Powder Processing and Characterization of W-3Ni-1Fe Tungsten Heavy Alloy

Matthew A. Hiser

Thesis submitted to the faculty of
Virginia Polytechnic Institute and State University
in partial fulfillment of the requirements for the degree of

Master of Science

in

Materials Science and Engineering

Alex O. Aning, Chair
William T. Reynolds
Guo Quan Lu
Mitsuhiro Murayama

April 25, 2011

Blacksburg, VA

Keywords: Tungsten Heavy Alloy, Mechanical Alloying, Sintering, Grain Size

Powder Processing and Characterization of W-3Ni-1Fe Tungsten Heavy Alloy

Matthew A. Hiser

ABSTRACT

Mechanical alloying, compaction by cold isostatic pressing, and pressureless sintering were used to study the potential for W – 3 wt% Ni – 1 wt% Fe to be processed into the bulk nanocrystalline form as a replacement material for depleted uranium in kinetic energy penetrators. Milling time and sintering temperature were varied from 15 to 100 hours and 1000 to 1300°C respectively. Particle size analysis and SEM showed a bimodal particle size distribution with most of the particles below 10 µm in size. XRD peak broadening analysis showed crystallite size to be reduced to below 50 nm, while peak shifting indicated a reduction in W lattice parameter due to dissolution of Ni and Fe atoms into the W BCC lattice.

Post-sintering bulk characterization showed density increasing strongly with increasing sintering temperature to above 90% of theoretical density at 1200°C. Apparent activation energy for sintering decreased strongly with increasing milling time. SEM micrographs showed a bimodal grain size distribution with some areas of smaller submicron grains and others with larger grains on the order of 1 – 4 µm, likely connected to the bimodal particle size distribution from milling. XRD and SEM also showed the precipitation of two secondary phases during sintering: $(Fe, Ni)_6W_6C$ incorporating carbon from the grinding media and an FCC solid solution of Ni, Fe, and W. The intermetallic carbide phase will increase strength but reduce ductility of the bulk material, which is not desirable. Micro and macrohardness testing show similar trends as density with a strong correlation with sintering temperature.

Acknowledgements

First, I would like to thank God for delivering me through some difficult times in my life, but never giving up on me and always drawing me closer to Him. My fiancée, Michelle, is the light of my world and helped to keep me sane through writing this thesis. I also want to thank my parents for their limitless support throughout my 22 years on this earth. I certainly would not be where I am today without them. The support of all my family, including my two sisters, Diana and Julia, four grandparents, aunts, uncles, and cousins, made this achievement possible. I also want to thank my friends, particularly Doug, Ian, and John, and their ability to help me have fun and stay motivated in my work.

I would like to acknowledge all of the people and institutions that helped make this project possible. The Virginia Tech Materials Science and Engineering department and its head Dr. David Clark and associate head Dr. Robert Hendricks provided the space and equipment for much of this work. Dr. Alex Aning was an excellent advisor in this work and has boundless enthusiasm in pursuing research. Andrew Zeagler, a PhD candidate under Dr. Aning, was instrumental in making this research possible, as I utilized much of his knowledge in similar work to quickly make progress in the lab and understand the results. John McIntosh and Jerry Hunter and their course on nanoscale characterization were an unbelievable help in using the SEM to get strong microscopy results.

Table of Contents

List of Figures

List of Tables

Chapter 1

---

1. Introduction

High-density kinetic energy anti-armor penetrator munitions made from depleted uranium (DU) have been deployed in combat by the U.S. military since the Persian Gulf War in 1991 [1-4]. However, since their introduction, concerns have been raised about the health and environmental effects of depleted uranium [1-4]. As a result, much research has focused on the development of tungsten heavy alloys (WHAs) as a less toxic replacement for depleted uranium in kinetic energy penetrators [5-14]. The Army Research Laboratory is currently working on a research plan to demonstrate “tungsten nanocomposite alternatives to depleted uranium in anti-armor penetrators [15].”

While tungsten (W) has sufficiently high density and is readily available, the challenge posed by tungsten is its behavior upon impact. Conventional, coarse-grained W tends to “mushroom” upon impact by massive plastic deformation, rather than “self-sharpen” by adiabatic shear banding, or localized bands of shear deformation [5, 10-12, 14, 16-20]. Research has shown that deformation behavior is dependent on both microstructure and strain rate. Adiabatic shear banding is more likely to occur as strain rate increases and as grain size decreases. Therefore, bulk nanocrystalline (NC) or ultra-fine grained (UFG) W will exhibit adiabatic shear banding at lower strain rates than coarse-grained W [5, 11, 12, 14, 16-20].

There are two general approaches to produce a bulk NC or UFG tungsten heavy alloy: bottom-up via powder processing or top-down via severe plastic deformation (SPD) [14]. Our bottom-up approach involving milling powders of W – 3 wt% Ni – 1 wt% Fe used limited amounts of Ni and Fe designed to be enough for alloying and potentially impinging grain growth, but not enough to unacceptably reduce density. A range of milling times (15, 25, and 50 hours) were used to gauge the effect of milling time on densification, microstructure, grain size, and mechanical properties.

After milling, the vital step of compaction and sintering is required to consolidate the powders into a bulk form. There are a variety of potential compaction and sintering methods including uniaxial pressing [21, 22], cold isostatic pressing (CIP) [21, 22], hot isostatic pressing [23], hot uniaxial pressing, and spark plasma sintering [24] among others. The most effective compaction and sintering method for this application would combine pressure and temperature simultaneously to maximize densification while minimizing grain growth. Unfortunately, due to equipment limitations, the only method available for this work was CIP followed by pressureless sintering under hydrogen atmosphere in a tube furnace. Post-CIP sintering parameters were varied as follows: time was held constant at one hour, while temperature was varied across three temperatures: 1000, 1100, and 1200°C. This study was designed to observe the effects of milling time and sintering temperature on densification, microstructure (particularly grain size), and mechanical properties of W – 3 wt% Ni – 1 wt% Fe.

Chapter 2

2. Background

2.1 Health Effects of Depleted Uranium

Depleted uranium, which is composed almost entirely of the stable U-238 isotope with little or no radioactive U-235 isotope, has been used in military munitions, particularly anti-armor kinetic energy penetrators (see Figure 1 [25]), since about 1980 due to its very high density and excellent penetrating capabilities upon impact [1, 4]. DU was used for the first time in combat during the Persian Gulf War in the early 1990s [1, 4]. In recent conflicts such as the Persian Gulf War, Bosnia, Kosovo, and Iraq, the U.S. military has fired more than 400 tons of DU in the form of anti-armor kinetic energy penetrators [4]. When DU is used as a kinetic energy penetrator it creates an aerosolized cloud of very fine particles upon impact. As the DU round pierces the armor, the outer layers of DU peel away in a "self-sharpening" effect, increasing penetration compared to other materials that mushroom upon impact. The aerosolized particles are the result of the material lost from the self-sharpening effect [4]. Due to the pyrophoric nature of DU in very fine powder form, the material that is aerosolized may also spontaneously ignite.

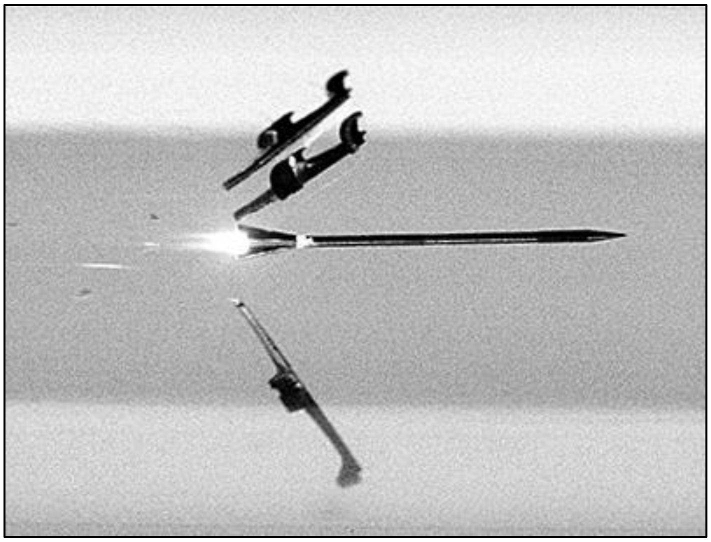

Figure 1 Kinetic energy penetrator with sabot separating [25] This work is in the public domain.

During the Persian Gulf War, roughly 115 US soldiers were directly exposed to high concentrations of aerosolized DU as a result of friendly fire [4]. A significant number of soldiers also received lower levels of contamination as a result of contact with DU rounds during storage, transport, and use [4, 26]. Subsequent concern about the adverse health effects of aerosolized DU led to several U.S. government studies to determine the long-term health effects of its use [1-4, 26, 27]. DU in bulk form poses only slight health risks and is not considered to be carcinogenic, with only 60% of the radioactivity of natural uranium [2, 3]. Therefore, the primary health concern with depleted uranium is its aerosolization upon impact, which creates a dust that may be inhaled and have more serious health effects [1, 4, 26]. The health risks of DU aerosols are primarily toxicological, consistent with heavy metal poisoning, causing damage to the liver and kidneys. Studies have shown a radiological risk to be present, but less significant than the toxicological risk, with the most severely exposed having a 1% chance of fatal lung cancer [27]. Numerous studies by the U.S. government as well as the World Health Organization have examined the issue and found DU aerosols to be a risk both to soldiers exposed directly in combat as well as environmentally due to the potential for postwar exposure through drinking water or other means [1-4, 26-28]. As a result of the conclusions from these health studies in additional to political and economic factors, the U.S. military has been actively researching tungsten as a replacement material for depleted uranium in anti-armor penetrators [15].

2.2 Deformation Behavior upon Impact of Tungsten

Tungsten compares favorably with depleted uranium in terms of density, with a value of 19.3 g/cc compared to 18.95 g/cc in DU, which even allows some potential for alloying tungsten with lighter metals without reducing density compared to DU. Also, according to van der Voet, et al., "tungsten and tungsten compounds are considered toxicologically relatively safe [3]." Nonetheless, toxicology research on tungsten and the specific risks associated with deploying it as a penetrator material are ongoing. Therefore, while tungsten (W) has sufficiently high density, is readily available and economical (given its widespread use in many other applications), and is "toxicologically relatively safe," the challenge posed by tungsten is its behavior upon impact.

2.2.1 Adiabatic Shear Banding Background

Adiabatic shear banding is a mode of plastic deformation in materials that is associated with a localized increase in temperature leading to localized shear and plastic deformation in bands ranging from 5 to 500 µm in width [29]. These bands form due to the inability of the material to conduct away the heat generated by plastic deformation at high strain rates (about 90% of the work from plastic deformation is converted to heat) [29]. Therefore temperature rises locally causing greater flow in the area of high temperature (flow stress decreases with increasing temperature), which becomes the shear band region [29]. In steels, adiabatic shear banding can be associated with a phase transformation from ferrite to austenite, which creates what is known as a transformed band that is observed as white under nital etching [29]. A second type of band is known as a deformed band, which experiences no structural transformation, but shows highly localized deformation due to temperature increases [29]. Deformed bands are much more likely in non-ferrous metals. Research in copper and aluminum alloys found "an inverse correlation between the work-hardening capability of these alloys and the severity of shear band formation [29]." In general, adiabatic shear banding is more likely in materials exhibiting a low strain-rate sensitivity and a high temperature sensitivity of the flow stress, which makes localized temperature increases more likely and their effects more dramatic [29].

2.2.2 Shear Banding in Tungsten and Depleted Uranium

For penetrator applications, adiabatic shear banding is highly desirable to reduce mushrooming (surface area increase) upon impact for maximum penetration. Figure 2 shows a schematic of how surface area is reduced by material discard from shear banding leading to greater penetration [30]. Unfortunately, conventional coarse-grained W tends to "mushroom" upon impact by massive plastic deformation, rather than "self-sharpen" by adiabatic shear banding, or localized bands of shear deformation [5, 10-12, 14, 16-20] as seen in Figure 3 [31]. While DU exhibits a self-sharpening effect upon impact to cause greater penetration, coarse-grained tungsten deforms into a mushroom shape. This mushroom shape causes the kinetic energy to be distributed across a larger area, leading to greater impact absorption by the armor and greatly reduced penetration depth.

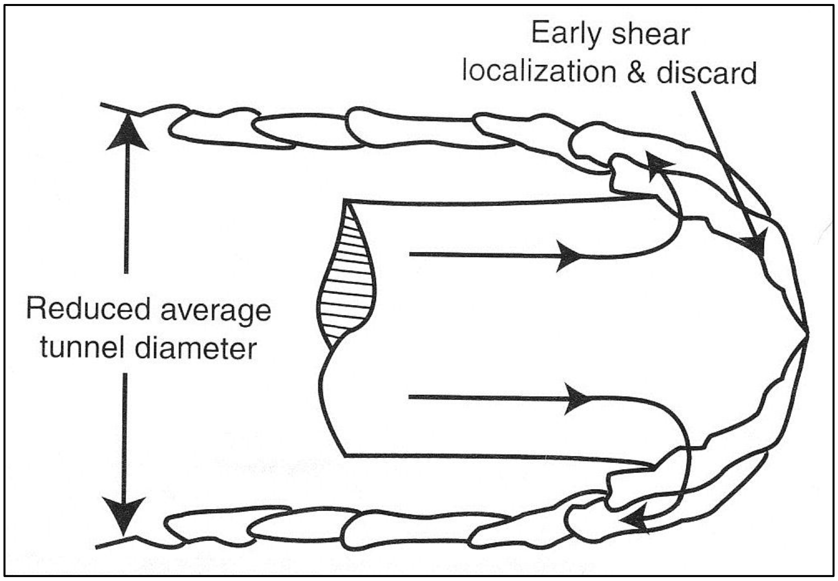

Figure 2 Improved penetration due to shear banding [30] Single figure reproduced with free permission from Cambridge University Press.

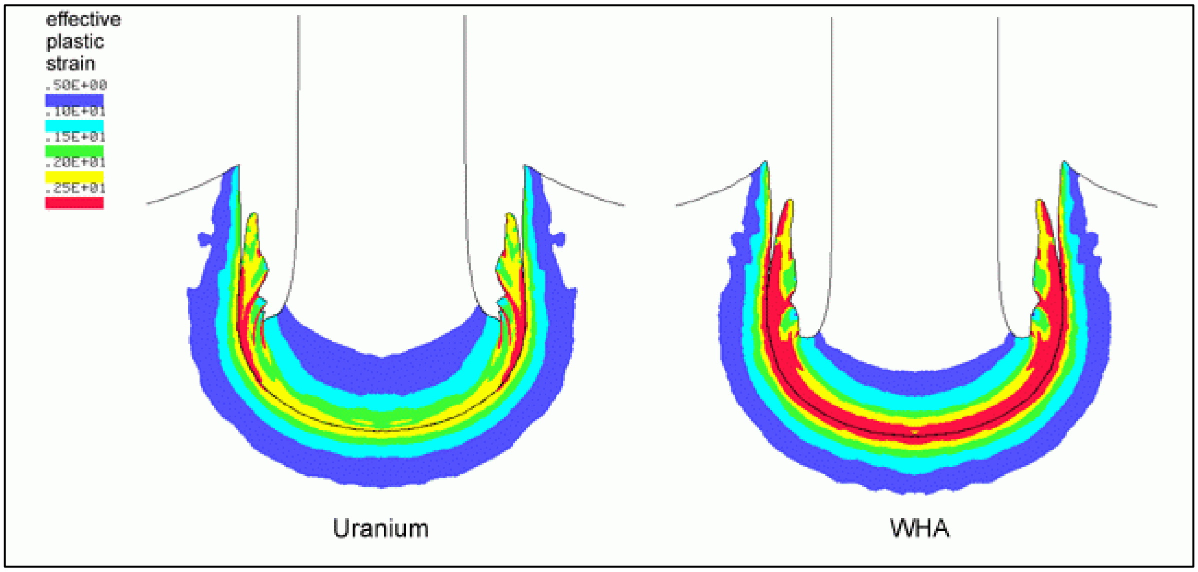

Figure 3 Shear banding in DU on left compared to mushrooming of WHA on right [31] with permission from R.C. Batra

Research has shown that deformation behavior is dependent on both microstructure and strain rate. Adiabatic shear banding is more likely to occur as strain rate increases and as grain size decreases.

For tungsten with grain sizes refined to 500 nm or below (ultra-fine grained or UFG) by severe plastic deformation (SPD), significant plastic flow localization is observed and strain rate sensitivity is reduced [16, 18, 32]. Additionally, tungsten with grain sizes below 100 nm (nanocrystalline or NC) formed by high pressure torsion (HPT) has shown localized shearing [17, 18, 20]. According to Wei, et al., "…UFG/NC microstructures not only significantly elevate the strength of tungsten, they also re-instate its ductility, decrease its strain rate sensitivity, and reduce its work hardening capability. These factors work together to greatly enhance the susceptibility of tungsten to adiabatic localization under uni-axial dynamic loading [17]." This means that NC or UFG tungsten may exhibit the behavior upon impact required for anti-armor penetrator applications.

2.3 Processing a Bulk Nanocrystalline or Ultra Fine-Grained Tungsten Heavy Alloy

There are two general approaches to produce a bulk NC or UFG tungsten heavy alloy: bottom-up via powder processing or top-down via severe plastic deformation (SPD) [14]. The top-down approach starts with a coarse-grained bulk material and uses extreme cold-working to reduce grain size. Prior research has demonstrated the ability to generate NC or UFG W by top-down methods such as SPD or HPT [16, 17]. Therefore, while the concept of using NC or UFG W to generate shear localization has been demonstrated by SPD or HPT (both top-down processes), the challenge remains to produce a high-density NC or UFG W via the bottom-up approach of powder metallurgy. The most straightforward approach would be to produce nanocrystalline powders by a process such as mechanical alloying or milling, and then consolidate these powders with a combination of temperature and pressure to densify the powders into a bulk without allowing unacceptable grain growth beyond the NC or UFG regimes to occur.

2.4 The Mechanical Alloying Process

Mechanical alloying (MA) was first developed by Benjamin in 1968 to aid in the production of high-temperature, dispersion-strengthened nickel alloys [33, 34]. However, by the 1980's, further use of the MA technique quickly revealed its applicability and effectiveness in processing many different material systems [35, 36]. Capabilities of MA include fine oxide dispersion (for ODS alloys), solid solubility limit extension, grain size refinement (down to nanometer size), solid-state amorphization, and inducement of low-temperature chemical reactions among others [35, 36].

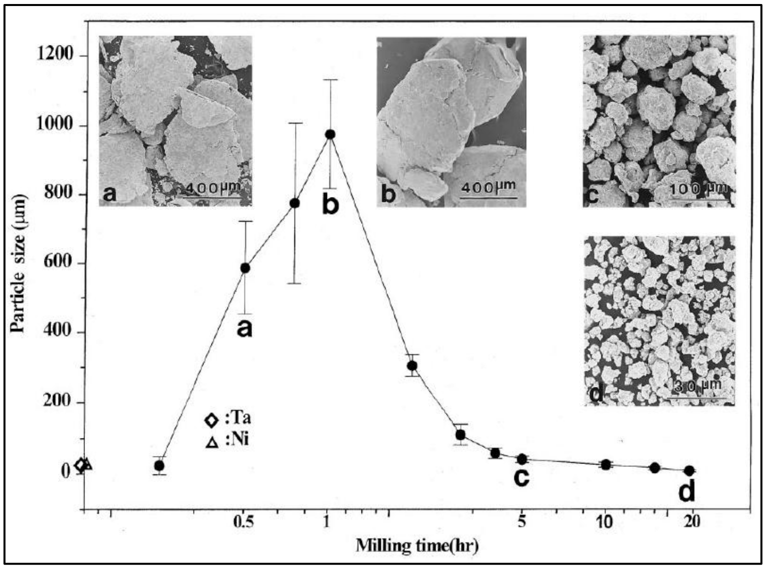

Figure 4 Effect of cold welding and fracture processes on particle size during MA [35] Reprinted with permission from Elsevier.

The mechanical alloying process involves placing powders (generally metallic) in a vial with hard, wear-resistant charge balls and milling for the desired time. Controllable parameters include charge ratio (weight of charge balls divided by weight of powders) and milling time among others. The MA technique utilizes the competing processes of fracture and cold welding to deform the powders over time as seen in Figure 4 [35, 36]. When two powders are being alloyed together by MA, a layered lamella structure of decreasing size with time is formed until a solid solution of the elements is reached as illustrated in Figure 5 below. The dynamic, energy-intensive nature of MA allows for extended solid-state solubility beyond the equilibrium phase diagram for a system. Additionally, crystallite (or grain) size decreases with increasing milling time down into the nanometer range [35, 36]. These two key phenomena of solid-state solubility extension and nanograin size refinement were utilized in this work for the W-Ni-Fe system. The idea was to reduce grain size to the nanoscale and supersaturate the W lattice with Ni and Fe to form a solid solution and hopefully impede grain growth during sintering.

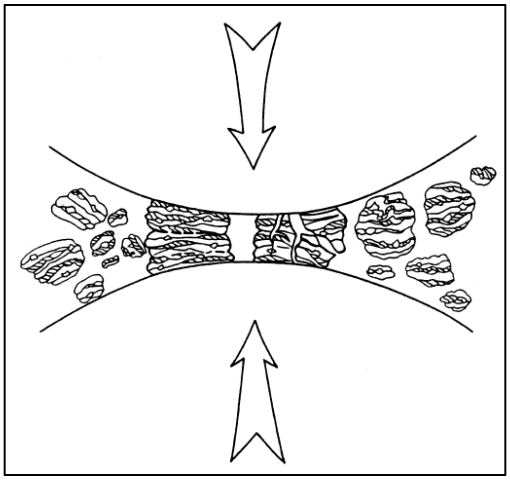

Figure 5 Ball-powder-ball collision schematic [35] Reprinted with permission from Elsevier.

2.5 Compaction and Sintering Methods

After mechanical alloying to generate a supersaturated nanocrystalline structure, a compaction and sintering step is required to transition from the powder form to the fully dense bulk form. There are two primary ways to perform the densification and sintering process found in the powder metallurgy literature: cold compaction followed by pressure-less high-temperature sintering or hot compaction in which the pressure to consolidate/compact is provided simultaneously with an elevated sintering temperature. The sintering and densification process occurs via the driving force of surface area reduction of the particles [21, 37]. The mass transport mechanism in metals which allows for this surface area reduction is generally vacancy diffusion from sources to sinks [21]. High temperatures are required for sintering and densification to allow for sufficient diffusion rates to be achieved to reduce the surface area and densify the part. Cold compaction techniques include cold uniaxial pressing and cold isostatic pressing (CIP), which would be followed by a pressureless sintering step to generate a dense bulk form. Hot compaction techniques that apply heat and pressure simultaneously such as hot uniaxial pressing, hot isostatic pressing (HIP), and spark plasma sintering (SPS) tend to be more effective at achieving full density while minimizing time at elevated temperature, but also more expensive.

2.5.1 Cold Compaction and Pressureless Sintering

There are two primary methods of cold compaction found in the powder metallurgy literature: cold uniaxial pressing and cold isostatic pressing (CIP) [21]. These processes are performed at low (non-sintering) temperatures and generally followed by a sintering stage to increase the density by reducing porosity and improving the bonding of the powders.

Cold uniaxial pressing involves the placing of the powder in a cylindrical die and pressing between lower and upper punches to a pressure of 400 to 800 MPa [21]. The advantages of uniaxial pressing include material and energy efficiency, ability to press large geometrical shapes, good dimensional precision and repeatability, and high rate productivity [21]. Overall, uniaxial pressing is cheap, fast, and reliable, but the resulting compact is of lower quality than can be produced by cold isostatic pressing. The issues include inhomogeneous density causing uneven shrinkage upon sintering along with significant residual stresses due to wall friction with the die upon removal. Figure 6 at right shows a schematic of the uniaxial compaction process, with particles first repacking to reduce porosity, before eventually deforming under increasing pressure to reduce porosity [37]. The extent and nature of deformation depends on the hardness and deformation behavior of the material at low temperature. The material deformation and pore distribution can greatly affect the ensuing sintering process.

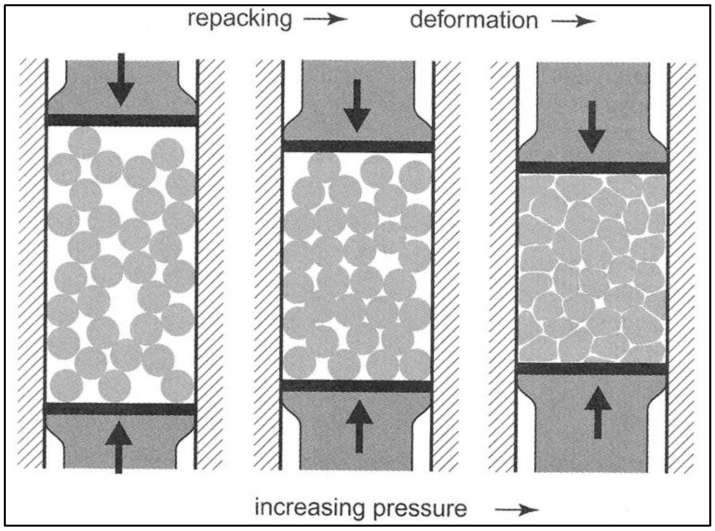

Figure 6 Cold uniaxial compaction process [37] Reprinted with permission from MPIF

Cold isostatic pressing, on the other hand, involves the application of pressure by a gas or fluid surrounding a flexible mold containing the powder, as illustrated in Figure 7. Pressures as high as 700 MPa can be reached by CIP. CIP has several advantages over uniaxial pressing, including homogeneous pressing, no residual stresses due to wall friction, and no need for the addition of binders or lubricants [22]. Homogeneous pressing results in homogeneous density in the green compact and therefore even shrinkage upon sintering. Not having to add binders or lubricants eliminates the binder burnoff step, increases green density, and removes a major contaminant source [22]. Overall, cold isostatic pressing has many technical advantages over uniaxial pressing in the resulting compact, but CIP is more expensive and slower than uniaxial pressing.

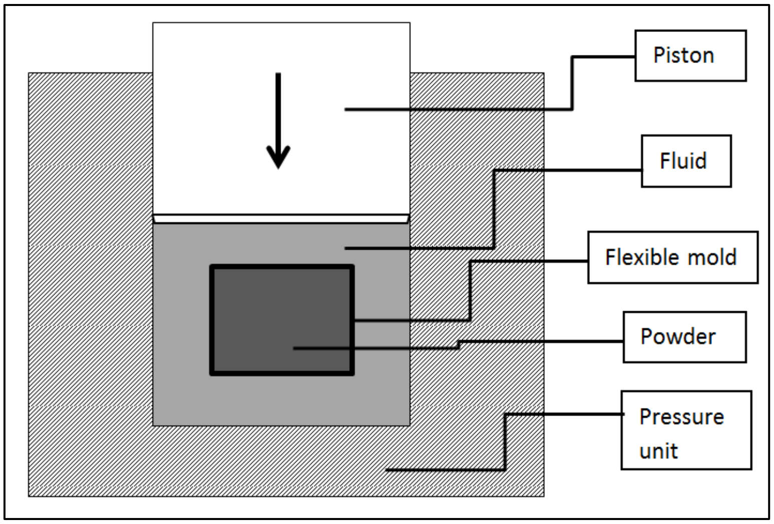

Figure 7 Schematic of cold isostatic pressing

The cold compaction process generally takes place in three stages: rearrangement, elastic-plastic deformation at particle interfaces, and massive deformation of particles leaving only small pores [22]. The first stage of particle rearrangement takes place at low pressures and reduces the porosity by 5-10%. Elastic-plastic deformation occurs at intermediate pressures and increases with pressure to increase interfacial contact and remove more porosity. Finally, massive deformation occurs at the highest pressures and leaves only small, isolated pores between the particles [22]. Due to the advantages over uniaxial pressing and equipment limitations, cold isostatic pressing followed by pressureless sintering was used in this work.

2.5.2 Hot Compaction and Sintering

The primary hot compaction methods are hot uniaxial pressing [23], hot isostatic pressing (HIP) [38], and spark plasma sintering (SPS) [23, 24]. Hot uniaxial pressing simply involves the placing of the powder in a cylindrical die and pressing between lower and upper punches to high pressure (400-800MPa) while holding at an elevated temperature [22, 23].

Hot isostatic pressing (HIP) involves the application of pressure up to 700 MPa by a gas or fluid surrounding a flexible mold containing the powder along with elevated temperatures to over 1000˚C [22, 38]. According to Majumdar, et al., “HIP is considered to be the most promising consolidation method for producing fine grain, uniformly dense bulk material by careful control of the temperature, isostatic pressure and processing time" [23]. These advantages of HIP are also true for hot uniaxial pressing, with precise control of the three main parameters of temperature, pressure, and time, but the primary drawback of uniaxial pressing is the inhomogeneous nature of the resulting compact.

Spark plasma sintering (SPS) is a more recently developed technique utilizing pulsed DC current and uniaxial pressure featuring high heating rate (up to 1000˚C/min), a low sintering temperature and a short isothermal holding at the sintering temperature [21, 24]. Heating of the powder occurs both through heat transfer from the punches and internal heating via the Joule effect [21, 24]. This technique should allow for better maintenance of a nanocrystalline structure by minimizing sintering time and temperature to limit grain growth and has been used by other researchers performing similar work [16, 18].

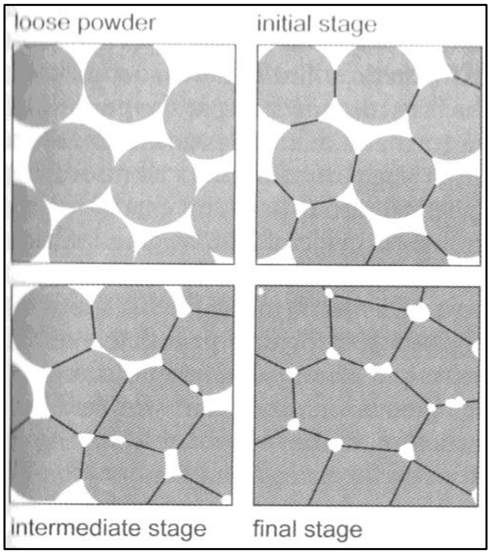

Figure 8 Stages of sintering [37] Reprinted with permission from MPIF

2.6 Sintering Theory

Sintering theory describes the progression of densification, porosity elimination, and microstructural changes during the sintering process. Without prior compaction, sintering proceeds through the four stages seen in Figure 8 at right: loose powder, initial, intermediate, and final [37]. With prior compaction (as in our work), sintering begins in the initial stage with necking between neighboring particles. Initial stage sintering proceeds fastest due to the curvature of the concave region of the neck. However, as the neck grows and sintering progresses, the curvature decreases and sintering rate slows. Intermediate stage sintering is reached when necks begin to interfere and overlap with each other, but the porosity remains open and considerable [37]. As sintering progresses porosity continues to decrease, which reduces the impediment to grain growth, allowing grains to grow faster as porosity decreases more slowly due to decreasing concavity. The relationship between grain growth and sintered density in general can be seen in Figure 9 with data for copper [37]. Final sintering is reached once porosity becomes closed as seen in the lower right portion of Figure 8.

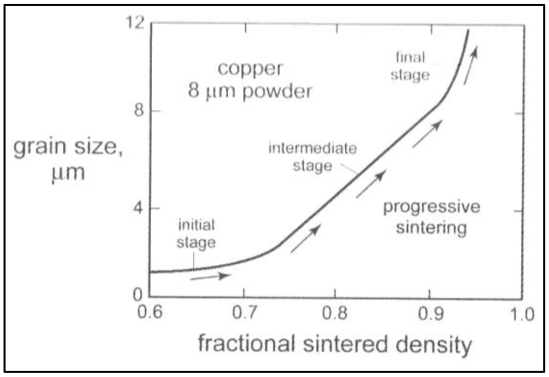

Figure 9 Grain size as a function of sintered density [37] Reprinted with permission from MPIF

The nature of the pores during the sintering process determines important characteristics of the final structure of the material. First of all, full 100% density will only be achieved through vacuum sintering, because the presence of gas molecules during sintering will prevent closed pores from ever completely being eliminated (although they may shrink considerably) [37]. This is important for our work, where sintering under hydrogen atmosphere was used, meaning full densification is not to be expected. The location of the pores in the material is also crucial. Pores on grain boundaries lead to densification as they are eliminated, while isolated pores (not on grain boundaries, but rather within grains) do not lead to densification as illustrated in Figure 10 [37]. Along with the effect on densification, pore location also effects grain growth with pores on grain boundaries impeding grain boundary motion and reducing grain growth, while isolated pores do little to affect grain growth.

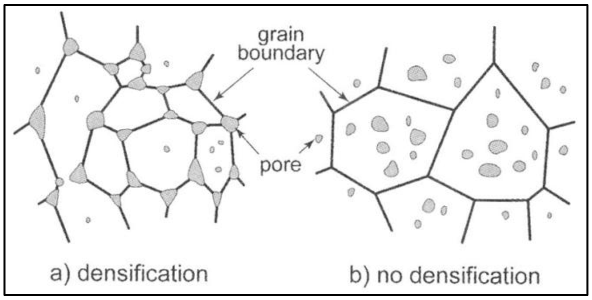

Figure 10 Importance of pore location [37] Reprinted with permission from MPIF

2.7 Experimental Results from Related Work

Research into the MA of tungsten heavy alloys has been performed by various researchers with different alloying elements, processing conditions and approaches. Aning, et al. investigated the solution kinetics and amorphization of pure tungsten and W-Ni [39]. Solid-state amorphization of equimolar W-Ni particles for dispersion strengthening was demonstrated by Zeagler [40]. More relevant work by Hong et al. used multiple milling and liquid phase sintering steps to form an inhomogeneous distribution of solid solution matrix phase and trigger localized shear deformation in 93W 5.6Ni-1.4Fe [7].

2.7.1 Ni-enhanced W Diffusion

Numerous researchers have observed the effect of small additions of nickel to cause activated sintering of tungsten [41-45]. Moon et al. looked at the effect of nickel on W grain growth, but at much larger grain sizes than our work [44]. Gessinger and Fischmeister proposed the enhancement of grain-boundary self-diffusion in tungsten by nickel additions to be the cause of improved sintering [42]. Hwang et al. pointed to a structural transition of the W grain boundary from an ordered to a disordered structure in the presence of nickel as the cause of activated sintering [45]. German and Munir found palladium to be the best activator of W sintering followed in order by nickel, cobalt, platinum, and iron [41], while Boonyongmaneerat did a more detailed study of the effect of iron and nickel on W sintering and found that nickel is much more effective than iron at activating W sintering [43]. All prior research described here has focused on very small additions of Ni or Fe (0.5 wt% or less) and their effect on enhancing grain boundary diffusion to increase densification and grain growth rates. However, this work involves greater amounts of nickel, which may be expected interact volumetrically with tungsten, particularly given the ability of high-energy ball milling to force mixing. While Gessinger [42] makes a passing claim that nickel does not enhance volume diffusion of W (without any further explanation or support), both German et al. [41] and Boonyongmaneerat [43] discuss the possibility of nickel improving the volume diffusion of W to help explain the activated sintering of W by nickel. This possibility will be discussed later in Chapter 5 to help explain some of the trends found in our experimental results of W-3Ni-1Fe.

2.7.2 Oxide-Dispersion Strengthening

Other researchers including Jing-lian, et al. [46], Lee et al. [47], and Fan, et al. [48], have used mechanical alloying with oxide-dispersion strengthening to improve mechanical properties, particularly ductility in WHA. Jing-lian et al. added yttria oxide to 90W-7Ni-3Fe to increase densification in liquid phase sintering and achieve 10-µm grain size with 30% elongation and 1050 MPa strength [46]. Lee et al. used partially stabilized zirconia (PSZ) dispersoids to increase ductility and high-temperature strength by comparing one and two-step milling processes and their effect on dispersoid location relative to grain boundaries [47]. Meanwhile, Fan et al. studied Y_2O_3 dispersed 93W-4.9Ni-2.1Fe and was able to achieve grain sizes of 3-5 µm leading to adiabatic shear bands at a strain rate of 1900 s^{-1} [48].

2.7.3 Severe Plastic Deformation

Although a totally different approach, it is also important to understand the results being achieved by a top-down method of severe plastic deformation (SPD) as reported by Mathaudhu, et al. [12], Wei, et al. [32], Wei, et al. [20], Cho et al. [16], Wei, et al. [17], and Wei, et al [14]. Mathaudhu performed equal-channel angular extrusion (ECAE) at 1000 or 1200°C followed by annealing at 1600°C for 1 hour and observed equiaxed grain sizes of 350 nm and a recrystallization temperature of 1400°C [12]. Wei used ECAE at 1000°C to reduce grain size to 500 nm and demonstrated that strain rate sensitivity at this ultra-fine grain size is halved relative to that of conventional coarse-grained W [32]. Wei used high-pressure torsion (HPT) at 500°C to achieve grain sizes below 200 nm with large-angle, high-energy grain boundaries with high dislocation densities [20]. However, this nanocrystalline W structure showed much smaller shear band width of 5 µm as compared to 40 µm for ultra-fine grained W [20]. Cho et al. used ECAE to generate and study ultra-fine grain size W and the formation of shear bands, while hypothesizing that the origin of brittle behavior in W is due to impurities such as C, N, S, meaning that the key to optimal behavior is reducing or eliminating these impurities [16]. Wei et al. used ECAP and HPT to study the effects of ultra-fine grain size and impurity concentration on W ductility [17]. Overall, top-down SPD methods have achieved the desired grain sizes, but with high-angle boundaries and large numbers of dislocations. Therefore, SPD has been useful in a laboratory setting to confirm the formation of shear bands at ultra-fine grain sizes, but powder processing methods would still be desirable.

2.7.4 Liquid Phase and Pressureless Sintering

Much research has been done on liquid phase sintering, but less on pressureless solid-state sintering of WHA. Ryu et al. describes mechanical alloying followed by cold isostatic pressing (CIP) and liquid phase sintering on W-5.6Ni-1.4Fe for a high-density depleted uranium replacement [13]. Ryu et al. were able to achieve nanocrystalline grain size of 16 nm after 36 hours milling, and a 97% dense bulk compact with 3 µm grain size [13]. Sarkar et al. used planetary milling of elemental W for 100 hours followed by sintering to three different temperatures to achieve a grain size of 5 µm at 90% density and 20 µm at 96% density [49]. Meanwhile, Wang, et al. discussed the sinterability of nanocrystalline tungsten powder and the effects of particle size and grain size on sintering for different times and temperatures [50]. However, their discussion did not include information about post-sintering grain size. Our work falls somewhat in between the above, with less alloying than Ryu and a more solid-state sintering approach like Sarkar and Wang, but not pure W like Sarkar and Wang.

2.7.5 Spark Plasma Sintering

The most desirable powder compaction method of producing bulk nanocrystalline W is spark plasma sintering, which features very high pressures and ramp rates, meaning better densification with less time at high temperature and therefore less grain growth. Xiao-qiang, et al. [51] worked with 93W-4Ni-2Co-1Fe with milling up to 60 hours followed by spark plasma sintering. They found the most optimal milling time to be 15 hours with a grain size of 340 nm and a density of 16.78 g/cc after sintering. Klotz, et al. achieved a density of 16.96 g/cc of pure W and grain sizes between 1 and 10 µm after ball milling and spark plasma sintering at 100 MPa up to 1600°C.

Having a firm understanding of other work that has been done on this topic is important when analyzing the impact and importance of our results. These other published results by similar, yet competing processes and approaches provide a good benchmark for the success and significance of our work.

Chapter 3

3. Experimental Methods

Powders were processed by mechanical alloying, cold isostatic pressing, and pressureless sintering before being cut, polished, and characterized. Characterization included density measurements, X-ray diffraction (XRD), scanning electron microscopy (SEM) with energy dispersive X-ray spectroscopy (EDS), and hardness testing (macro and micro) for bulk samples. Likewise, powder samples from milling were characterized by a particle size analyzer, SEM, and XRD.

3.1 Powder Processing

Powders of the desired composition were processed by mechanical alloying for various times, followed by cold isostatic pressing to form a green compact. This green compact was then pressurelessly sintered for one hour at various temperatures before characterization.

3.1.1 Preparation and Milling of Powders

Elemental powders of tungsten (W), nickel (Ni) and iron (Fe) were measured out to the ratio of 96 wt% W – 3 wt% Ni – 1 wt% Fe (88.33 at% W – 8.65 at% Ni – 3.03 at% Fe). W powder was acquired from Alfa Aesar at 99.9% purity and -325 mesh size, Ni powder was acquired from Atlantic Equipment Engineers at 99.9% purity and -100/+325 mesh size and Fe powder was acquired from Atlantic Equipment Engineers at 99.8% purity and -325 mesh size. All handling and mixing of the powders was performed under argon atmosphere in a Labconco Protector Glove Box to prevent oxidation. All powders were reduced in a Lindberg Blue M (Model #54233) tube furnace with hydrogen atmosphere by heating to 500˚C for 1 hour prior to mixing and milling.

The W – 3 wt% Ni – 1 wt% Fe mixture of powders was milled in a SPEX 8000 high-energy shaker mill seen in Figure 11 at 7200 Hz using a tungsten carbide (WC) milling vial with 7/16" WC milling balls, also shown in Figure 11. A ratio of milling ball weight to powder weight (charge ratio) of 2:1 was used with about nine balls weighing around 75 g total and 37.5 g of W – 3 wt% Ni – 1 wt% Fe powder. The loading and sealing of the vial was done under argon atmosphere in the glove box, ensuring milling to occur under inert conditions to prevent

Figure 11 WC milling vial and balls on left and SPEX 8000 mill on right [35] Reprinted with permission from Elsevier.

oxidation and atmospheric contamination of the powder. Slight heating of the vial and its contents to an insignificant temperature of less than 100˚C was observed during milling.

Milling times of 15, 25, and 50 hours were used to assess the effect of milling time on densification, microstructure, and properties. An additional milling time of 100 hours was performed and partially characterized by XRD, SEM for powder size and morphology, and particle size analysis, but not compacted and sintered for full characterization.

3.1.2 Compaction and Sintering

After milling the powders were removed from the mill under inert atmosphere and then compacted by cold isostatic pressing (CIP) in an AIP CP360 cold isostatic press (as seen in Figure 12 at right) at a pressure of 30 ksi (138 MPa) for 10 minutes in a cylindrical polymer mold. To improve densification, air in the mold was removed using a syringe prior to pressing. In an additional effort to improve densification without significantly affecting grain size, after pressing, samples were subjected to a heat treatment of 300°C for one hour in the tube furnace under hydrogen atmosphere designed to allow for some recovery of the defects in the crystal structure from the milling process. This recovery heat treatment was followed by a second CIP run, under the same parameters as previously. Compacted samples were approximately 20 g in mass.

Figure 12 AIP CP360 Cold isostatic press

Following the second round of pressing, the compacted samples were sintered in a Lindberg Blue M (Model #54233) tube furnace under hydrogen atmosphere for varying temperature from 1000 to 1200˚C for 1 hour for all three milling times (15, 25, and 50 hours) to total nine samples. A heating rate of 5˚C/min followed by ambient cooling was used under hydrogen atmosphere to prevented oxidation and contamination of the samples during sintering.

An additional six samples were prepared followed the same procedure as above, but sintered for 1300°C for 25 and 75 hours for all three milling time of 15, 25, and 50 hours. These samples were designed to assess the maximum density that can be achieved by CIP and pressureless sintering for comparison to the theoretical density as well as provide a greater view of grain size as a function of heating parameters. Table 1 summarizes the full test matrix of fifteen samples.

Table 1: Sintering Temperature and Milling Time Test Matrix

Milling Time/ Sintering Parameters	1000˚C for 1 hour	1100˚C for 1 hour	1200˚C for 1 hour	1300˚C for 25 hours	1300˚C for 75 hours
15 hours	X	X	X	X	X
25 hours	X	X	X	X	X
50 hours	X	X	X	X	X

3.2 Sample Preparation

After sintering, the cylindrical compacts were cut using a Buehler Isomet low-speed saw with a diamond blade. The cut was made about halfway between the midplane and one end of the sample or about 75% of the way down the sample axially. The smaller slice was used for X-ray diffraction, while the remainder was mounted and polished for microscopy and hardness testing. Samples were mounted by taking a compacted cylinder of mounting polymer and using Krazy glue to attach a bulk sample of W-Ni-Fe to one end. This setup was used for each sample and allowed for use of a Buehler Automet 2 six-piece autopolisher for efficiency and consistency. Using the autopolisher, grinding was performed down to the 600 grit size followed by polishing with alumina to 0.3µm and a 0.05µm colloidal silica finishing polish. No etching was found necessary as grains were easily identifiable in the SEM using the backscattered electron detector (BSED).

3.3 Characterization

Both bulk and powder samples were characterized by various techniques to assess the effect of the milling and sintering processes on densification, microstructure, and properties. To adequately achieve this goal, characterization was performed on milled powders to observe the effects of milling and on bulk samples to observe the effects of milling and sintering. Primary parameters of interest based on this experimental design are milling time and sintering temperature.

3.3.1 Powder Characterization

Milled powders were characterized to assess the effects of milling on microstructure and particle morphology. Particle size analysis allowed a quantitative assessment of the range of particle sizes, while SEM provided imaging of the powder particles as a function of milling time to confirm size distribution and observe morphology. Finally, X-ray diffraction allowed the microstructure to be assessed using Williamson-Hall plots to quantify strain and crystallite size from peak broadening as well as peak shift to determine dissolution of Ni and Fe in W.

3.3.1.1 Particle Size Analysis

A Horiba LA-950 Laser Diffraction Particle Size Distribution Analyzer with guarantees on accuracy up to 0.6 % and precision up to 0.1% was used to evaluate W-3Ni-1Fe powders milled for zero, 15, 25, 50, and 100 hours to assess the effect of milling on the particle size distribution. Each sample was repeated with at least three runs to provide confidence in the results, which were output as plots of frequency on a linear y-axis versus particle diameter on a logarithmic x-axis.

3.3.2.2 Scanning Electron Microscopy

W-3Ni-1Fe powders milled for zero, 15, 25, 50, and 100 hours were imaged at the Virginia Tech Institute of Critical Technology and Applied Science Nanoscale Characterization and Fabrication Laboratory (VT ICTAS NCFL) using the FEI Quanta 600 FEG Environmental Scanning Electron Microscope (SEM) using an accelerating voltage of 20 kV with a spot size of about 5 nm. A range of magnifications were used to assess the size distribution and morphology of particles ranging in size from less than one to greater than 100 microns.

3.3.2.3 X-ray Diffraction

W-3Ni-1Fe powders milled for zero, 15, 25, 50, and 100 hours were tested by X-ray diffraction using a PANalytical X'Pert Pro PW 3040 diffractometer using the following incident beam optics parameters: nickel filter, 10 mm mask, 1˚ anti-scatter slit, and Bragg angle (2Θ) range from 30 to 90˚. Each sample was run twice in the diffractometer under identical parameters for statistical reasons when quantifying peak shifts and broadening. Analysis of this data focused on peak broadening and shifting of the four tungsten (W) peaks in this range as a function of milling time and Brag diffraction angle. MDI Jade 5.0 software was used to analyze peaks for precise diffraction angle (which correlates with d-spacing) as well as the full-width at half of the maximum peak as an assessment of peak broadening.

3.3.2.3.1 Lattice Parameter

The Bragg angle location of the W peaks was used to estimate the W lattice parameter for each sample. It is known that each diffraction angle correlates with a d-spacing of the planes creating the peak. From the powder diffraction files stored in the MDI Jade 5.0 software, the orientation of the planes generating a given peak is also known. For example, the most intense W peak occurs at a Bragg angle (2θ) of about 40.4° and is created by the (110) set of planes of the W crystal. There are three other well-defined W peaks in the range of 2θ from 30° to 90° for which the approximate angle and (hkl) planes generating the peak are known. Table 2 shows the four primary W peaks between 30° and 90° and their respective planes.

Table 2: Primary W XRD Peaks

Approximate Angle (2θ)	Generating Plane (hkl)
40.4°	(110)
58.4°	(200)
73.3°	(211)
87.1°	(220)

The diffraction angle correlates to a d-spacing of the planes generating a given peak, which can be called d_{hkl}. From this d_{hkl} for each set of planes, one need only multiple by the square root of the sum of the squares of the values h, k, and l for each set of planes to obtain an estimate of the W BCC lattice parameter [52]. Therefore, each XRD run provided four estimates of the W BCC lattice parameter based on the d-spacing from the diffraction angle. With two XRD runs per sample, the W lattice parameter calculated for each milling time is the average of eight estimates (four peaks in each of two runs). Equation 1 shows the calculation of the W BCC lattice parameter from d_{hkl}, h, k, and l.

$$W\ lattice\ parameter = d_{hkl} * \sqrt{h^2 + k^2 + l^2} \qquad \text{Eq. 1}$$

Shifting of the W peaks with increasing milling time indicates the metastable dissolution of Ni and Fe into the W lattice. Using the unmilled W-Ni-Fe powder XRD W peaks as a baseline value (a^o_{WBCC} = 0.31615 nm) of the W lattice parameter, approximate quantification of the at% of Ni and Fe present in the W solvent was inferred from the decrease in W lattice parameter. According to the W-Ni and W-Fe phase diagrams, Fe is much more soluble in W at equilibrium than Ni (0.8% vs. 0.1%), likely due to the common crystal structure of Fe and W (BCC) in contrast with Ni (FCC) [52-54]. However, our composition also has about three times as many Ni atoms as Fe atoms, so while Fe is more easily dissolved in W, there are more Ni atoms available to be dissolved in the W lattice.

To simplify quantification, two key assumptions were made. First, since Fe and Ni are nearly the same atomic size (atomic radius of 0.124 nm for Fe and 0.125 nm for Ni) and Fe has a stable room-temperature BCC phase [52], the lattice parameter of BCC Fe (a^o_{FeBCC} = 0.287 nm) was used when estimating the at% of Ni/Fe dissolved in W. Also, a linear effect of Ni/Fe on the average W BCC lattice parameter was used. Therefore, if the lattice parameter was calculated to be halfway between the W and Fe BCC lattice parameters (a^o_{WBCC} and a^o_{FeBCC}), it would be assumed this means there is 50at% W – 50at% Ni-Fe. Equations 2 and 3 provide the conversion from W BCC lattice parameter to estimated at% Ni/Fe and then from estimated at% Ni/Fe to estimated wt% Ni/Fe.

$$at\%\,Ni/Fe = \frac{a^o_{WBCC} - a_{WBCC}}{a^o_{WBCC} - a^o_{FeBCC}} * 100\% \qquad \text{Eq. 2}$$

$$wt\%\,Ni/Fe = \frac{at\%Ni/Fe * AW_{Ni/Fe}}{at\%Ni/Fe * AW_{Ni/Fe} + (1 - at\%Ni/Fe) * AW_W} * 100\% \qquad \text{Eq. 3}$$

where AW_W = atomic weight of tungsten and
$AW_{Ni/Fe}$ = average of the atomic weights of nickel and iron (which are very similar)

3.3.2.3.2 Williamson-Hall Plots

In addition to analyzing peak shifts, Williamson-Hall plots were also used to analyze peak broadening as a function of milling time and diffraction angle. A Williamson-Hall plot allows one to separate out the contributions to peak broadening of crystallite size and strain by the following relation in Equation 4 [55, 56].

$$\beta_{size+strain} * \cos\theta = \eta \sin\theta + \frac{K\lambda}{d} \qquad \text{Eq. 4}$$

where $\beta_{size+strain}$ is the peak broadening in radians due to crystallite size and lattice strain, θ is one half of the diffraction angle 2θ, η is the lattice strain, d is the crystallite size, K is the shape factor (assumed to be 0.9), and λ is the wavelength of the X-rays.

For peak broadening, the full width at half max (FWHM) value less the instrument broadening (accounted for by the FWHM from a coarse-grained W sample) of the three largest W peaks (the first three listed in Table 2) was used for $\beta_{size+strain}$, along with the angle θ of the given peak. With this information for each peak, it was fairly straightforward to plot three points for each sample of FWHM * cos(θ) vs. sin(θ). A best-fit line was generated for each set of points, with the slope representing η or lattice strain and the y-intercept equaling $\frac{K\lambda}{d}$, which can easily be solved for d or crystallite size. In this fashion, Williamson-Hall plots were generated and the data used to analyze lattice strain and crystallite size (an estimate of grain size) as a function of milling time.

3.3.2 Bulk Characterization

Bulk samples were characterized to assess the effect of sintering temperature and milling time on densification, grain size, microstructure, and mechanical properties. Density measurements both by calipers to estimate volume and Archimedes' principle were used to quantitatively assess densification, along with SEM, which provided a more qualitative assessment. XRD was used to determine phases present, along with peak shifts to analyze lattice parameter as mentioned in the powder characterization section above. SEM provided direct assessment of grain size and microstructure, as well as compositional mapping and point estimates of composition using EDS. Finally, hardness testing (both macro and micro) provides information on mechanical properties, which are affected by density and microstructure, particularly grain size.

3.3.2.1 Density Measurements

Density measurements were taken on both green compacts and final sintered compacts to see the effects of pressing, recovery heat treatment and repressing, and sintering. For pre-sintering density measurements, rough calculation was done with calipers by measuring the height and diameter of the sample to estimate cylindrical volume. The mass of the sample was divided by this volume to estimate density. These caliper density measurements were performed three times: after initial pressing, after repressing, and after final sintering to assess the effectiveness of the recovery heat treatment and repressing, as well as to correlate to values determined by Archimedes' principle after final sintering. In addition, one pre-sintering sample from each milling time was measured by Archimedes' principle.

Archimedes' density measurement was performed on each sample after final sintering to assess densification. A traditional Archimedes' density approach was used by taking the weight of the compact in air (W_{air}) and then in ethanol ($W_{ethanol}$) along with the known density of ethanol ($\rho_{ethanol} \approx 0.79$ g/cc) at the given temperature and the density of air ($\rho_{air} = 0.0012$ g/cc) to estimate the density of the compact ($\rho_{compact}$). These values are related by Equation 5:

$$\rho_{compact} = \frac{W_{air}}{W_{air} - W_{ethanol}} * (\rho_{water} - \rho_{air}) + \rho_{air} \qquad \text{Eq. 5}$$

Theoretical density (ρ_{th}) was calculated by assuming a 100-g sample with 96 g of W, 3 g of Ni and 1 g of Fe. Using the known densities of W (19.25 g/cc) , Ni (8.908 g/cc), and Fe (7.874 g/cc), the volume of this 100 g sample is calculated and used to calculate the theoretical density. Equation 6 shows the calculation.

$$\rho_{th} = \frac{m}{V} = \frac{m_W + m_{Ni} + m_{Fe}}{m_W/\rho_W + m_{Ni}/\rho_{Ni} + m_{Fe}/\rho_{Fe}} = \frac{100\ g}{4.9870cc + 0.3368cc + 0.1270\ cc} = \mathbf{18.346}\,\frac{\boldsymbol{g}}{\boldsymbol{cc}} \qquad \text{Eq. 6}$$

3.3.2.2 X-ray Diffraction

All bulk W-3Ni-1Fe sintered samples were tested by X-ray diffraction using a PANalytical X'Pert Pro PW 3040 diffractometer using the following incident beam optics parameters: nickel filter, 10 mm mask, 1˚ anti-scatter slit, and Bragg angle (2Θ) range from 30 to 90˚. Analysis of this data focused on peak identification to identify the presence of secondary phases as well as shifting of the four tungsten (W) peaks in this range as a function of milling time and Brag diffraction angle. MDI Jade 5.0 software was used to analyze peaks for precise diffraction angle (which correlates with d-spacing).

3.3.2.3 Scanning Electron Microscopy

All bulk W-3Ni-1Fe sintered samples were imaged at the Virginia Tech Institute of Critical Technology and Applied Science Nanoscale Characterization and Fabrication Laboratory (VT ICTAS NCFL) using the FEI Quanta 600 FEG Environmental Scanning Electron Microscope (SEM, seen in Figure 13) using an accelerating voltage of 20 kV with a spot size of about 5 nm. A range of magnifications were used to assess both the densification and porosity at lower magnifications and the grain size distribution and microstructure at higher magnification.

Figure 13 FEI Quanta 600 ESEM used in this work

Energy dispersive spectroscopy (EDS) during SEM imaging allowed the correlation of different regions in the SEM image with different concentrations of elements in those regions. For this analysis, Esprit 1.8 EDS software was used to generate compositional maps overlaying the presence of different elements on an SEM image. This software also allowed the gathering of EDS spectra on specific points or areas to confirm regions rich in W or Ni and Fe semi-quantitatively as ratios relative to Ni. Semi-quantitative means the absolute concentration values are not reliable due to a lack of standards, but the relative concentrations from one region to another in the same sample are reliable to assess the relative concentration of a particular element in one area compared to another. Beam energy of 20 keV was used to excite desired X-ray peaks of Fe, Ni, and W at around 6.5, 7.5, and 8.5 keV, respectively.

In addition to EDS for phase mapping, the SEM was used for high magnification imaging using the backscattered electron (BSE) detector to highlight the difference in elements and grain orientation for easy determination of W grain size. These images were then analyzed visually to estimate W grain size as a function of milling time and sintering temperature.

3.3.2.4 Hardness Testing

Microhardness and macrohardness testing were used to assess mechanical properties on both the macro and micro scales, as a function of sintering parameters. A LECO DM-400 Vickers microhardness tester was used at 1,000 gf for 10 seconds. At least ten tests were run per sample, with more runs on some samples to reduce the range of the 95% confidence interval. A LECO LV700AT Vickers hardness tester was used at 10 kgf for 10 seconds. At least six tests were run per sample, with more runs on some samples to reduce the range of the 95% confidence interval based on the t-statistic shown in Equation 7 below.

$$95\%\ CI = \bar{X} \pm t * \frac{S}{\sqrt{n}} \qquad \text{Eq. 7 [57]}$$

where $\bar{X}$ is the sample mean, t is the t-statistic based on the number of tests in the sample, S is the sample standard deviation, and n is the number of tests in the sample.

Chapter 4

4. Results

Chapter 4 presents the data and results gathered by the experimental methods described in Chapter 3 with limited analysis and discussion of their importance and correlation with one another. Chapter 5 provides more extensive discussion and analysis of the results to tie together the importance of different findings into a complete picture of the powder processing of W-3Ni-1Fe.

4.1 Powder Characterization

4.1.1 Particle Size Analysis

As described in Chapter 3 above, particle size analysis was performed to assess the particle size distribution as a function of milling time. This information was then used to explain and understand observations of densification and microstructure as a function of milling time. Figure 14 shows a typical plot of both the cumulative and regular distribution of unmilled W-3Ni-1Fe powder with size on the x-axis and frequency on the y-axes. Figure A1.1 of Appendix A contains data from all three runs for the unmilled powder. The regular distribution curve features one fairly narrow peak centered at a size of about 40 µm, which is consistent with the mesh sizes provided by the powder manufacturer. Observation of the cumulative distribution peak indicates that about 90% of the particles are between 20 and 70 µm in size.

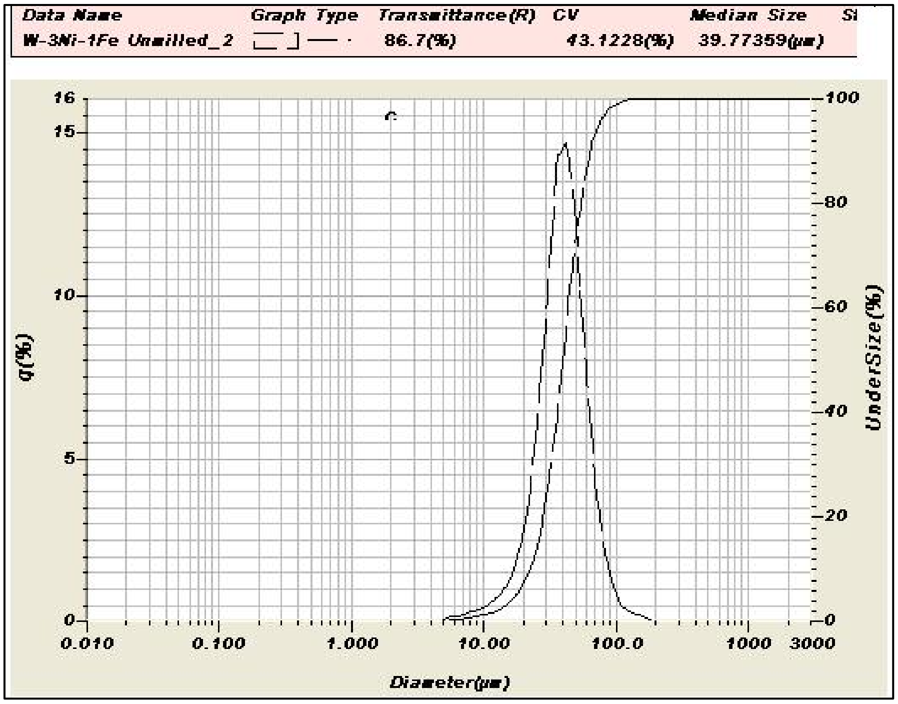

Figure 14 Unmilled W-3Ni-1Fe particle size distribution

Particle size distribution curves were produced for all four milling times: 15, 25, 50, and 100 hours. Figure 15 shows all four milling times on one graph, while Figures A1.2-5 of Appendix A show plots of each milling time separately, but with all of the data generated from the three or more runs for each milling time. Figure 15, which summarizes the milling effects, shows an uneven bimodal size distribution. Most of the particles are in the peak indicating a smaller size between 1 and 10 µm, while approximately 20% of the particles are in the peak indicating a larger size of 50 to 150 µm. The general distribution shape is consistent for all four milling times, with some evidence of a slight shifting to the left (indicating a size decrease) of both peaks with increased milling time. For the peak indicating smaller size, the center shifts from approximately 5 µm at 15 hours to closer to 3 µm at longer milling times, largely due to broadening in the region of 1 to 2 µm particles. The second peak similarly shifts to the left from a center of 90 to 100 µm after 15 hours milling to closer to 75 µm at longer milling times, but without as much broadening.

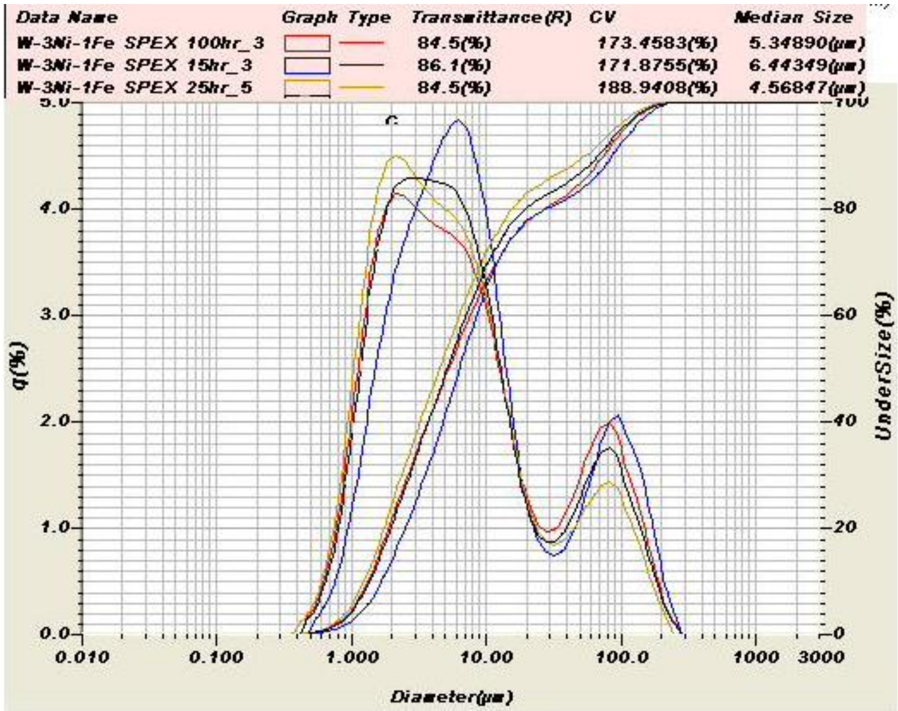

Figure 15 Milled W-3Ni-1Fe particle size distributions: 15 hours in blue, 25 hours in yellow, 50 hours in black, 100 hours in red

4.1.2 Scanning Electron Microscopy (SEM)

To augment the knowledge of particle size and morphology and confirm the particle size analysis results, SEM was used to image powder particles from each milling time. Figure 16 shows the unmilled W-3Ni-1Fe powder, while Figures A2.1-2 in Appendix A show additional SEM micrographs of the unmilled powder. Figure 16 shows a collection of particles consistent with the particle size distribution shown in Figure 14, with equiaxed particles mostly in the size range of 20 to 70 µm.

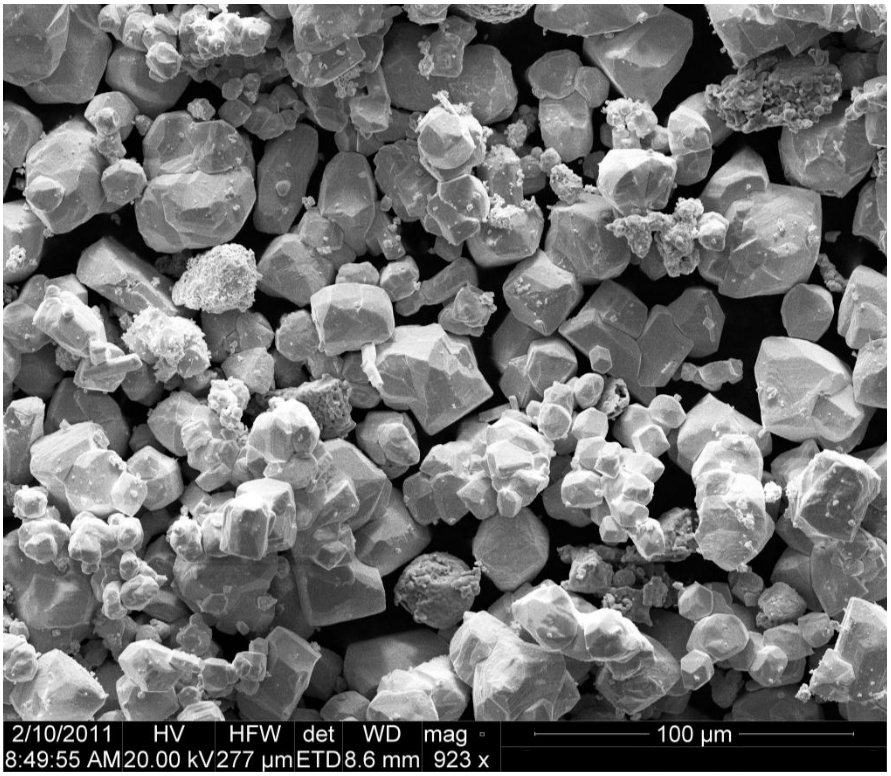

Figure 16 Unmilled W-3Ni-1Fe powder particles

Figures 17-20 show SEM micrographs of powder milled for 50 hours to provide an idea of the particle sizes and morphologies in the milled powders. Figure 17 is a low magnification image showing a large particle greater than 100 µm in size as well as some medium sized particles of maybe 20 to 40 µm in size covered and surrounded by many smaller particles on the order of <1 to 10 µm. Figure 18 shows that same large particle at higher magnification to clearly show the surface of the particle covered in smaller particles. Figure 19 is of still higher magnification focusing on the medium-sized particles covered in small particles. Figure 20 shows a high magnification image of the smallest particles with sizes ranging from <1 to 10 µm with fairly equiaxed, smooth morphology. SEM did not show significant variation in the size distribution or morphology of the particles with increasing milling time, which is consistent with the slight changes in particle size distribution with increasing milling time observed via particle size analysis. Additional images of powder from other milling times can be found in Figures A2.3-13 of Appendix A.

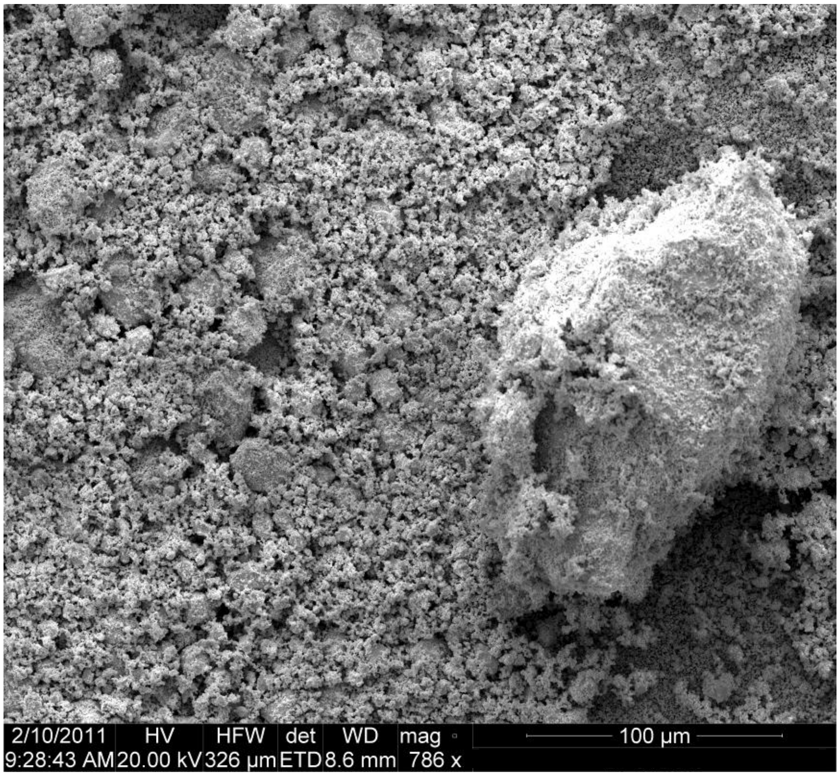

Figure 17 Large, medium, and small 50-hour milled W-3Ni-1Fe powder particles

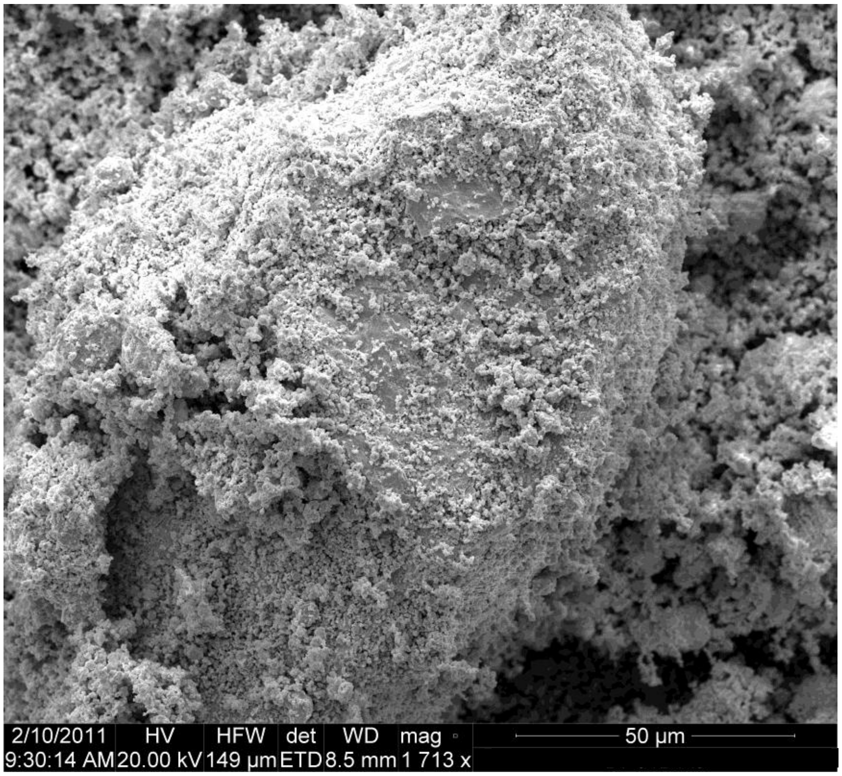

Figure 18 Large 50-hour milled W-3Ni-1Fe powder particle covered in small particles

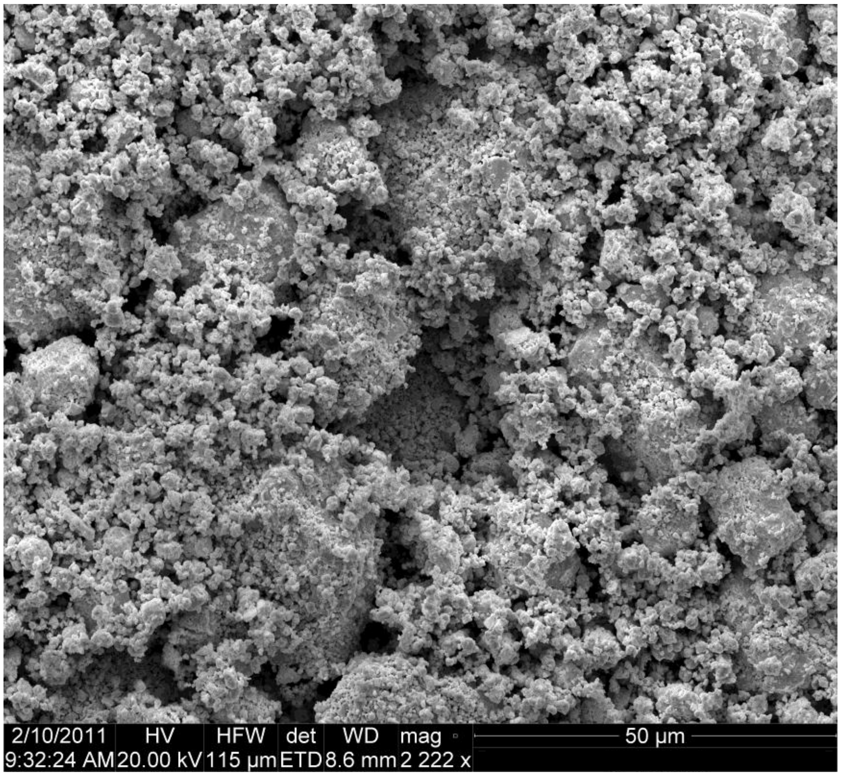

Figure 19 Medium-sized 50-hour milled W-3Ni-1Fe powder particles covered in small particles

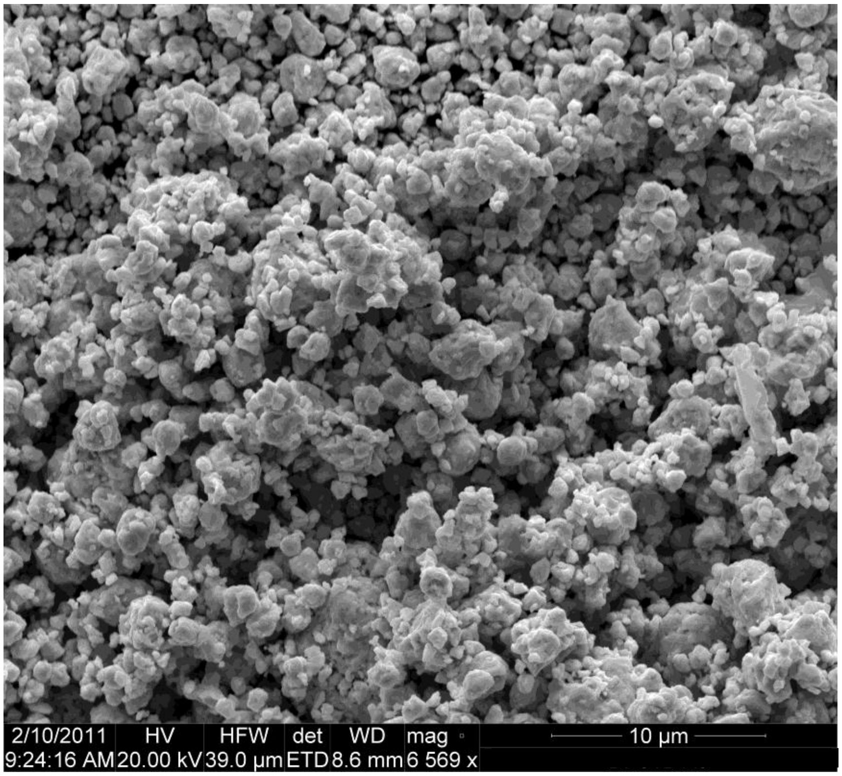

Figure 20 Smallest 50-hour milled W-3Ni-1Fe powder particles

To better understand the differences between the small and large particles, point-based EDS analysis was used to observe compositional differences in the two particle sizes as a function of milling time as shown in Figure 21 for powder milled for 25 hours. For this analysis, points were selected on SEM images to measure small or large powder particles by EDS. As can be seen below, one point is selected from a very large particle in the left image, while another point is selected in a region of very small particles in the right image. The large particle appears to contain slightly less Ni/Fe and more W compared to the small particles adjacent to it. This observation is consistent for a variety of areas on three different milled powders that were observed. Table 3 shows the average ratio compositions of small and large particles from three different samples based on at least three samples of each particle size for each milling time.

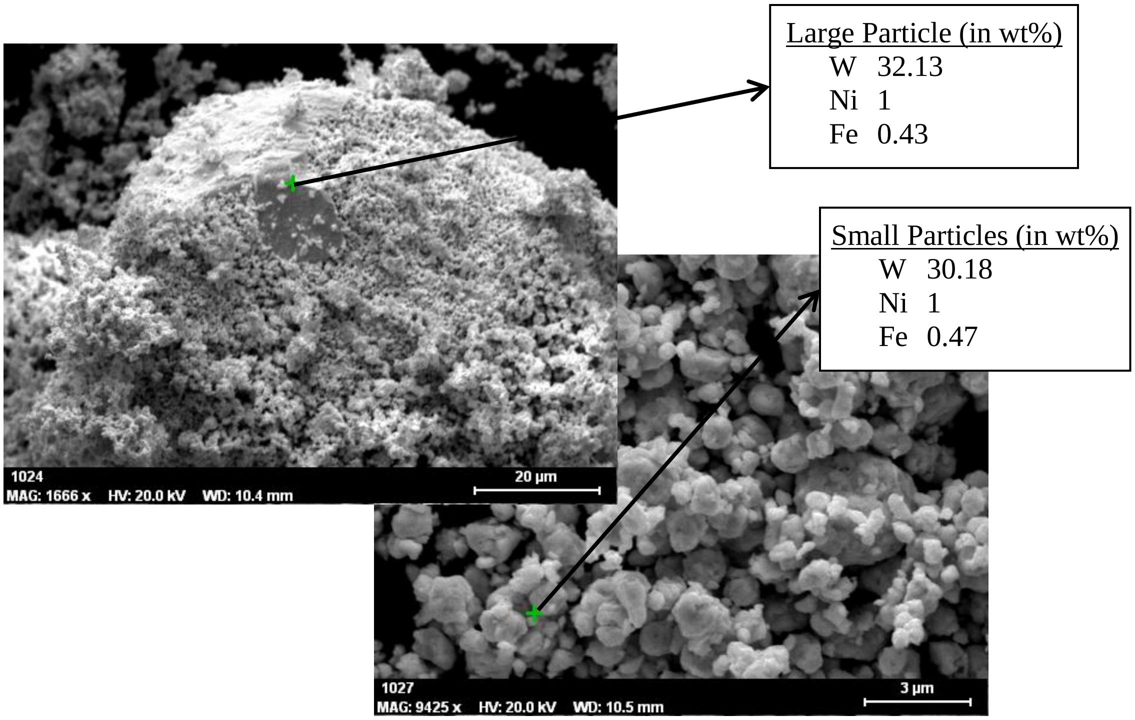

Large Particle (in wt%)
W 32.13
Ni 1
Fe 0.43

Small Particles (in wt%)
W 30.18
Ni 1
Fe 0.47

Figure 21 Example on 25 hour milled powder of point-based EDS to compare large and small milled powder particles compositionally

Table 3: Large vs. Small Powder Particles Point-Based EDS Composition Readings

Ratios relative to Ni in wt%	Sample	15 hours mill	25 hours mill	50 hours mill
Large Particles	Avg. W:Ni	33.85	32.14	34.25
	Avg. Ni:Ni	1	1	1
	Avg. Fe:Ni	0.74	0.41	0.72
Small Particles	Avg. W:Ni	30.42	30.80	28.03
	Avg. Ni:Ni	1	1	1
	Avg. Fe:Ni	0.63	0.46	0.65
Difference (Large - Small)	Avg. W:Ni	3.43	1.34	6.22
	Avg. Ni:Ni	0	0	0
	Avg. Fe:Ni	0.11	-0.05	0.07

Table 3 shows an increasing disparity in W:Ni ratio of the small vs. large-grained regions with increasing milling time. While this trend is not completely consistent, it is interesting to observe with increasing milling time. Figure 22 shows the difference in W:Ni ratio in wt% between the small and large particles as a function of milling time.

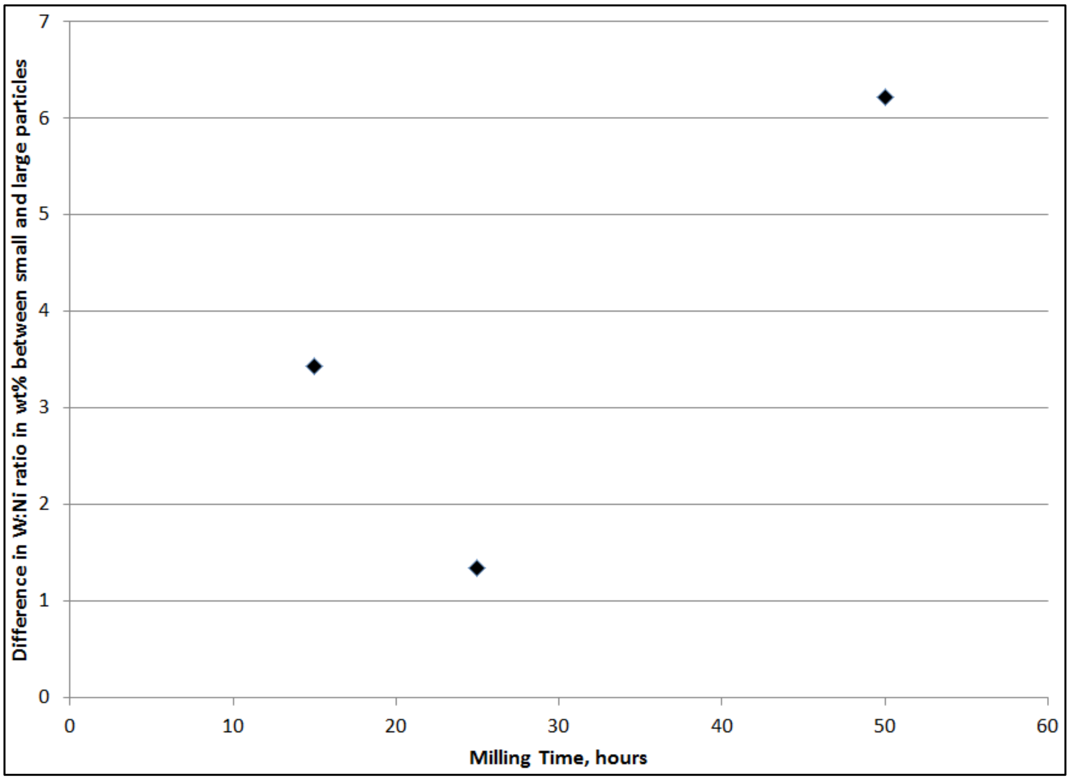

Figure 22 Plot of difference W:Ni ratio in wt% W between small and large particles as a function of milling time

4.1.3 X-Ray Diffraction (XRD)

XRD was used extensively for powder characterization to assess the effects of milling time on the material structure. These analyses included peak shifting to determine lattice parameter, as well as peak broadening analyzed by the Williamson-Hall method to separate the effects of strain and crystallite size. Full XRD curves of unmilled, 15, 25, 50, and 100 hour milled powders can be seen in Figure A3.1 in Appendix A showing crystalline W, Ni and Fe in the unmilled powders, but only broadened W peaks in milled powders, indicating the dissolution and disappearance of the crystalline Ni and Fe phases as a result of milling.

4.1.3.1 Lattice Parameter

As described in Chapter 3, XRD peak position indicates the lattice parameter of the phase generating the peak. For our samples, the W peaks show an interesting evolution in peak position with increasing milling time. Figure 23 shows XRD curves of unmilled, 15, 25, 50, and 100 hour milled powders focused on the main W peak at about a Bragg angle of 40°, which demonstrates this trend qualitatively. The W peaks shift to the right (to higher diffraction angles) with increasing milling time, indicating a reduction in the lattice parameter of the crystalline W BCC phase.

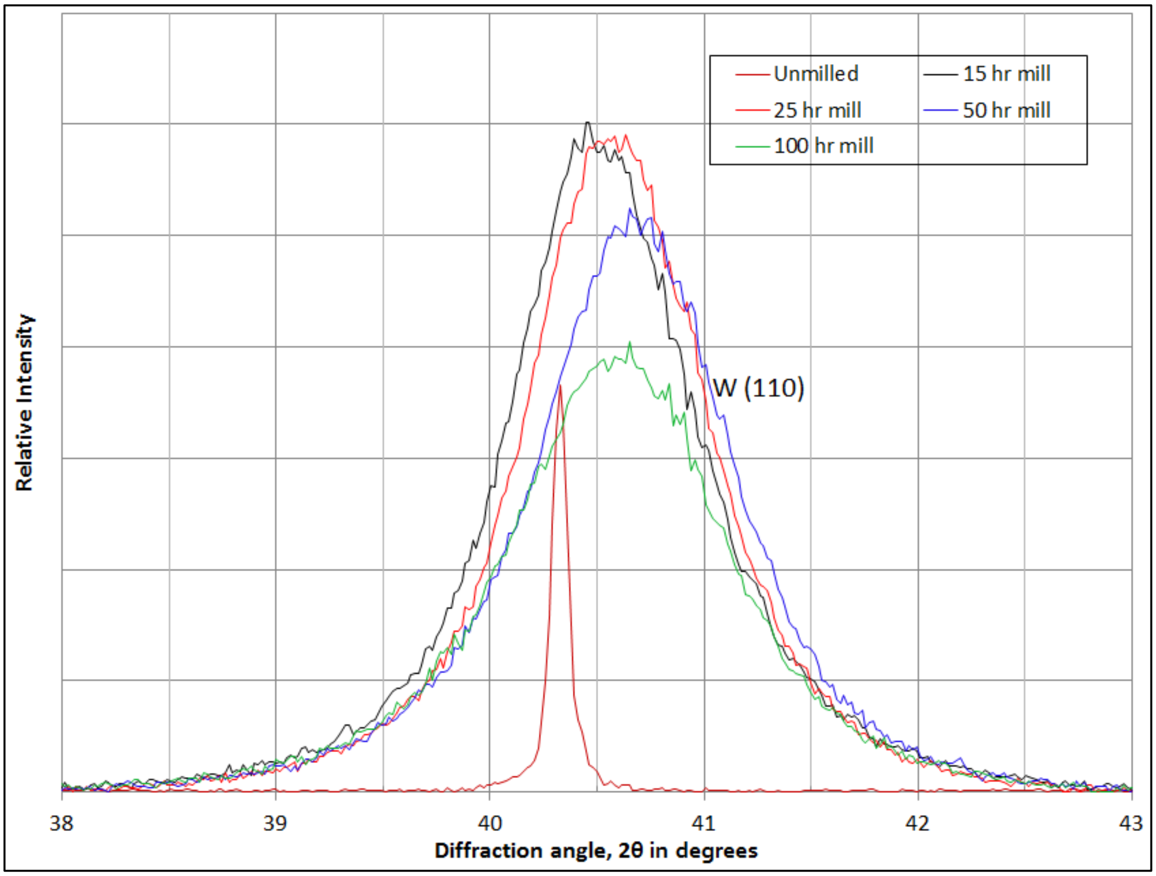

Figure 23 XRD curves focused on the main W peak for all powder samples both unmilled and milled for 15, 25, 50, and 100 hrs (Intensity scale much greater for unmilled sample for visual purposes)

Figure 24 provides a graphical representation of lattice parameter of the W phase as a function of milling time. Each data point was averaged from data for eight W peaks (four peaks from two runs each as described in Chapter 3). This trend clearly shows the lattice parameter decreasing, which as described in Chapter 3, is likely due to the dissolution of Ni and Fe in W. Full analysis and discussion of the correlation of lattice parameter reduction to Ni and Fe dissolution into W appears later in Chapter 5.

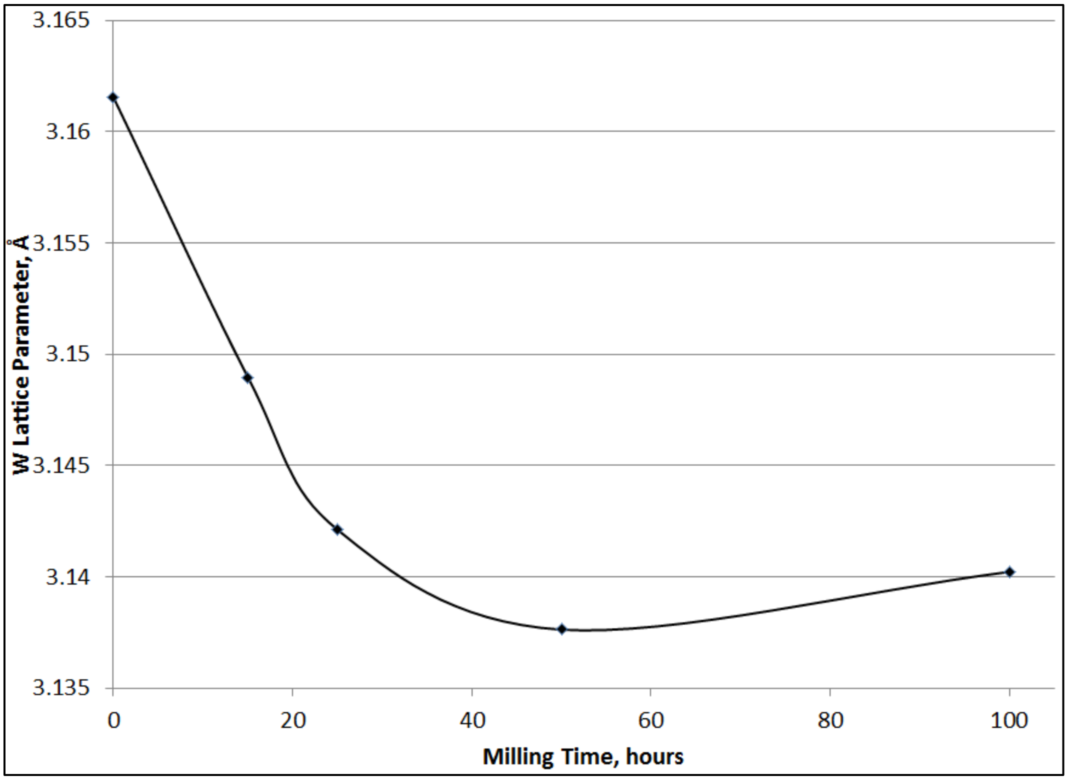

Figure 24 W lattice parameter inferred from XRD peak position as a function of milling time

4.1.3.2 Williamson-Hall Plots

Williamson-Hall plots, which separate the peak broadening effects of lattice strain and crystallite size as described in Chapter 3 were generated to estimate the change in strain and crystallite size as a function of milling time. Due to the coarse-grained nature of the unmilled powders, a reliable estimate of crystallite size was not able to be made as the Scherrer equation only provides a valid approximation for values <100 nm. The strain in the unmilled powder was estimated by the Williamson-Hall method to be very low compared to the milled powders with a value of 0.21%. Figure 25 shows the lattice strain inferred from peak broadening by the Williamson-Hall method as a function of milling time for 15, 25, 50, and 100 hours milling (but not unmilled due to difficulty of displaying the much lower value). This plot shows a slight, but steady increase in lattice strain with increasing milling time, which may be logarithmic in nature as evidenced by the logarithmic best-fit line superimposed on the plot.

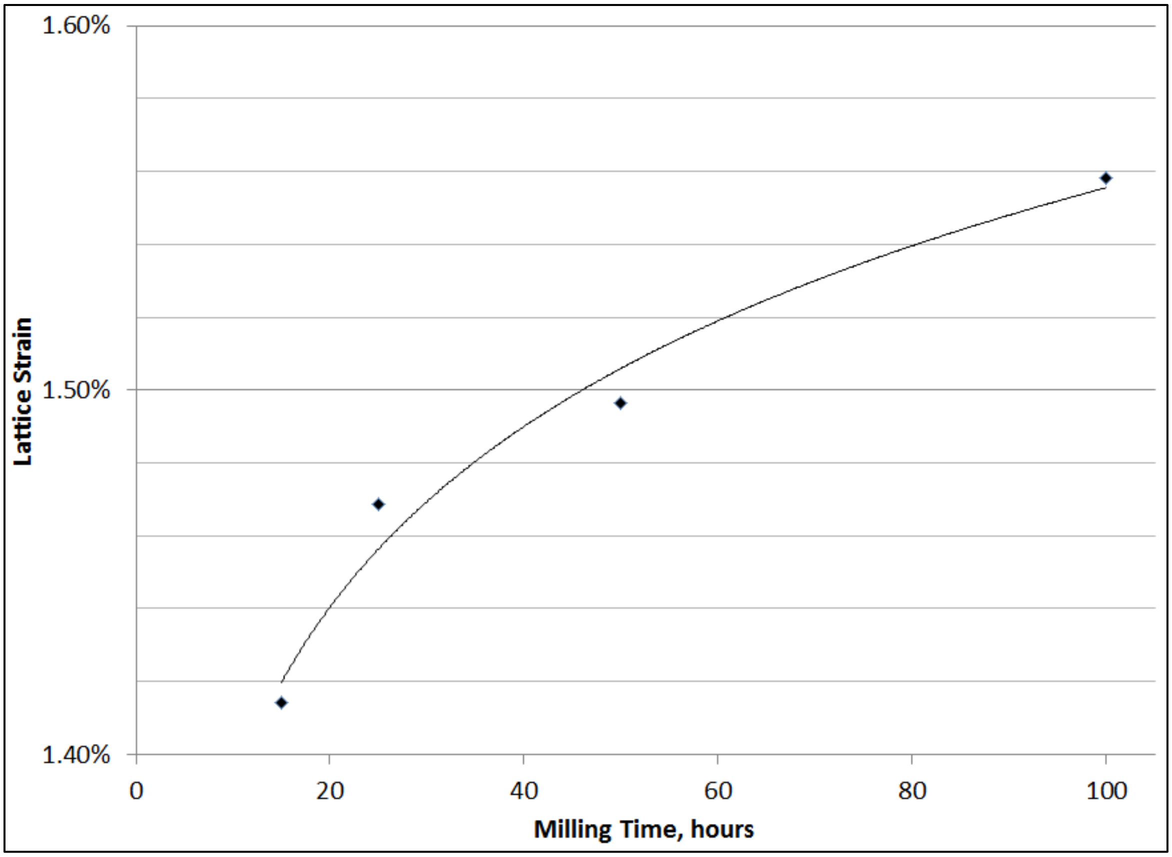

Figure 25 W lattice strain inferred from XRD peak broadening as a function of milling time

Figure 26 shows the trend of crystallite size as a function of milling time for all four milling times. Crystallite size likewise shows a slight, but steady decrease with increasing milling time, dropping from almost 45 nm at 15 hours milling to below 25 nm at 100 hours milling. The correlation appears to be almost linear, as illustrated by the superimposed linear best-fit line. This indicates that high-energy ball milling is continuing to refine grain size up to 100 hours of milling.

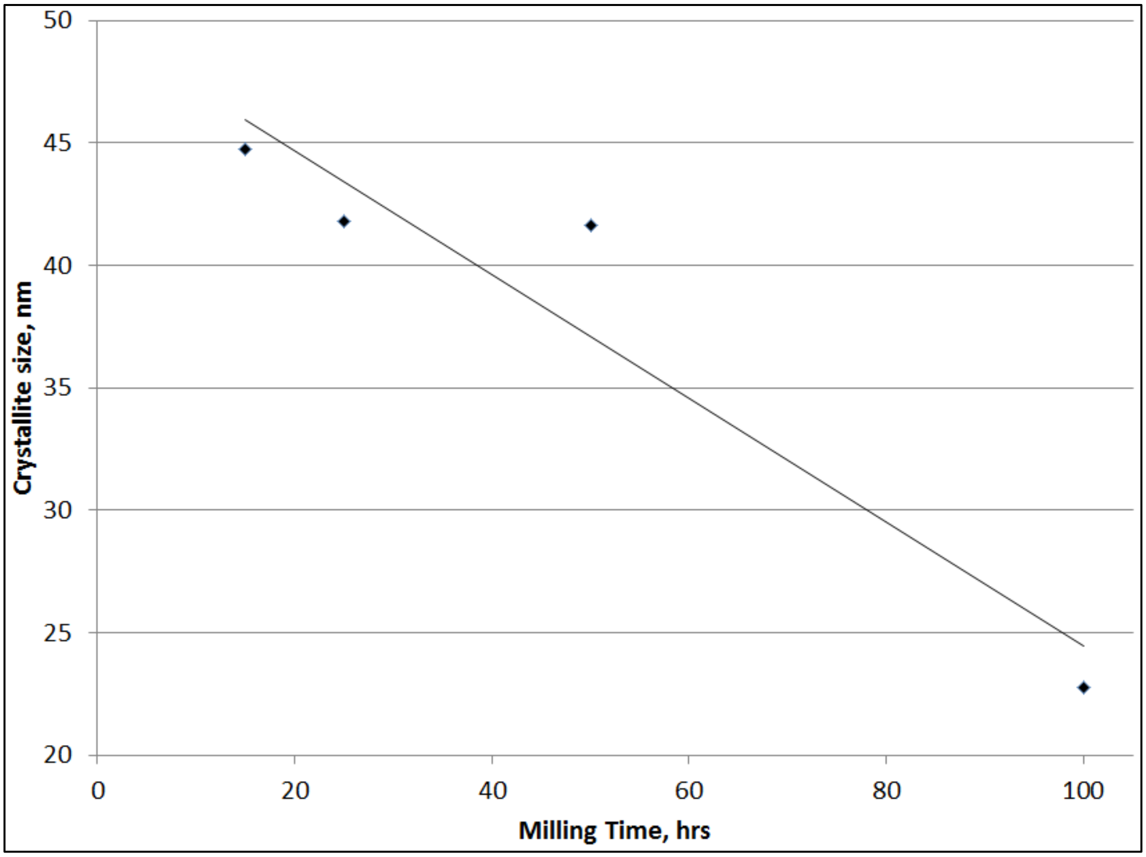

Figure 26 W crystallite size inferred from XRD peak broadening as a function of milling time

4.2 Bulk Characterization

After compaction and sintering, bulk samples were characterized by density measurement, X-ray diffraction, SEM, and hardness testing to assess densification, microstructure, and mechanical properties as described in Chapter 3.

4.2.1 Density Measurements

4.2.1.1 Green Density

Density was measured by calipers to estimate volume before sintering and by Archimedes' density after sintering. Caliper densities were used on CIPed, pre-sintering samples to assess the effect of the 300°C recovery heat treatment (HT) on pre-sintered green density. Figure 27 compares CIPed density as a fraction of theoretical density with and without the recovery heat treatment over the three milling times: 15, 25, and 50 hours. Each data point is the average of measurements on three samples (each being destined for a different sintering temperature as seen in Table 1 of Chapter 3). There is a strong decrease in green density with increasing milling time, which may be explained by milling effects. The data also shows a slight, but significant increase in green density following the recovery HT. This increase also appears to be greater at the longer milling times of 25 and 50 hours.

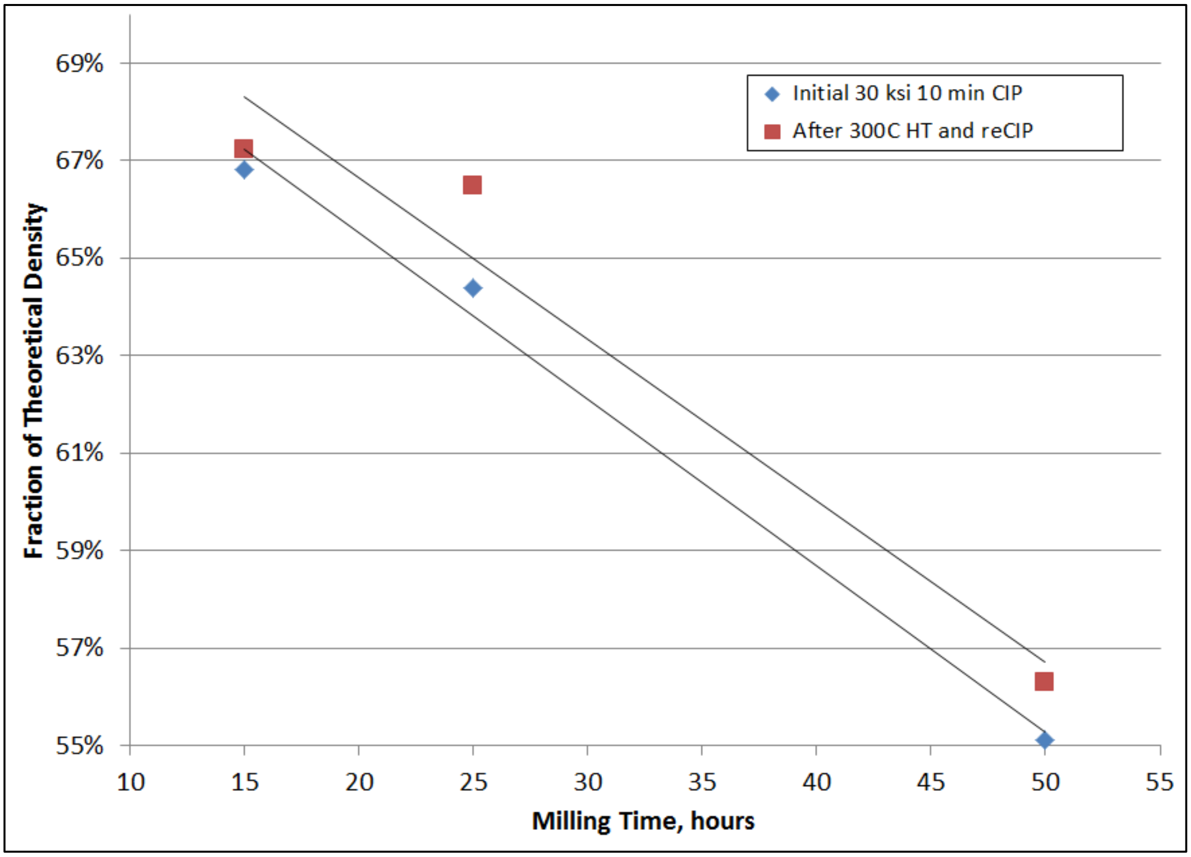

Figure 27 Effect of recovery HT on green density as a function of milling time

While useful for pre-sintered density measurements to qualitatively assess the effect of the recovery HT, caliper measurements were not considered to be very accurate or precise due to the difficulty in judgment of the dimensions as well as the imperfections in shape relative to an ideal cylinder. Therefore, while caliper measurements were made on most samples before and after sintering, for sintered samples only Archimedes' density values were reported due to the greater confidence in the reliability and accuracy of the results. Full tables of density results can be seen in Appendix B.4.

4.2.1.2 Sintered Density

Before investigating more moderate times and temperatures, a few samples were run to higher temperatures and times (1300°C for 25 hours and 75 hours as presented in Table 1 in Chapter 3) to assess the pragmatism of the theoretical density calculations as well as to observe the practical limits of densification in pressureless sintering under hydrogen atmosphere. Unlike in vacuum sintering, 100% density is not expected due to the presence of hydrogen gas molecules in closed porosity during final sintering as discussed in Chapter 2. Figure 28 plots Archimedes' sintered densities as a fraction of theoretical density observed for two sintering runs as a function of milling time.

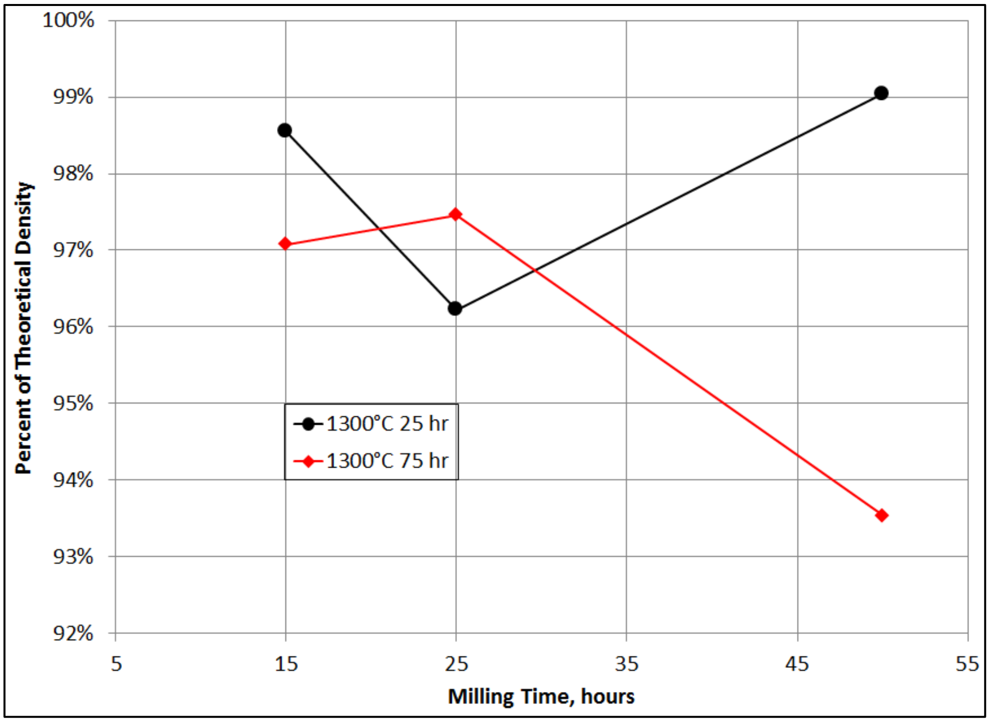

Figure 28 High-temperature sintered density as a function of milling time

Five of the six samples show densities greater than 96%, but less than 100% as would be expected. The exception is the 50-hour milled, 1300°C 75-hour sintered sample, which showed an abnormally low density indicative of a possible outlier. Somewhat surprisingly, the shorter sintering time provides similar, if not greater, densification than longer sintering time. This probably shows that densification has been essentially completed by the shorter time, with no significant densification occurring after that time and statistical variation explaining most of the difference in the two sets of densities. This data also seems to confirm at least the approximate accuracy of the calculated theoretical density, with most of the values falling in the expected range of 96-100%, indicating almost full densification. The lack of increase in density at longer sintering time provides evidence that there is no further densification to be achieved after 25 hours at 1300°C.

Archimedes' densities were measured for the nine samples sintered for the primary test matrix of sintering for 1 hour at 1000, 1100, and 1200°C after milling for 15, 25 and 50 hours. Figure 29 shows the density as a fraction of theoretical density for the three milling times as a function of sintering temperature. For a different perspective on the results, Figure 30 shows the same data as a function of milling time, rather than sintering temperature. Figures 29 and 30 both show the dominant factor in sintered density to be sintering temperature, with increasing milling time having only a minor, but fairly consistent effect. Density increases from about 84-85% at 1000°C to 88-89% at 1100°C and 92-93% at 1200°C. Another slight, yet steady trend appears be greater density after milling for 50 hours (although 1100°C doesn't follow this, the other two temperatures do) as compared to the other two milling times.

At 1000°C and 1200°C sintering temperatures, the 50 hour milled samples are 1.5 to 2% greater in percent of theoretical density than the 15 and 25 hour milled samples. Meanwhile, 15 hours milled samples show the second highest density, but only slightly higher at about 0.5% greater than the 25 hours milled samples, which appeared to densify the least.

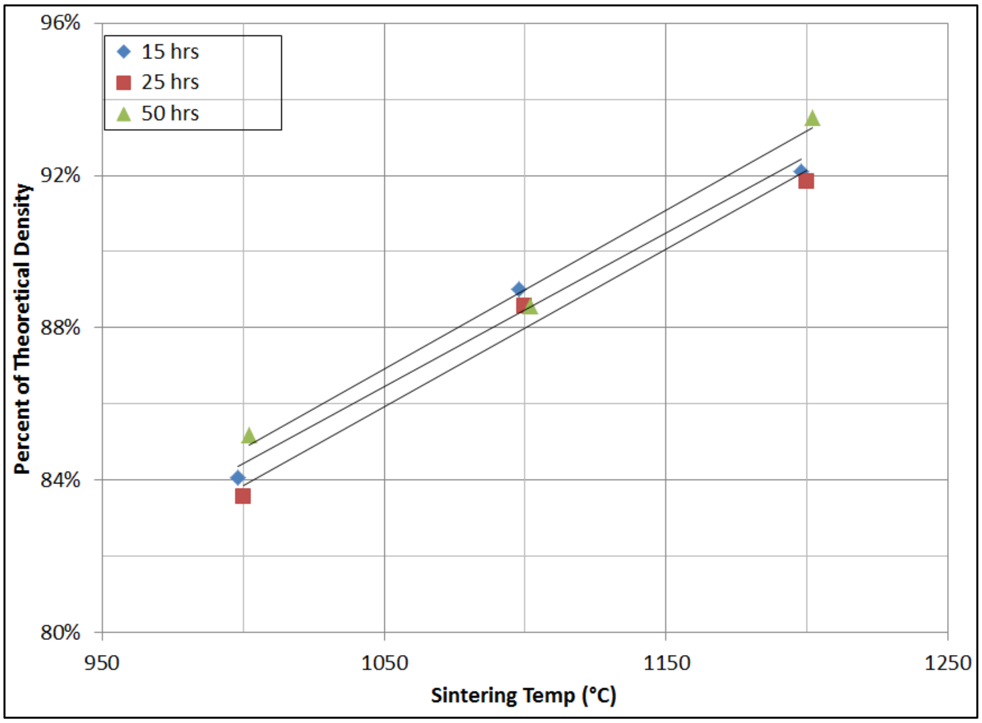

Figure 29 Density after 15, 25, and 50 hours of milling as a function of sintering temperature

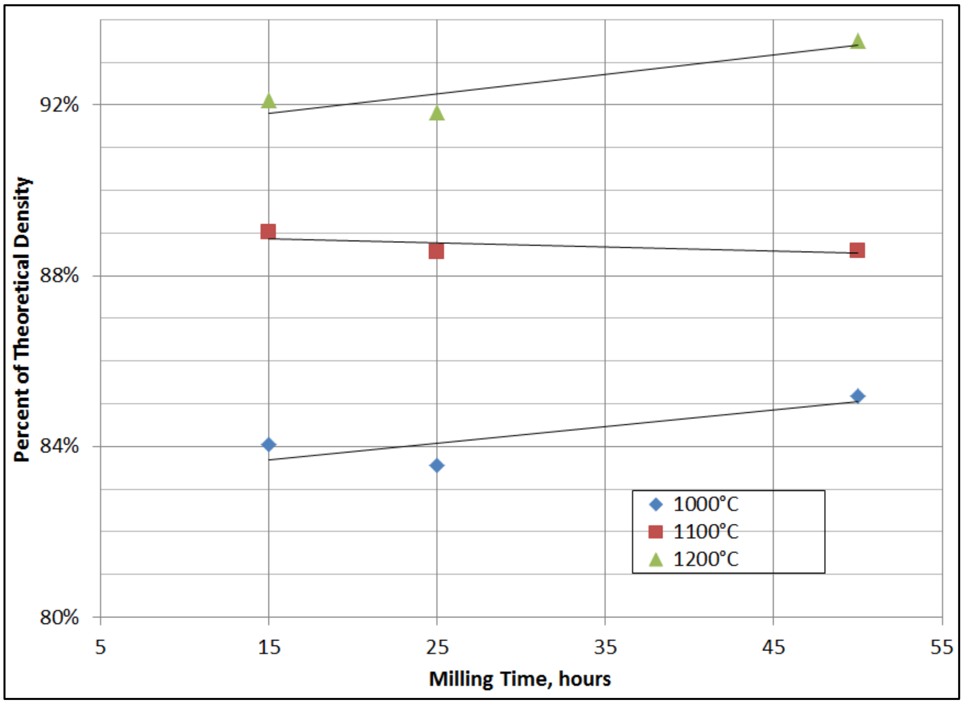

Fig. 30 Sintered density as a function of milling time for 1000, 1100, and 1200°C sintering temperatures

4.2.1.3 Activation Energy

Green and sintered Archimedes densities were used for further analysis to examine apparent activation energy for sintering and sintering exponent as a function of milling time. These calculations were made to demonstrate quantitatively and empirically the sintering rate as a function of milling time. For this analysis, the shrinkage $(\frac{\Delta L}{L_o})$ is calculated from the green and sintered densities as shown below in Equation 8 [37].

$$\frac{\Delta L}{L_o} = 1 - (\frac{\rho_g}{\rho_s})^{1/3} \qquad \text{Eq. 8 [37]}$$

With the shrinkage value for each milling time and sintering temperature, an Arrhenius plot of $\ln \frac{\Delta L}{L_o}$ as a function of 1/T, where T is the absolute temperature, was generated for each milling time. Equation 9 shows how the slope of this plot is equal to the apparent activation energy (E_a) divided by the gas constant (R) with A representing a pre-exponential constant. A linear best-fit line was generated for each milling time and the slope used to calculate the apparent activation energy as a function of milling time.

$$\ln \frac{\Delta L}{L_o} = \ln A - \frac{E_a}{R}(\frac{1}{T}) \qquad \text{Eq. 9}$$

Figure 31 shows the natural logarithm of shrinkage as a function of the inverse of absolute temperature. All three linear fits show correlations of greater than 95%. The slope of each line is the activation energy divided by the gas constant, which allows for empirical calculation of the sintering activation energy as a function of milling time as shown in Figure 32. These results show a strong reduction in apparent activation energy as a function of increasing milling time, which is discussed in greater detail in Chapter 5. Activation energy is suspected to be correlated to the dissolution Ni/Fe into W. Therefore, Figure 33 was generated plotting apparent activation energy as a function of W lattice parameter after milling. As lattice parameter decreases, Ni/Fe dissolution increases, which appears to decrease apparent activation energy. A positive relationship between lattice parameter and apparent activation energy is observed as expected.

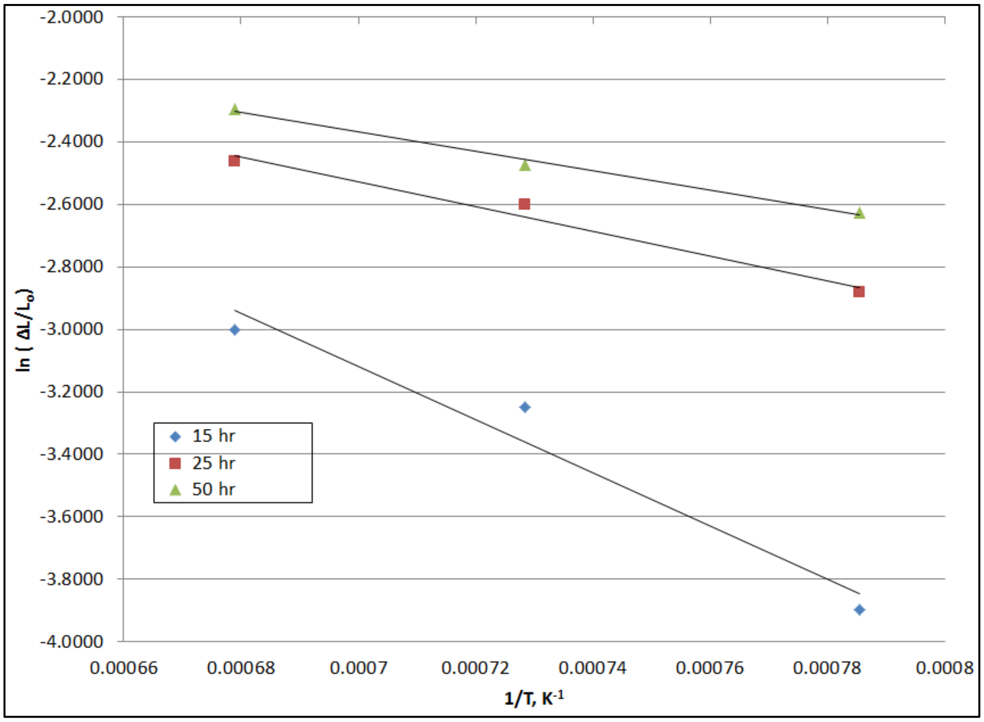

Figure 31 Arrhenius plot of logarithm of shrinkage as a function of inverse absolute temperature for the three milling times

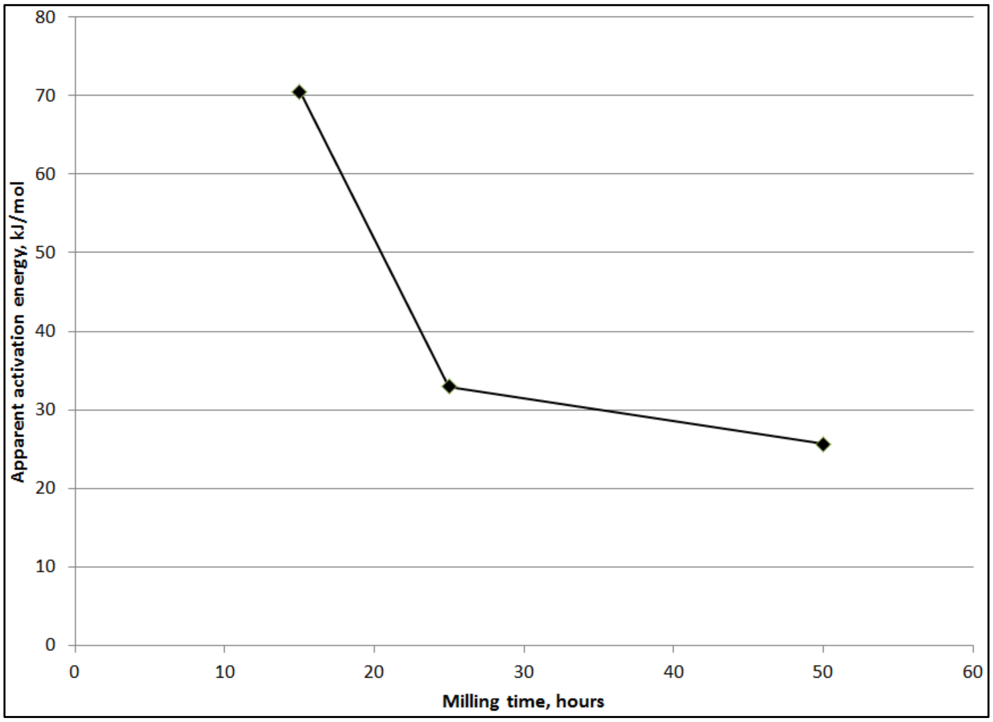

Figure 32 Apparent activation energy for diffusion during sintering of W as a function of milling time

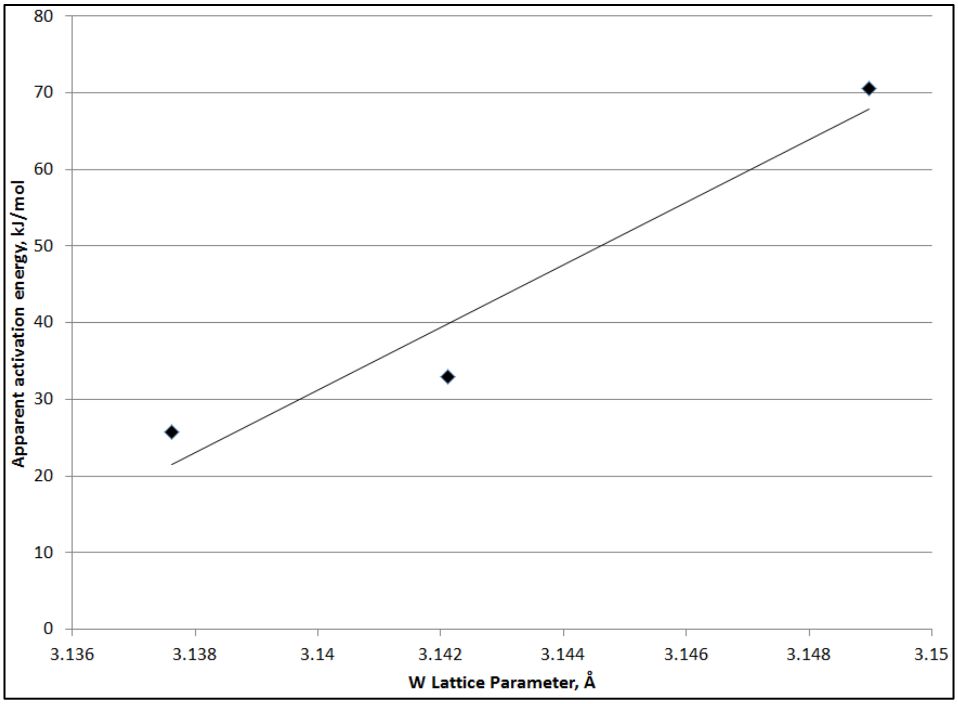

Figure 33 Apparent activation energy for diffusion during sintering of W as a function of W lattice parameter after milling

4.2.1.4 Sintering Exponent

The sintering exponent (m) requires a bit more involved derivation beginning with Equations 10 and 11 from Boonyongmaneerat [43] below for the initial stage of sintering.

$$\frac{\Delta L}{L_o} = (\frac{Kt}{T})^m \qquad \text{Eq. 10}$$

where t is time, T is absolute temperature, and K is a diffusion coefficient.

$$K = B\exp(\frac{-E_a}{RT}) \qquad \text{Eq. 11}$$

where B is a constant relating to diffusivity, surface energy, atomic volume, and particle size, R is the gas constant, E_a is the activation energy (previously calculated), and T is the absolute temperature.

When the logarithm of the result of the combination of these equations is taken, Equation 12 is produced, in which m is the slope of a plot of $\ln\frac{\Delta L}{L_o}$ as a function of $\ln\frac{e^{\frac{-E_a}{RT}}*t}{T}$, where $m*\ln B$ is assumed to be constant as sintering temperature changes. Therefore, this plot was made and the slope calculated using a linear best-fit to calculate the sintering exponent, m.

$$\mathbf{ln}\frac{\Delta \boldsymbol{L}}{\boldsymbol{L_o}} = \boldsymbol{m} * \mathbf{ln}\,\boldsymbol{B} + \boldsymbol{m} * \mathbf{ln}\frac{\boldsymbol{e}^{\frac{-E_a}{RT}}*\boldsymbol{t}}{\boldsymbol{T}} = (m*\ln Bt) + m(\frac{-E_a}{RT} - \ln T) \qquad \text{Eq. 12}$$

Figure 34 shows the plot of the logarithm of shrinkage versus a more complex term involving activation energy, temperature, and time to infer the sintering exponent. The slopes of the curves in

Figure 34 are equal to m and all are fit with at last 95% correlation. This leads to Figure 35, which plots the sintering exponent as a function of milling time below. As milling time increases, the sintering exponent increases strongly from around 1.2 to almost 1.8, indicating an increase in the rate of sintering.

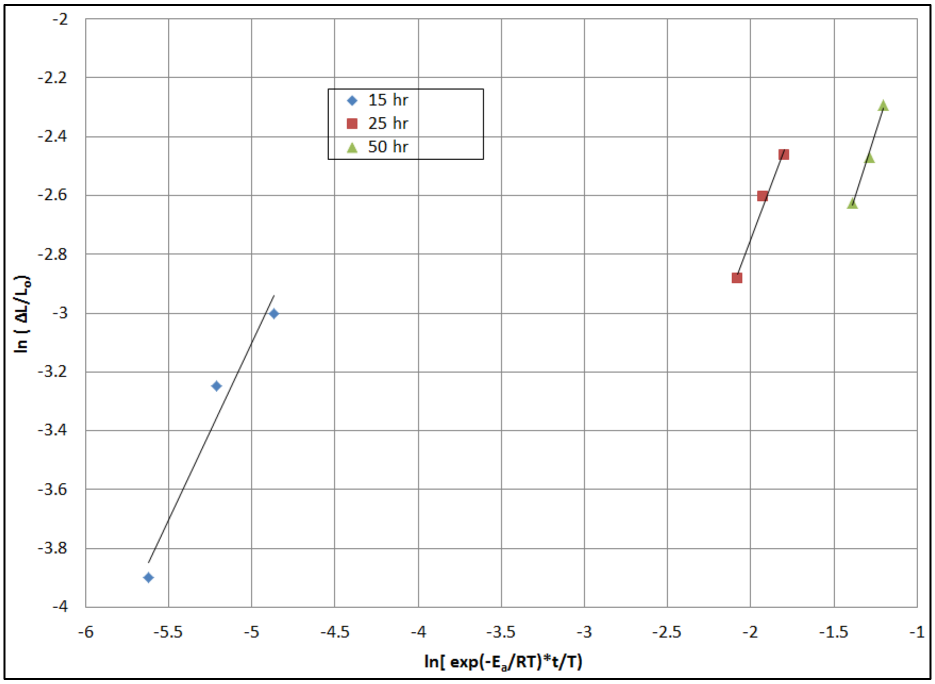

Figure 34 Plot of logarithm of shrinkage as a function of a more complex term involving activation energy, temperature, and time for the three milling times

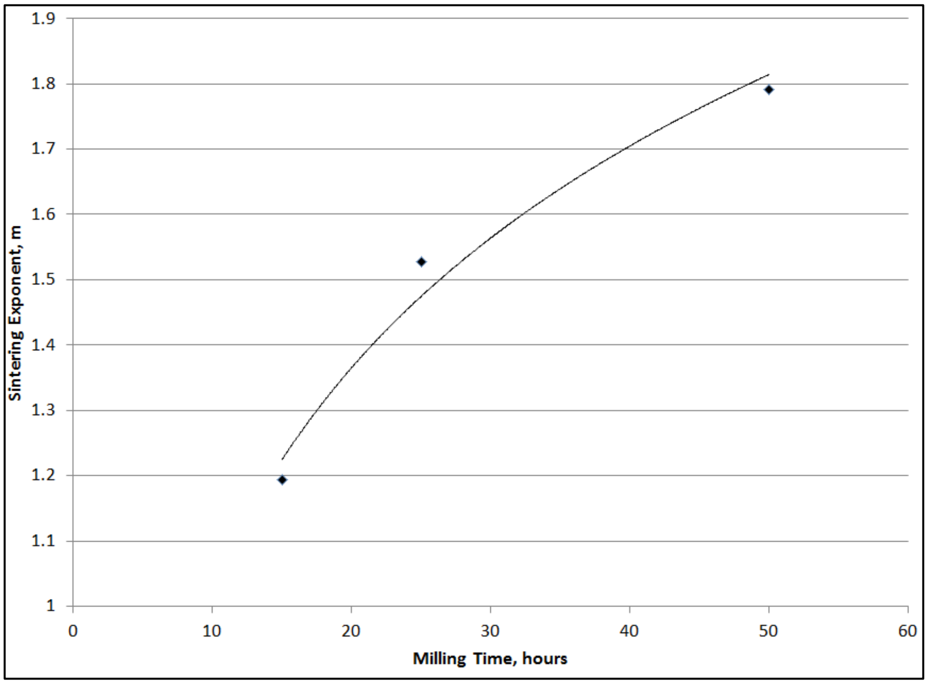

Figure 35 Sintering exponent as a function of milling time

Lattice strain represents stored energy in the lattice, which can be a driving force for sintering. Therefore, Figure 36 was generated plotting sintering exponent as a function of XRD-inferred lattice strain. The resulting plot provides a good linear trend with a correlation of greater than 98%.

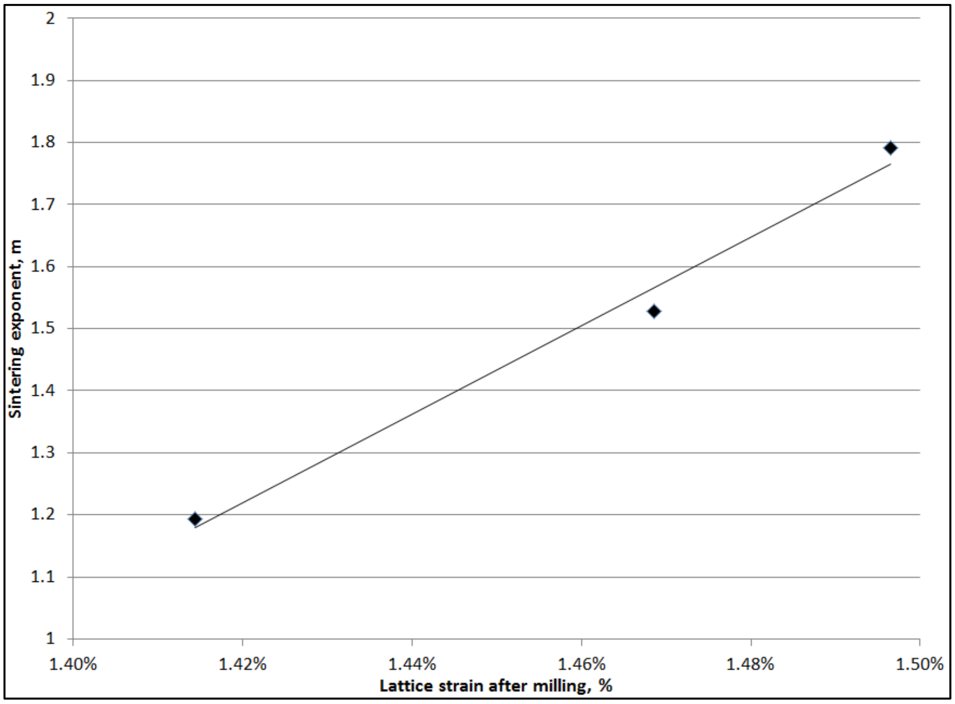

Figure 36 Plot of sintering exponent as a function of lattice strain after milling

4.2.2 X-ray Diffraction

All sintered samples were run in the X-ray diffractometer after cutting to assess phases present through peak identification as well as to look for any peak shifting or broadening. W peak shifting and broadening were not very informative. All peaks shifted back to near their original position, and while there was some variation in peak position as a function of milling time and sintering temperature trends were not clear or consistent. Likewise, W peaks, which had broadened considerably and were analyzed by the Williamson-Hall method for strain and crystallite size in the milled powders earlier in this chapter, narrowed greatly due to recrystallization and grain growth and did not yield useful data or trends.

The most useful information from XRD for bulk sintered samples was identifying the presence of precipitated secondary phases through peak identification. XRD results indicate the presence of two secondary phases. One of these phases is confidently identified as Fe_6W_6C, which is an intermetallic phase incorporating carbon introduced to the system through the milling process. The other set of peaks (of lower intensity than the Fe_6W_6C peaks) seems to match with two potential phases: Ni_3Fe intermetallic or a crystalline FCC Ni phase. Figure 37 shows the XRD curves for the 50 hour milled samples for all five heating runs. Figures B1.1 and B1.2 in Appendix B show the curves for the 15 and 25 hour milled samples, respectively, for all five heating runs each. The 1300°C runs show the secondary phase peaks clearly, while the lower temperatures show diffuse humps in the areas where discrete peaks later form, indicating the presence of these peaks in all samples, but their coarsening into sharp peaks and increase in volume fraction only at higher temperatures with longer hold times. At lower temperatures, these phases are likely only very fine precipitates, leading to broadening effects from their small size.

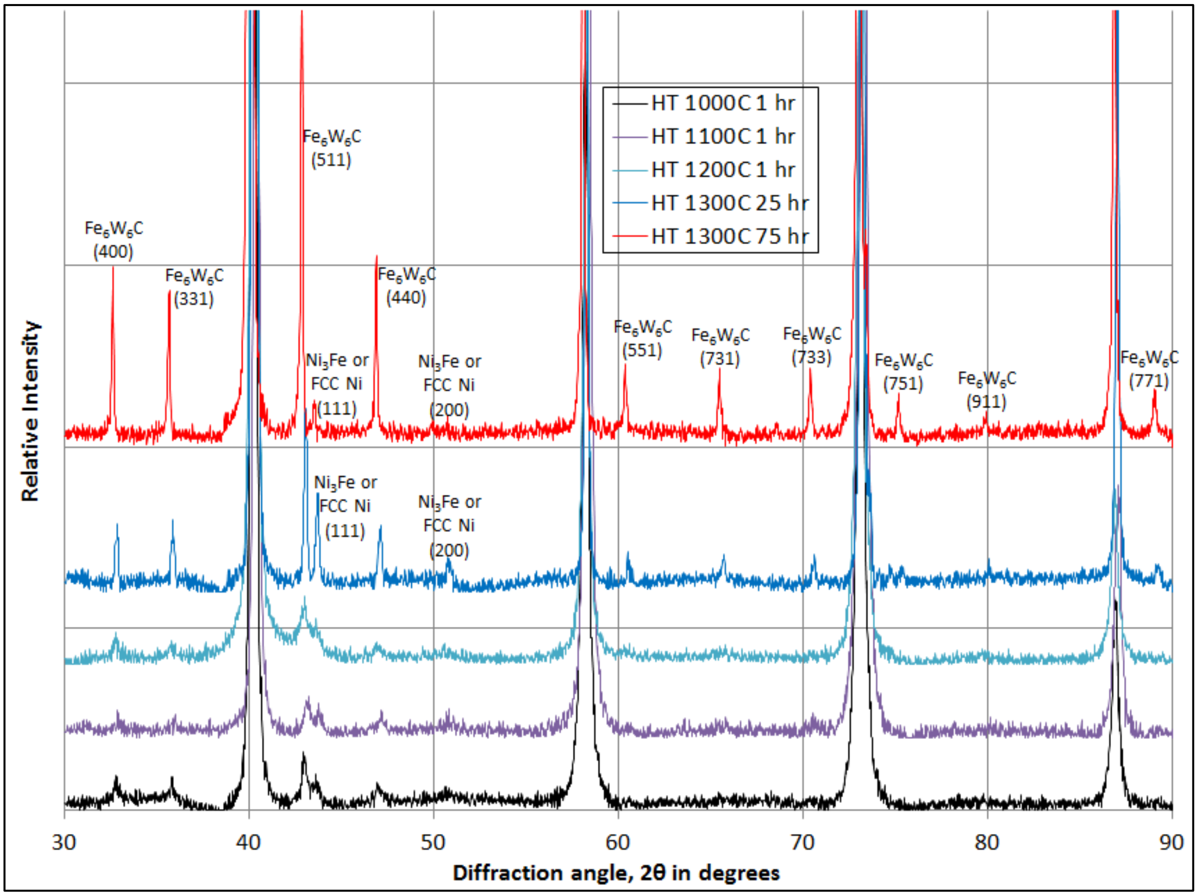

Figure 37 XRD curves for 50 hour milled samples – sintering temp increases vertically as indicated in legend

The third phase peaks don't match perfectly with either potential phase as shown in Figure 38. Figure 38 shows the area from diffraction angles 42 to 52° in the 15 hour milled samples for all heating runs to demonstrate the observed peaks in relation to the literature values for the peak positions of each potential phase. Figures B1.3 and B1.4 in Appendix B show similar curves for the 25 and 50 hour milled samples for all five heating runs. The Ni_3Fe intermetallic phase literature peaks are slightly closer to the observed than the crystalline FCC Ni literature peaks, [58, 59] but FCC Ni could be more likely to be shifted to lower diffraction angles due to the dissolution of W into the lattice. Further discussion of the identity of this third phase is provided in Chapter 5.

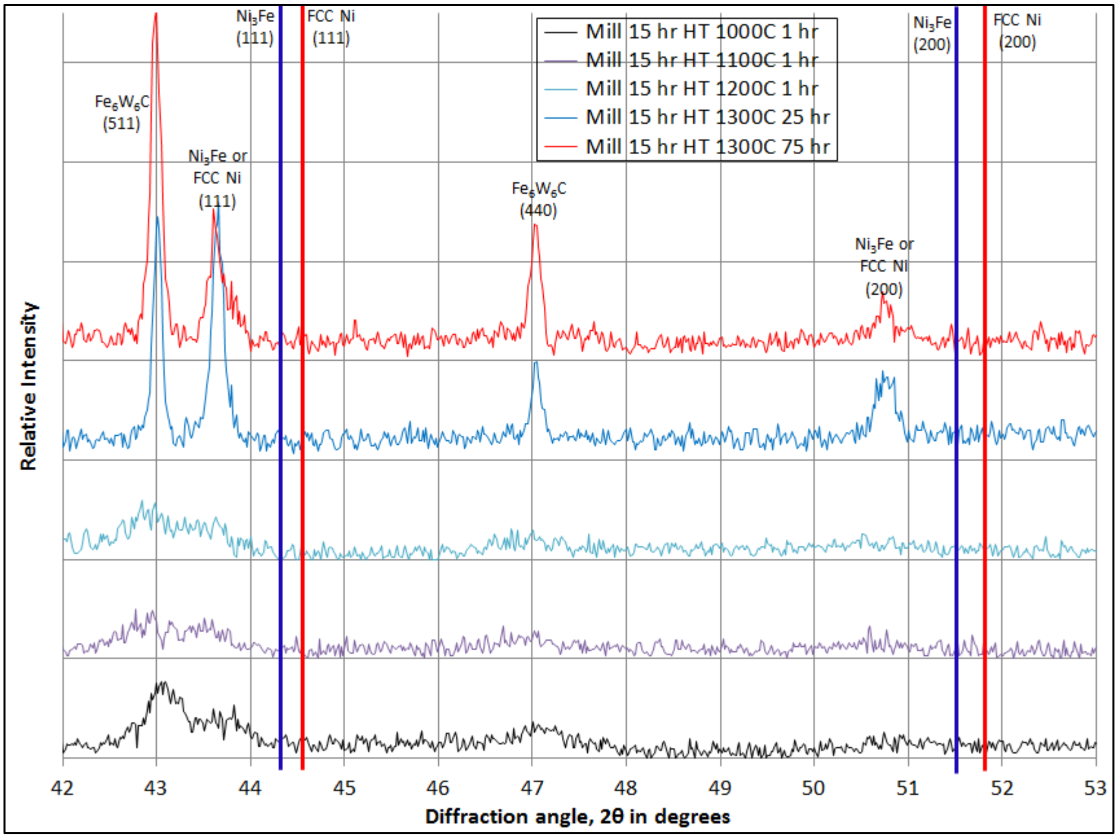

Figure 38 XRD curves for 15 hour milled samples with vertical lines drawn indicating expected peak positions for Ni$_3$Fe and FCC Ni – sintering temp increases vertically as indicated in legend

4.2.3 Scanning Electron Microscopy (SEM)

SEM was used to examine all fifteen compacted samples for a qualitative assessment of densification and microstructure, including phases present and grain size. Low magnification images from the backscattered electron detector (BSED) allowed for imaging to observe the degree and nature of densification as a function of milling time and sintering parameters. Higher magnifications were used to observe the microstructure for grain size as well as different phases in conjunction with elemental mapping and composition at specific points using energy dispersive X-ray spectroscopy (EDS).

4.2.3.1 Densification

Low magnification SEM images with the BSED allowed for good qualitative comparison of the degree and nature of densification. Figure 39 shows a composite of nine SEM micrographs with sintering temperature increasing from 1000 to 1200°C from top to bottom and milling time increasing from 15 to 50 hours from left to right. While the beam energy and size were held constant, the more artificial parameters of brightness and contrast of each original image were not tightly controlled. Therefore, each image was modified from the original micrograph by brightness and contrast to highlight the difference between more porous and dense regions to give a sense for the degree and nature of densification.

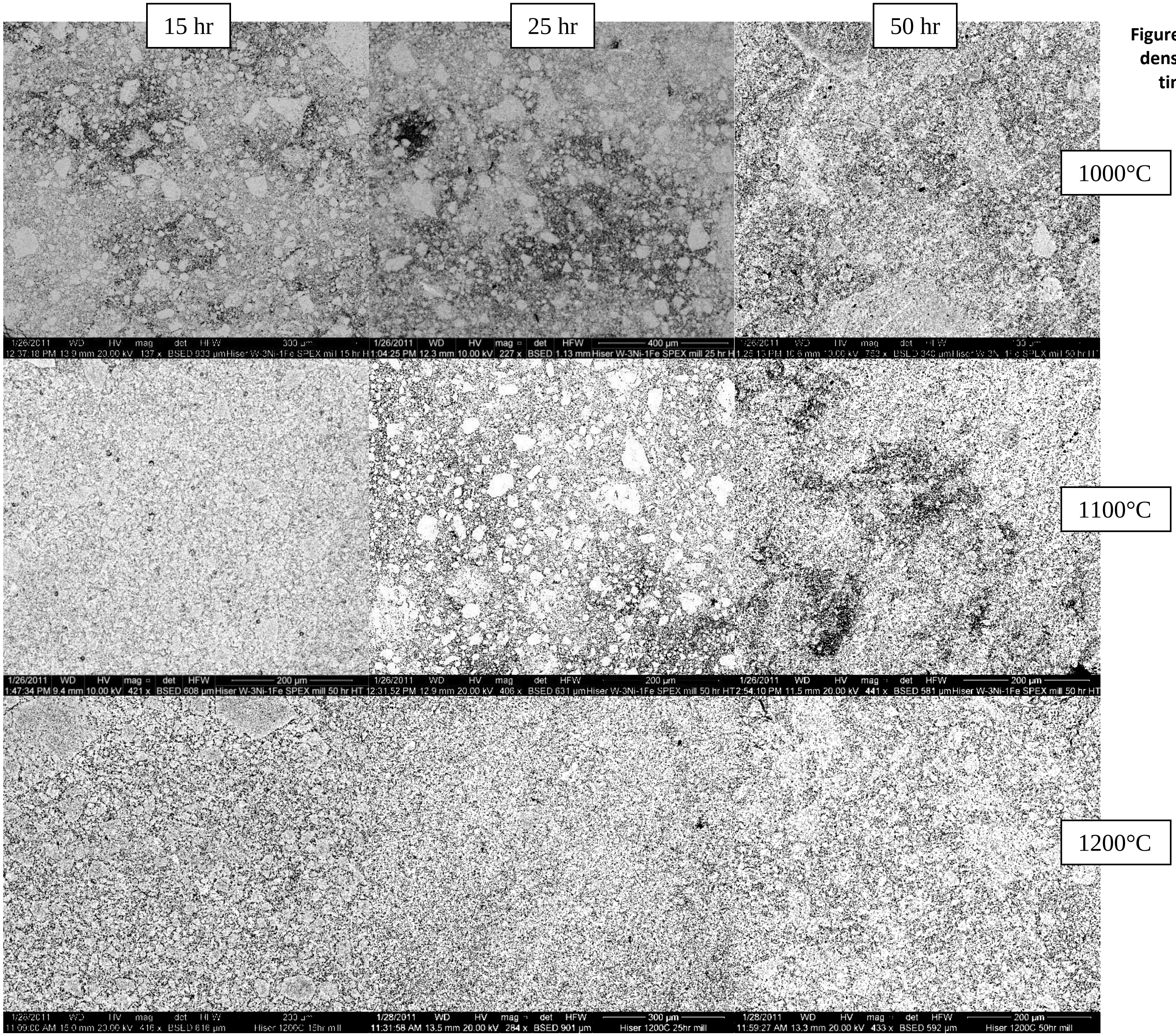

Figure 39 SEM micrographs illustrating densification as a function of milling time and sintering temperature

While the images have been modified to highlight porosity in all cases, it appears clear that porosity decreases with increasing milling time and sintering temperature. As with Archimedes' density, sintering temperature appears to be the strongest driver of densification with all three 1200°C sintered samples appearing fairly homogeneous and dense, while lower temperatures show more significant porosity and heterogeneity with fairly densified regions surrounded by areas of porosity. A slighter trend also appears with increasing milling time, where densification appears more homogeneous with increasing milling time. At longer milling times (particularly 50 hours), there is less contrast between densified regions and surrounding more porous regions. Figures B2.1 and B2.2 show the densification of two samples sintered to 1300°C to demonstrate the almost fully dense, homogeneous structure that is achieved with sufficient sintering.

4.2.3.2 Microstructure and Grain Size

At higher magnifications, SEM micrographs show that a heterogeneous structure with a bimodal grain size distribution develops for all samples sintered at 1200°C. Figures 40, 41, and 42 show samples milled for 25 hours and sintered at 1000, 1100 and 1200°C, respectively. These figures show typical microstructures for these samples. There is greater porosity in the large-grained regions, while small (generally submicron) grains appear in almost fully dense regions on the order of tens to about one hundred microns in size. The primary variation across the samples is the large decreases in degree of porosity with increasing sintering temperature, whereas the grain size increases significantly. There also appears to be a weaker trend of decreasing heterogeneity and porosity at longer milling times. Additional images at the milling times of 15 and 50 hours can found in Figures B2.3-B2.7 in Appendix B.

Figure 43 shows the 50 hour milled 1200°C sintered sample and appears to show reduced heterogeneity, which is probably a precursor to the transition at higher sintering temperatures and times where porosity becomes negligible and grain size becomes more homogeneous. Figure 44 shows the 15 hour milled 1300°C 25 hour sintered sample, which continues this trend with larger grains and less porosity, but still some evidence of smaller-grained areas. Finally, by 1300°C 75 hours sintering, the grain size appears homogeneous as seen in Figure 45.

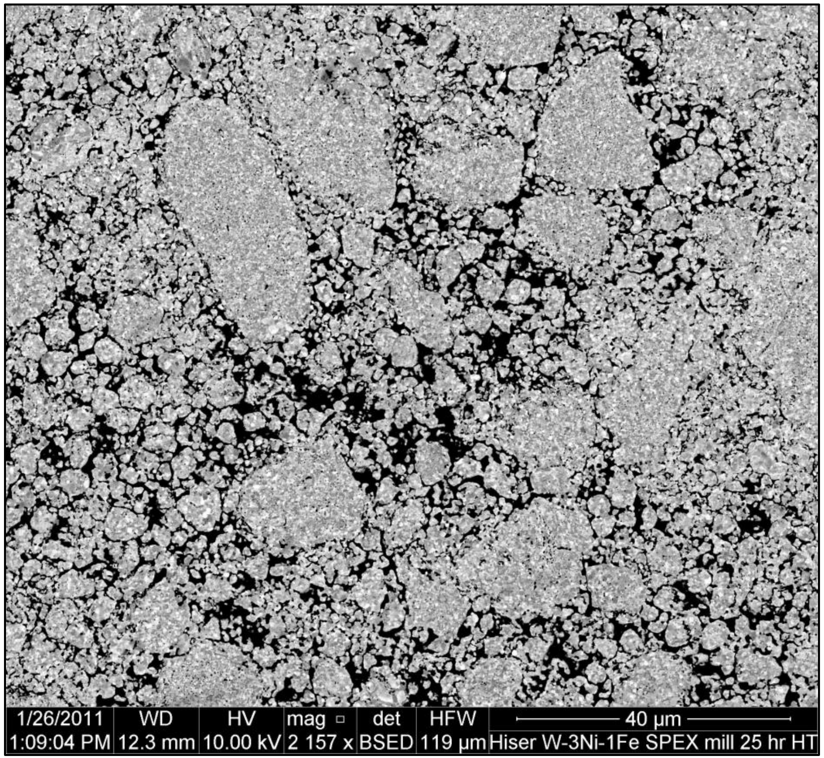

Figure 40 SEM micrograph of 25 hour milled 1000°C sintered sample

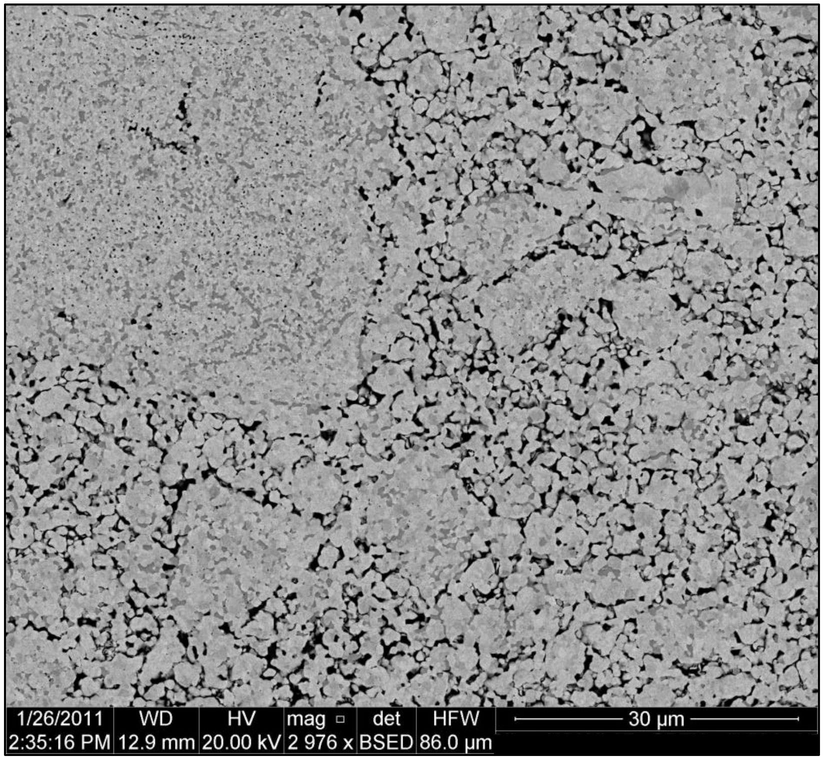

Figure 41 SEM micrograph of 25 hour milled 1100°C sintered sample

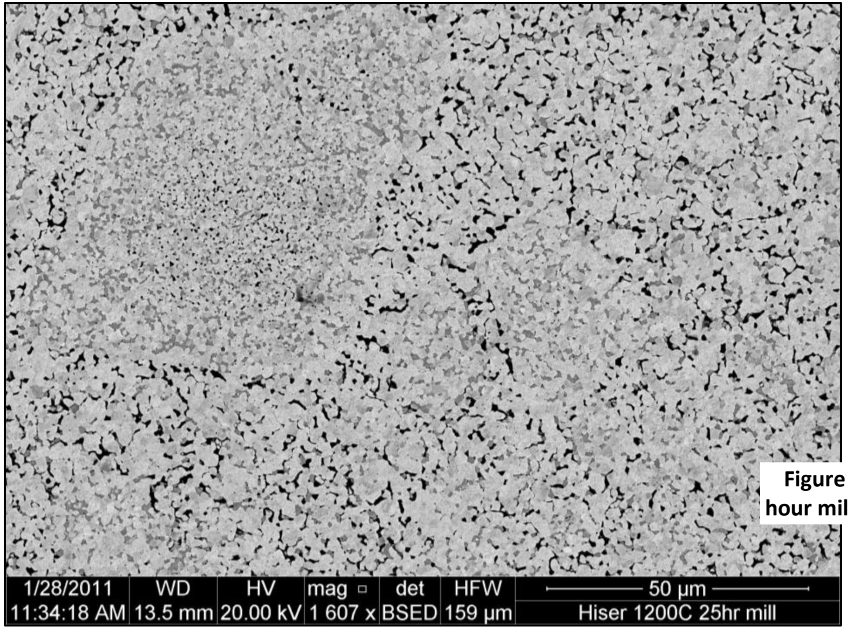

Figure 42 SEM micrograph of 25 hour milled 1200°C sintered sample

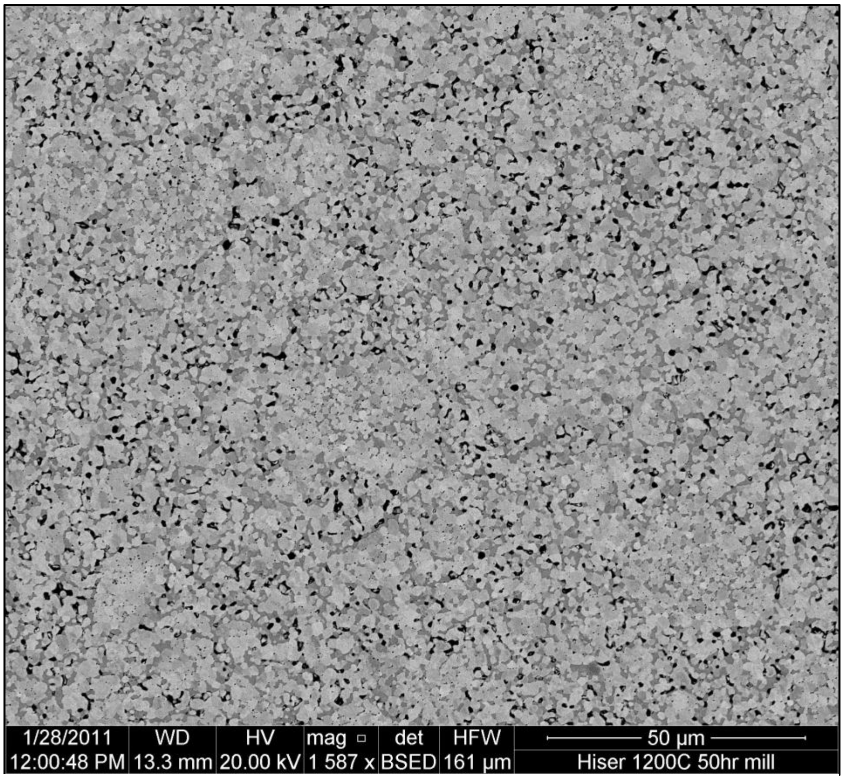

Figure 43 SEM micrograph of 50 hour milled 1200°C sintered W-3Ni-1Fe

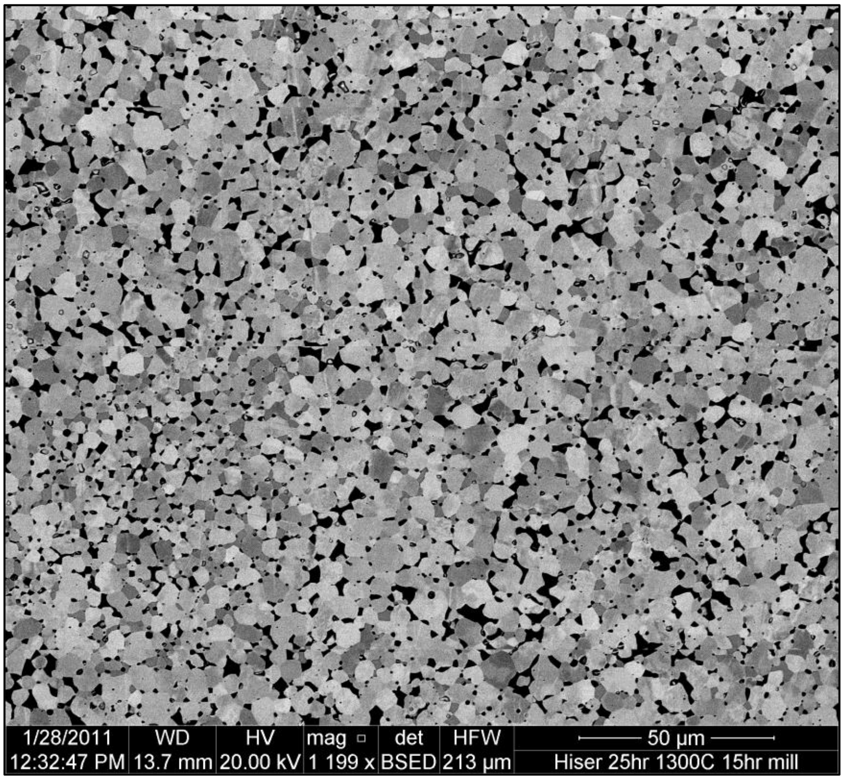

Figure 44 SEM micrograph of 15 hour milled 1300°C 25 hour sintered sample

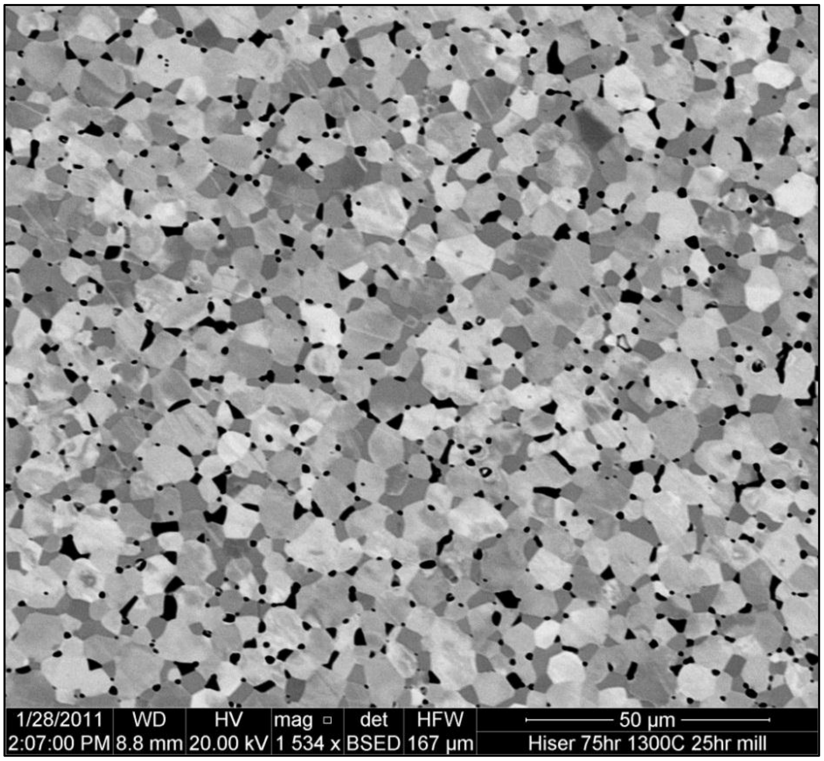

Figure 45 SEM micrograph of 25 hour milled 1300°C 75 hour sintered sample

The preceding Figures 40-45 provide a qualitative assessment of the grain size distribution, which was supplemented by a quantitative assessment of grain size as a function of milling time and sintering temperature using higher magnification SEM micrographs. Figure 46 demonstrates how higher-magnification images were taken of both the small and large grained regions for each sample to estimate grain size in each area for each sample. These images were used to estimate grain sizes in large and small (if present) grain size regions for each sample, which are presented in Tables 4 and 5 below respectively.

Table 4: Large Grain Size (in µm) as a Function of Milling Time and Sintering Parameters

Milling Time / Sintering Temperature & Time	1000˚C for 1 hour	1100˚C for 1 hour	1200˚C for 1 hour	1300˚C for 25 hours	1300˚C for 75 hours
15 hours	0.4	1	2.5	4 – 10	6 – 12
25 hours	0.5	1.5	3	3 – 8	6 – 12
50 hours	1	2	2.5	4 - 10	5 – 12

Table 5: Small Grain Size (in µm) as a Function of Milling Time and Sintering Parameters

Milling Time / Sintering Temperature & Time	1000˚C for 1 hour	1100˚C for 1 hour	1200˚C for 1 hour	1300˚C for 25 hours	1300˚C for 75 hours
15 hours	0.1	0.5	1	N/A	N/A
25 hours	0.2	0.4	1.5	N/A	N/A
50 hours	0.3	0.6	1	N/A	N/A

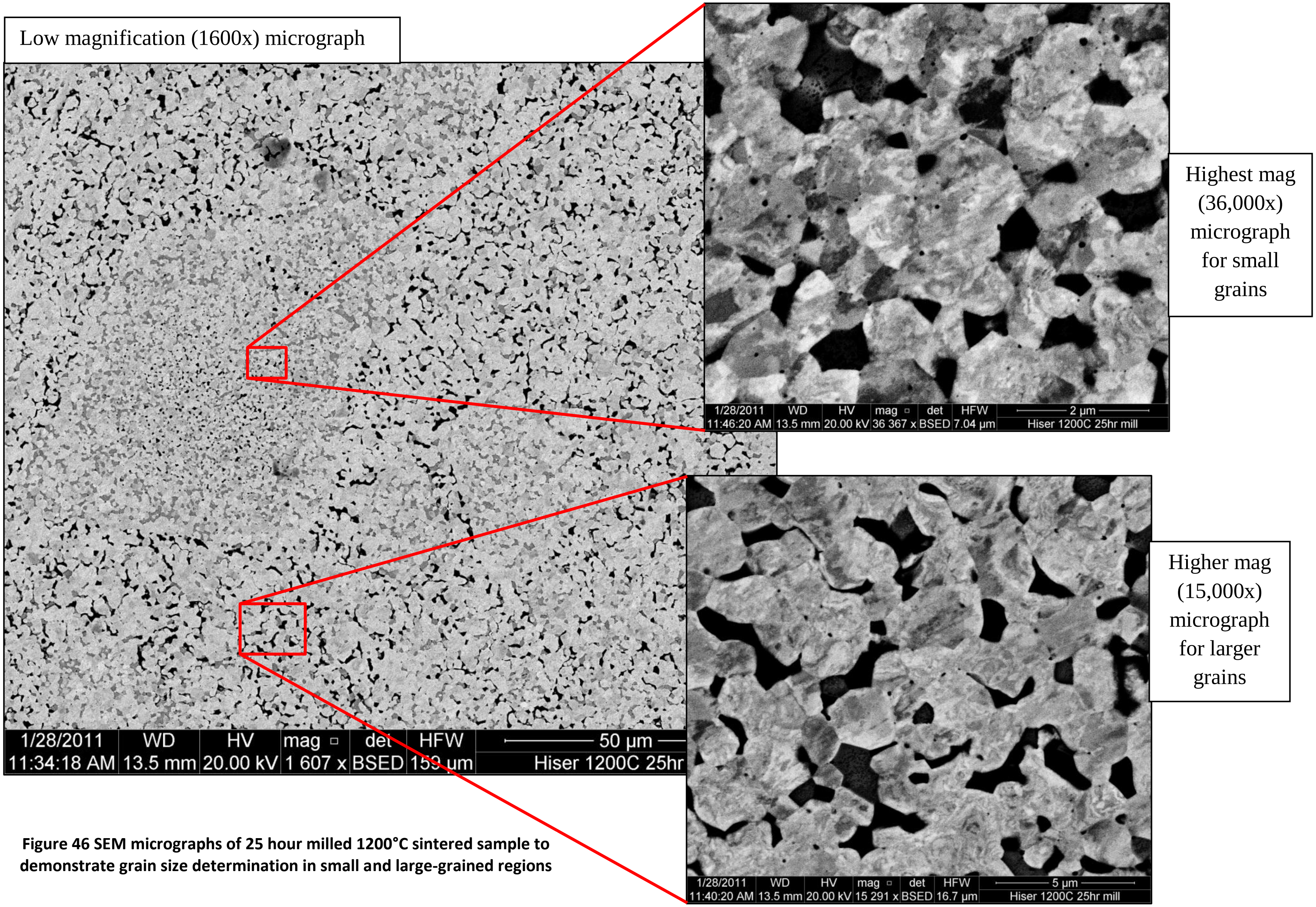

Figure 46 SEM micrographs of 25 hour milled 1200°C sintered sample to demonstrate grain size determination in small and large-grained regions

Tables 4 and 5 summarize the approximate grain sizes in large and small-grained regions for all samples. These visual estimates show the large grains to be on the order of 2 to 4 times larger than the small grains in samples where the bimodal distribution appears. Grain sizes increase most strongly with sintering temperature, but also have a weaker positive correlation with increasing milling time. By 1200°C sintering temperature, almost all of the grains (both small and large) are at least 1μm in size, but at 1000 and 1100°C sintering, small grains are on the order of 600 nm or less, considered to be nearly ultra-fine grained (UFG). There is also dramatic grain growth observed in samples sintered at 1300°C, with grain sizes above 10 μm.

To better understand the differences between the large and small-grained regions, object-based EDS analysis was used to observe compositional differences in the two regions as shown in Figure 47 for the 1100°C HT 25 hr milled sample. For this analysis, objects were drawn on SEM images to select small or large grained regions from which to scan and measure elementally by EDS. As can be seen below, Box 24 is in a small-grained region, while Box 26 is in a large grained region. The small-grained region appears to contain slightly less Ni/Fe and more W compared to the large-grained region adjacent to it. This observation is consistent for a variety of areas on three different samples that were observed. Table 6 shows the ratios relative to Ni of the average compositions of large and small grained regions from three different samples based on at least four samples of each region on each sample. There appears to be a substantially larger ratio of W:Ni in the small grained regions compared to the large grained regions consistently across many regions of many samples.

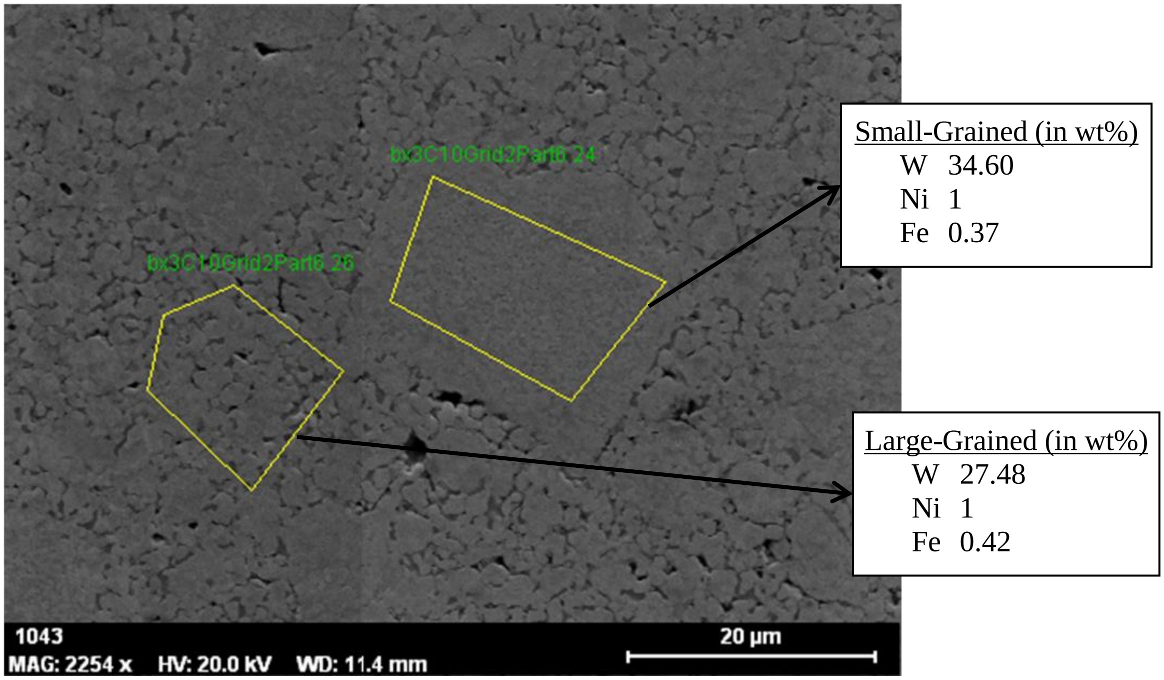

Figure 47 SEM micrograph of 25 hour milled 1100°C sintered sample to show object-based EDS analysis in small and large-grained regions

Table 6: Small vs. Large Grained Region Object-Based EDS Composition Readings

Ratio relative to Ni in wt%	Sample	1000°C 1 hr HT 50 hr mill	1100°C 1 hr HT 25 hr mill	1200°C 1 hr HT 15 hr mill
Small-Grained Regions	Avg. W:Ni	35.58	35.67	31.22
	Avg. Ni:Ni	1	1	1
	Avg. Fe:Ni	0.46	0.37	0.35
Large-Grained Regions	Avg. W:Ni	28.62	28.28	26.71
	Avg. Ni:Ni	1	1	1
	Avg. Fe:Ni	0.41	0.39	0.38
Difference (Small – Large)	Avg. W:Ni	6.96	7.39	4.51
	Avg. Ni:Ni	0	0	0
	Avg. Fe:Ni	0.05	-0.02	-0.03

4.2.3.3 Phase Identification by EDS

SEM also was used to explore phases present with the use of energy dispersive X-ray spectroscopy (EDS) for compositional mapping to identify W-rich and W-depleted regions as well as for point estimates of semi-quantitative composition. In this effort, compositional differences (i.e., different phases) could be identified indirectly by observing the brightness of the area in the BSE image. W-rich areas were brightest because W has a much greater atomic weight than Ni or Fe, causing it to backscatter more electrons. Regions that are more diluted in W appear darker due to the reduction in BSE. Therefore, from BSE images areas of differing W composition could be identified, confirmed more directly by compositional mapping to show concentration of W, Ni, and Fe, and then most fully characterized by point-based EDS to estimate W, Ni, and Fe composition at specific points.

SEM images appeared to be consistent with XRD results in showing the presence of two precipitation phases in addition to the W BCC matrix. These phases appear consistently in all samples observed using both SEM and XRD, although their volume fraction varies significantly. Figure 48 shows a typical BSE image with compositional maps at a lower sintering temperature of 1200°C showing the presence of three different phases. However, the most useful information was gathered from the 1300°C sintered samples, which provided a coarser microstructure for easier identification and analysis of phases. Figure 49 shows results from a 1300°C sintered sample to demonstrate the apparent similarity in phases, but the greater ease of analysis with coarser microstructure. Figure 50 shows another 1300°C sintered sample with a compositional map with W, Ni and Fe counts overlaid on one another. Based on the similarity in compositional maps (seen in Figures 48-50) and the XRD results showing similar precipitation peaks, it is reasonable to assume that the phases present in the 1300°C sintered samples are also present (just more difficult to characterize) in the lower temperature sintered samples. Notice the difference in size of the features in Figure 48 compared to Figures 49 and 50; the features in Figure 48 are 1 µm or less, while in Figures 49 and 50 all features are several microns in size.

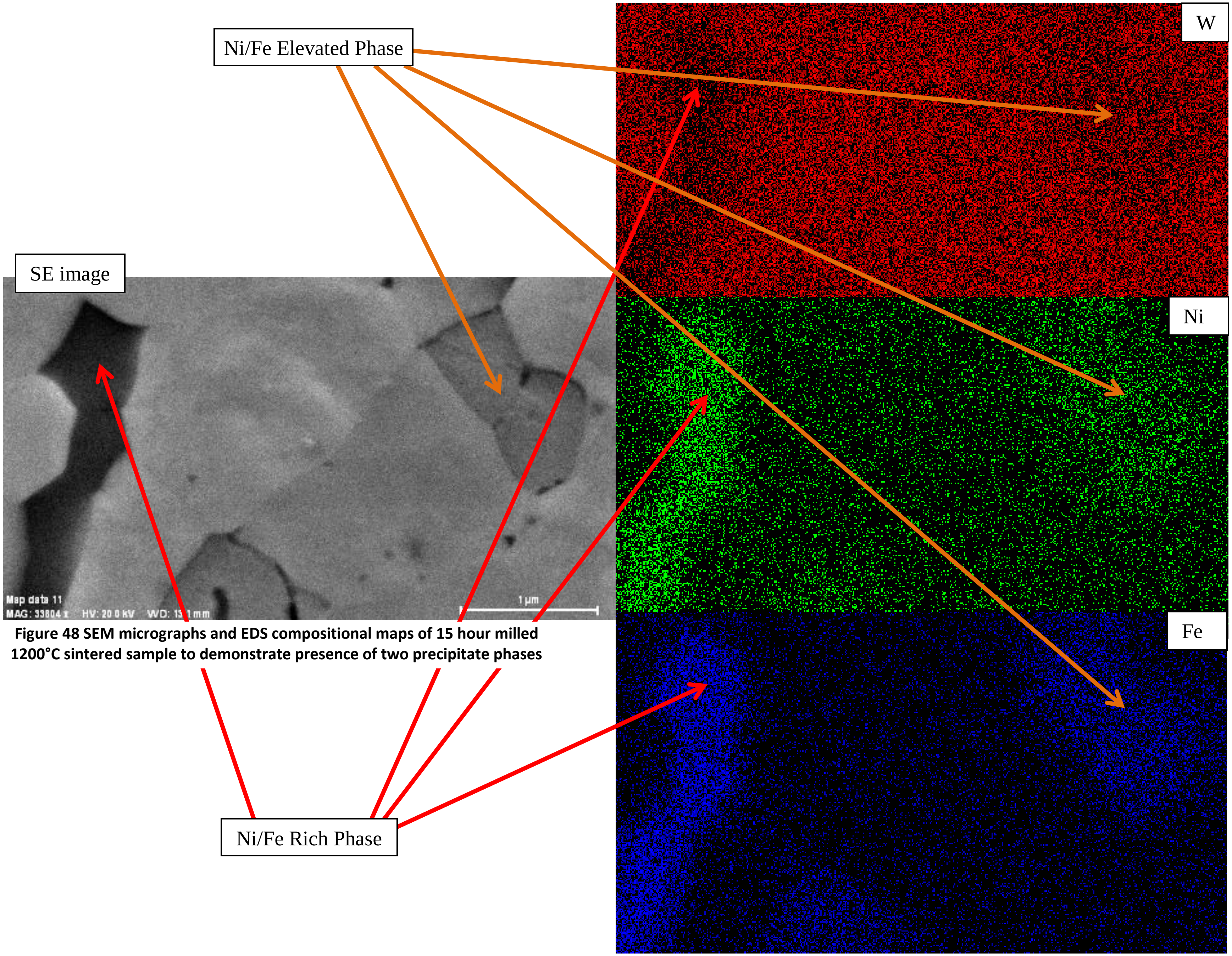

Figure 48 SEM micrographs and EDS compositional maps of 15 hour milled 1200°C sintered sample to demonstrate presence of two precipitate phases

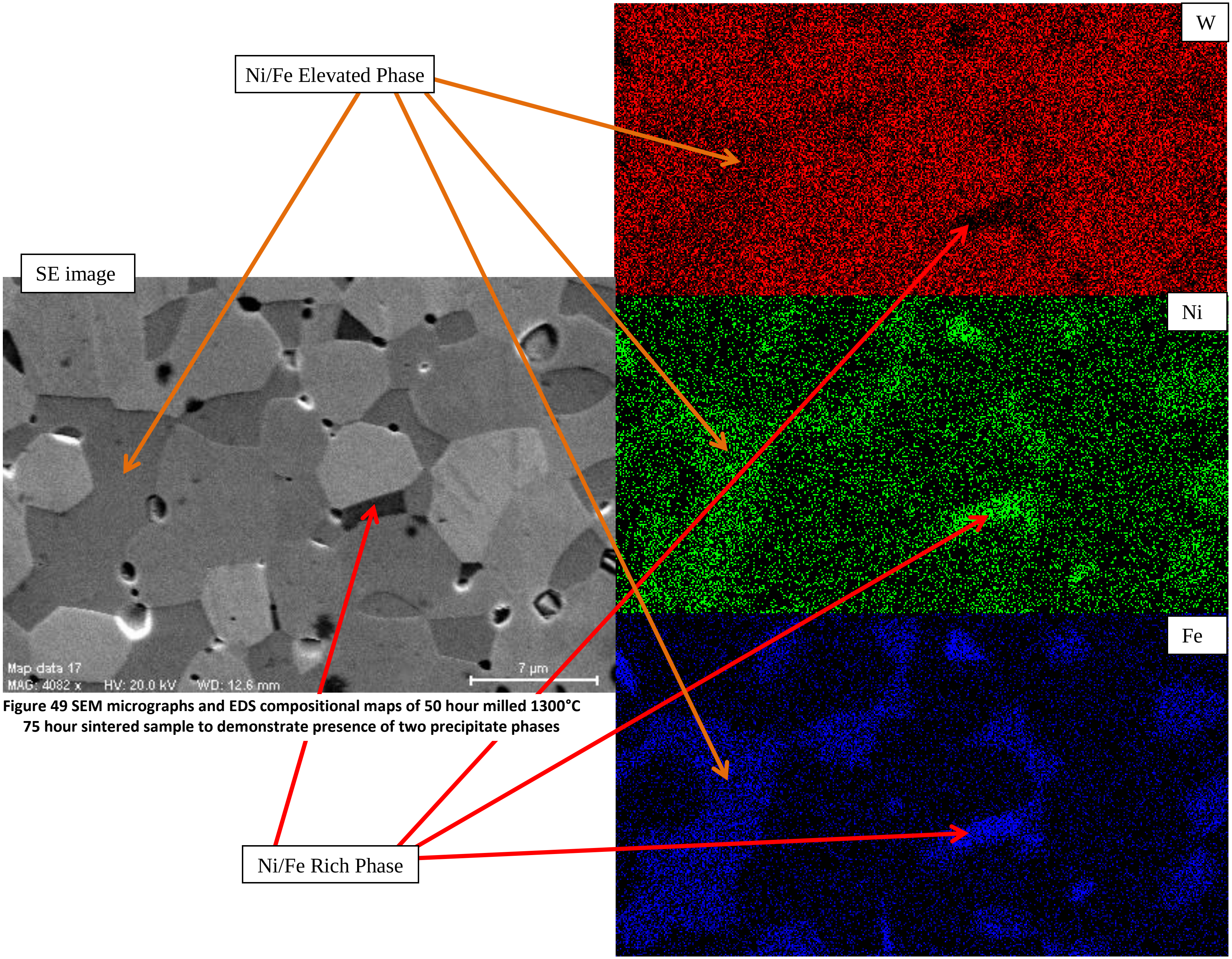

Figure 49 SEM micrographs and EDS compositional maps of 50 hour milled 1300°C 75 hour sintered sample to demonstrate presence of two precipitate phases

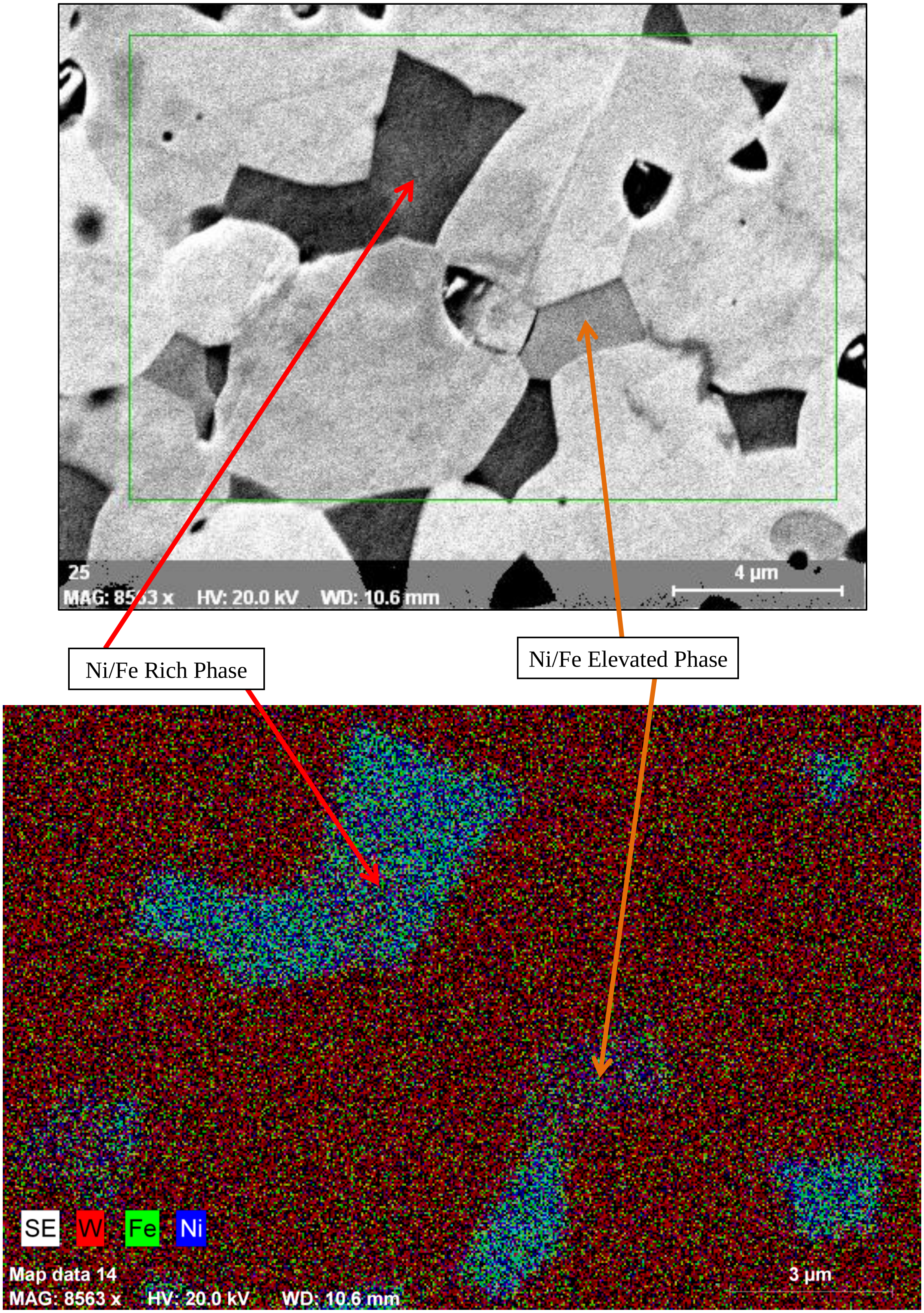

Figure 50 SEM micrograph and overlaid EDS compositional map of 15 hour milled 1300°C 25 hour sintered sample to demonstrate presence of two precipitate phases

Images such as those shown in Figures 48-50 were analyzed by point-based EDS to semi-quantitatively estimate the W, Ni, and Fe composition. The three phases were each targeted to try to gain confidence in the W, Ni, and Fe composition of each phase. Figure 51 shows an example of how point-based EDS was used to estimate composition relative to Ni of the different phases. The consistency of the semi-quantitative compositions observed for each phase was very good. The three observed phases will be referred to as W matrix, Ni/Fe elevated, and Ni/Fe rich for now. The W matrix phase had a ratio of greater than 100 for W:Ni in wt%. The Ni/Fe elevated phase was observed to have a ratio of about 5 for W:Ni and about 0.35 for Fe:Ni, indicating much more Ni/Fe relative to W. The Ni/Fe rich phase exhibited more variability in observed composition, but was generally around a W:Ni ratio of 0.5 and a Fe:Ni ratio of 0.34. It is interesting to note that each of these precipitate phases shows Ni and Fe at about a 3:1 ratio, similar to their initial bulk composition. Table 7 below summarizes the compositional results relative to Ni for the W matrix and Ni/Fe elevated phases, while Table 8 shows all the data, identified by the sample from which the observation was made, for the less clear case of the Ni/Fe rich phase. Tables B2.1 and B2.2 in Appendix B show the full data for the W matrix and Ni/Fe elevated phases respectively, which is summarized in Table 7 below. Each of Tables 8, B2.1, and B2.2 has a thicker line partway down to delineate samples sintered below 1300°C.

Table 7: W Matrix and Ni/Fe Elevated Phase Point-Based EDS (in wt%) Relative to Ni Ratio-Based Composition Readings Summary

Phase	W Matrix	Ni/Fe Elevated
Total # of Measurements	19	15
# of Measurements on Samples Sintered below 1300°C	5	7
Avg. W:Ni	114.48	4.96
Avg. Ni:Ni	1	1
Avg. Fe:Ni	0.8	0.35

Table 8: Ni/Fe Rich Phase Point-Based EDS Composition Readings

Sample (in wt% relative to Ni)	W:Ni	Ni:Ni	Fe:Ni
15 hr mill 1200°C for 1 hr HT	2.61	1	0.40
15 hr mill 1300°C for 25 hr HT	0.89	1	0.34
25 hr mill 1300°C for 25 hr	**0.42**	**1**	**0.38**
50 hr mill 1300°C for 25 hr	**0.64**	**1**	**0.36**
50 hr mill 1300°C for 25 hr HT	1.34	1	0.36
50 hr mill 1300°C for 25 hr HT	1.86	1	0.61
15 hr mill 1300°C for 75 hr	**0.47**	**1**	**0.33**
25 hr mill 1300°C for 75 hr	**0.49**	**1**	**0.31**
50 hr mill 1300°C for 75 hr	**0.54**	**1**	**0.34**
50 hr mill 1300°C for 75 hr	**0.54**	**1**	**0.34**
Bold Average	**0.51**	**1**	**0.34**
All Average	0.82	1	0.36

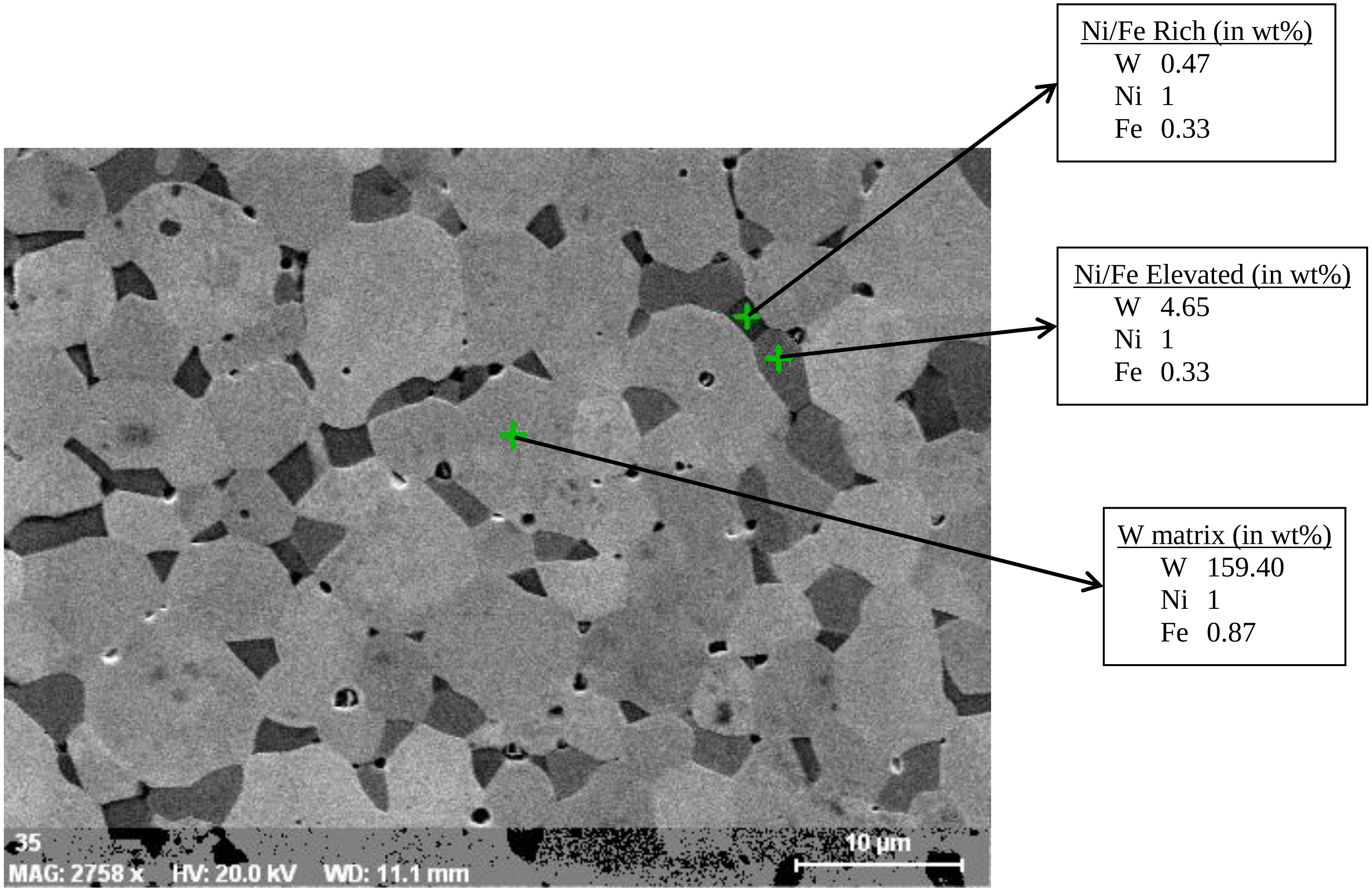

Ni/Fe Rich (in wt%)
W 0.47
Ni 1
Fe 0.33

Ni/Fe Elevated (in wt%)
W 4.65
Ni 1
Fe 0.33

W matrix (in wt%)
W 159.40
Ni 1
Fe 0.87

Figure 51 SEM micrograph and point-based EDS compositions of 15 hour milled 1300°C 75 hour sintered sample to demonstrate presence of two precipitate phases

4.2.4 Hardness Testing

Both Vickers macro and microhardness testing were performed on all samples as described in Chapter 3. The two methods were employed to observe the effect of the scale (macro vs. micro) on the resulting hardness value. Figure 52 shows an ordered plotting of macro vs. micro hardness values for the fifteen samples tested with a 1:1 correlation line shown for reference and demonstrates very good correlation between the two tests. Microhardness values are equal or slightly higher in all cases, but macrohardness reflects microhardness fairly well across milling time and sintering temperature. The hardness plots shown in this chapter are all of microhardness, which is expected to be more representative of the microstructure by showing less effect of porosity. The corresponding macrohardness plots can be found in Appendix B.

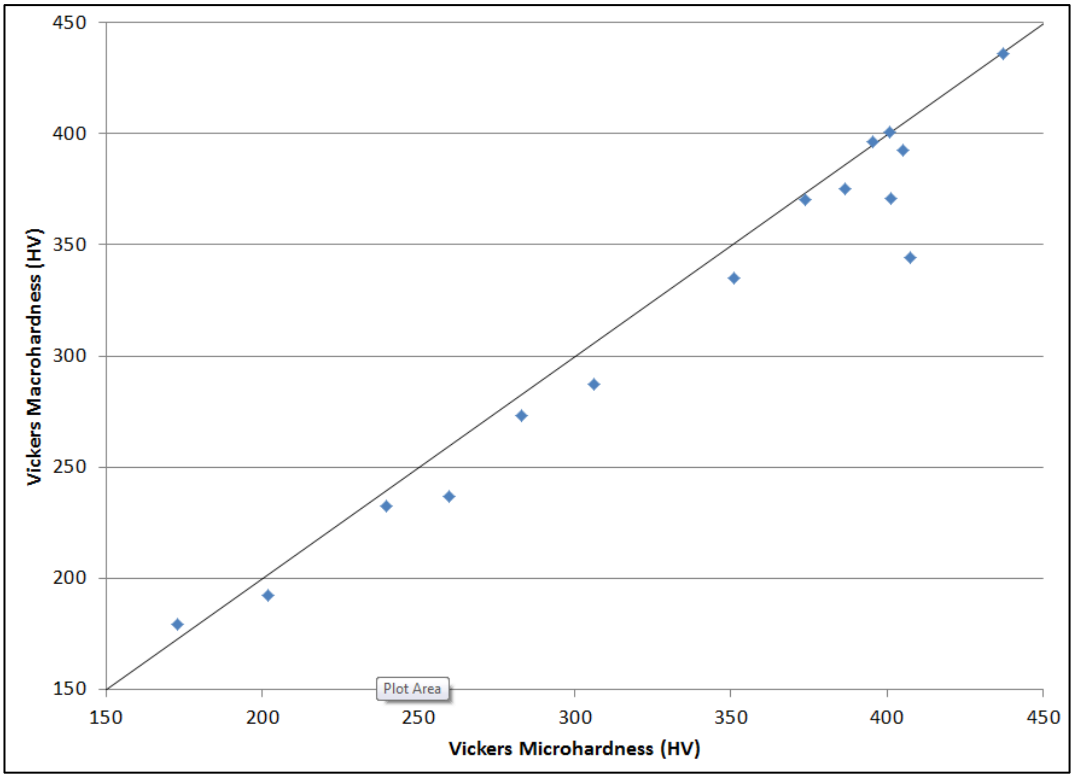

Figure 52 Macrohardness values as a function of microhardness values for all samples

Figure 53 shows a plot of Vickers microhardness as a function of sintering temperature for all three milling times, while Figure B3.1 in Appendix B shows the corresponding plot for macrohardness. In both figures, the points located slightly to the left of 1300°C represent those held for 25 hours, while those slightly to the right represent a 50-hour hold at 1300°C. Figure B3.2 in Appendix B shows the same data as a function of milling time rather than sintering temperature, with Figure B3.3 presenting the corresponding macrohardness data. All four hardness plots show 95% confidence intervals on all points based on the t-statistic from the number of tests and the standard deviation as described in Chapter 3.

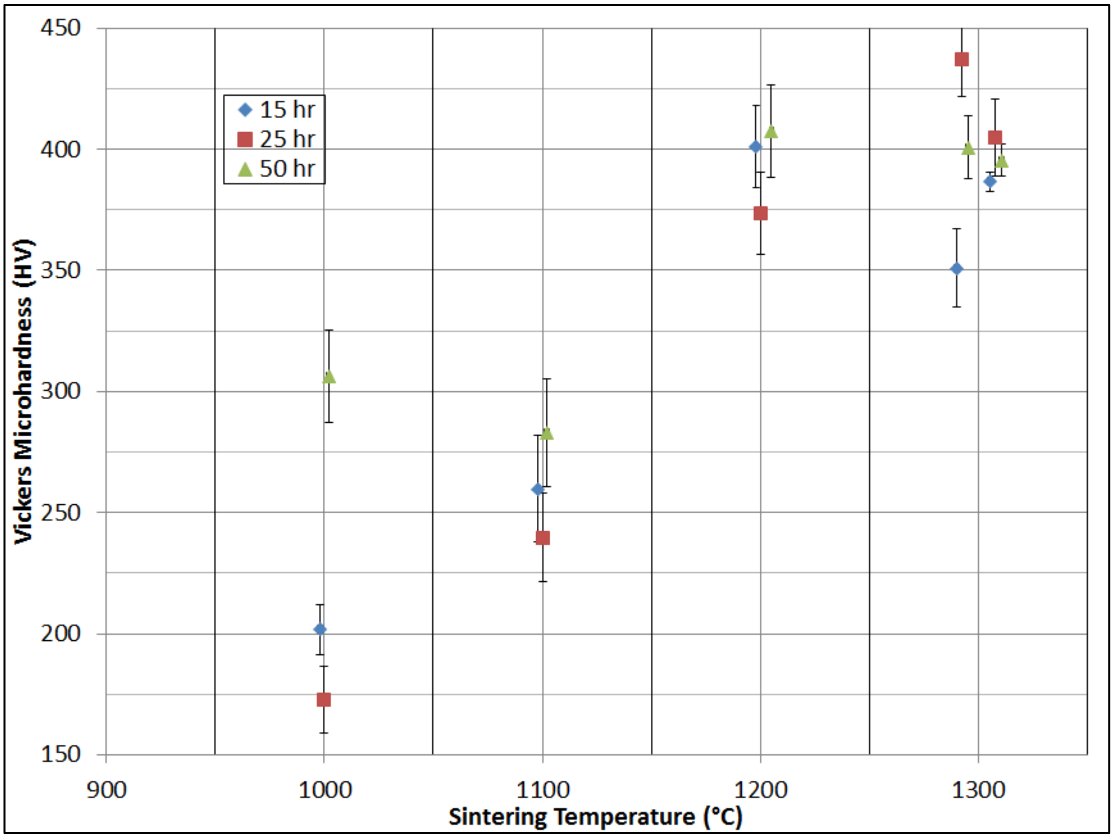

Figure 53 Microhardness as a function of sintering temperature over all three milling times

All hardness plots show a primary effect of sintering temperature, along with a weaker trend associated with increasing milling time. Figure 53 shows a large increase in microhardness from 1100 to 1200°C for all milling times from 250-275 HV to 375 – 400 HV. The long hold time 1300°C samples show no significant increase in hardness over their 1200°C counterparts. These figures also show a trend with increasing milling time, particularly at lower sintering temperatures, where the 50 hour milling time has significantly higher hardness than the 15 and 25 hour milling time samples.

Chapter 5

5. Discussion

Chapter 4 presented all of the data gathered by the experimental methods described in Chapter 3. This chapter provides deeper discussion and analysis of the results to bring together a cohesive description of the powder processing of W-3Ni-1Fe.

5.1 Powder Particle Size Distribution

Particle size analysis and SEM of powder particles are consistent with each other in showing a bimodal particle size distribution developing from starting powders of a modal size distribution as can be seen in Figures 14-20 in Chapter 4. Starting powder particles averaged around 40 – 50 µm in size, with almost all particles between 20 and 70 µm in size. Milling developed a bimodal particle size distribution with about 75% of the particles between 1 and 15 µm in size and about 15-20% of the particles between 30 and 150 µm in size. The remaining few percent are either submicron (~2%) or between 15 and 30 µm (~5%). This description of particle size distribution is consistent between quantitative particle size analysis and the more qualitative SEM. The reason for the development of a bimodal particle size distribution in milling is not clear based on current characterization of the powders.

Milling time does not have a dramatic effect on particle size distribution, although there is a general trend of both peaks shifting towards smaller sizes. The smaller particle size peak shows a reduction in the number of particles in the 5-15 µm size range with an increase in particles below 5 µm in size with increasing milling time. The larger particle size peak also exhibits a reduction in the number of particles in the 100-150 m size range with more particles shifting to the 30 to 80µ m size range with increasing milling time. These trends with increasing milling time are slight, but consistent over several milling times and could help to explain trends in densification, grain size, and microstructure found in bulk samples with increasing milling time.

Point-based EDS comparing composition of small and large particles in Table 3 and Figure 22 also appears to show slightly greater Ni/Fe content in the small powder particles. This difference increases with increasing milling time and appears to carry through and could help explain the bimodal grain size distribution observed in sintered samples.

5.2 Powder X-ray Diffraction

5.2.1 Peak Shifting and Dissolution of Ni/Fe into W

Figure 24 in Chapter 4 show the change in W lattice parameter as a function of milling time inferred from peak position shifting shown in Figure 23. The results show the W lattice parameter decreasing steadily with increasing milling time up to 50 hours from a starting value of 3.162 Å to a minimum value of 3.138 Å after 50 hours of milling. This change is significant particularly when observing the XRD peak shifts in Figure 20, and is consistent over all four milling times. The 100 hour milling time shows a lattice parameter of 3.140 Å, only slightly larger than at 50 hours.

The decrease in lattice parameter can only reasonably be explained by the dissolution of Ni and Fe into the W lattice. Ni and Fe are nearly the same size (atomic radius of 0.124 nm for Fe and 0.125 nm for Ni) and significantly smaller than W (atomic radius of 0.137 nm) [52]. Therefore, when Ni and Fe atoms replace W atoms in the BCC lattice the average lattice parameter decreases. Both W and Fe have stable BCC structures (with known lattice parameters) at room temperature, while Ni is FCC at room temperature. Therefore, two very basic (but also unrealistic) assumptions were made: identical effects of Ni and Fe (based on their almost identical size) on W lattice parameter and a linear trend of lattice parameter with Ni/Fe composition. These assumptions as well as the entire methodology used are described in more detail in Chapter 3. These assumptions and Equations 2 and 3 from Chapter 3 were used to produce Figure 54 below, which plots Ni/Fe dissolution in W as a function of milling time.

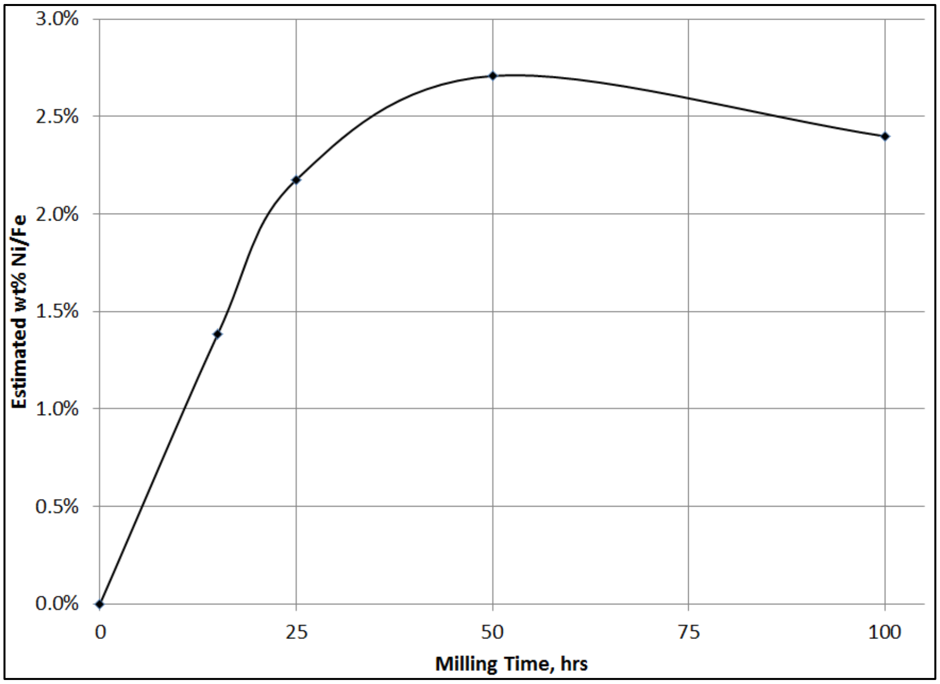

Figure 54 Estimated wt% Ni/Fe dissolved in W as a function of milling time

While the assumptions inherent to Figure 54 are certainly not 100% accurate, given the size similarity of Ni and Fe and the small amounts of Ni and Fe being dissolved, they can be expected to be reasonably effective. It is therefore interesting to note that the starting bulk composition was 4 wt% Ni/Fe and this simple model indicates that about 2.7 wt% Ni/Fe is dissolved into the W lattice after 50 hours of milling. Therefore, while the accuracy of this value is unknown, it is at least consistent with the initial composition. It is also interesting to note the decrease in estimated Ni/Fe content from 50 to 100 hours milling. This is probably due to reaching a limiting amount of Ni and Fe dissolved in the W lattice, so even with the metastable structures that can be formed by milling, only about 2.5 wt% Ni/Fe can be incorporated into the lattice.

5.2.2 Strain and Crystallite Size

XRD was also used to analyze peak broadening by the Williamson-Hall method to observe the degree of strain in the W lattice as well as the crystallite size, which is a rough estimate of grain size. Figures 25 and 26 in Chapter 4 summarize the trend of lattice strain and crystallite size, respectively, as a function of milling time. Lattice strain increases dramatically with increasing millingtime from 0.21% before milling to around 1.5% after milling. Strain continues to increase logarithmically with increasing milling time from about 1.42% after 15 hours to 1.56% after 100 hours. This is indicative of approaching a steady-state in milling where the amount of strain added with increasing milling time becomes negligible. Crystallite size decreases dramatically with increasing milling time from estimated over 10 μm to less than 50 nm after 15 hours milling. This decrease continues slowly but steadily, in almost linear fashion, down to about 23 nm after 100 hours milling. While decreasing crystallite (and therefore presumably grain) size is a desirable thing, high energy milling for 100 hours or more is not considered a very practical or economical approach. However, achieving crystallite sizes below 50 nm after much less milling is very promising and useful.

5.3 Densification

Data regarding densification during compaction and sintering is presented in Figures 27 – 36 in Chapter 4.

5.3.1 Green Density

Figure 27 shows the estimated green density measured by calipers as a function of milling time before and after a 300°C recovery HT and re-CIP. The results show a strong decrease in green density with increasing milling time as well as an increased effect of the recovery heat treatment (HT) with increasing milling time. These results can be explained fairly well by the effects of milling. As discussed in the prior section, lattice strain increases and crystallite (presumably grain) size decreases with increasing milling time. Strengthening effects can be seen in lattice strain based on work hardening and grain size based on the Hall-Petch effect as well as alloying with increasing dissolution of Ni/Fe into W. All of these effects serve to harden powder particles and make them more resistant to plastic deformation. Therefore, at longer milling times harder particles deform less under compaction and yield lower green densities. Likewise, due to the greater dislocation density and smaller crystallite size at longer milling times, a recovery HT is more likely to soften the particles by reducing dislocations (strain) and increasing grain size. This is seen in the greater effect of the recovery HT on green density at longer milling times.

A confounding consideration is the effect of particle size. Particle size decreases generally, though slightly, with increasing milling time as discussed above, but green density is not greatly affected by absolute particle size. The ratio of large to small particles can have an effect on green density, but this ratio changes only slightly if at all. Therefore, given the slight changes and the general weakness of the particle size effect, this effect is likely overwhelmed by the effect of particle hardness.

5.3.2 Sintered Density

Figure 28 shows densities for samples at the three milling times and two sintering times sintered at 1300°C with no significant trends across milling or sintering time. It appears that the 50 hour milled 1300°C 75 hour sintered sample is an outlier. Based on the lack of increase in density with sintering time, it seems reasonable to conclude that the maximum density that can be achieved by pressureless sintering under argon atmosphere is around 96 – 99% of the theoretical density and is reach by sintering at 1300°C for 25 hours regardless of milling time.

At lower sintering temperatures as shown in Figures 29, 30, and 39, sintered density increases strongly with sintering temperature, but also somewhat with increasing milling time. No explanation is needed for the increase in density with sintering temperature, but the slight increase in density with increasing milling time is more interesting. As discussed previously, particle size decreases with increasing milling time, meaning smaller particle size could provide more surface area as a driving force for densification. Similarly, decreasing crystallite size with increasing milling time provides greater grain boundary surface area, which aids diffusion and can increase driving force for densification. Another explanation consistent with this trend is the increased dissolution of Ni/Fe into the W lattice as inferred from XRD peak shifts and shown in Figure 54. Greater amounts of Ni dissolved in the W lattice could improve sintering by activating W diffusion both at the grain boundaries and volumetrically. One factor counter to the trend of increasing sintered density with increasing milling time is the green density, which decreases strongly with increasing milling time. It is likely that the three other factors (smaller particle size, smaller crystallite size, and greater dissolution of Ni/Fe in W) combined to overcome the reduced green density at the start of sintering.

Analysis of empirical diffusion activation energy during sintering and sintering exponent also helps to explain the trends discussed above. Apparent activation energy decreases strongly with increasing milling time from 70 kJ/mol to about 25 kJ/mol. This is likely due to the greater incorporation of Ni into the W lattice, which increases the rate of sintering by making diffusion easier. Therefore, as milling time increases and activation energy decreases greater densification is to be expected for a given temperature because the activation energy has been lowered, allowing diffusion to occur more freely. Sintering exponent, m, also reflects this reduction in activation energy, showing an increase in sintering rate with increasing milling time.

5.4 Microstructure and Grain Size

Figures 40 – 46 and Tables 5 and 6 describe the evolution of microstructure and grain size as a function of milling time and sintering parameters. A heterogeneous microstructure develops at lower sintering temperatures with more dense areas featuring small grains and more porous areas with grains two to four times larger in size than the small-grained regions. As sintering temperature increases grains grow and the microstructure becomes more homogeneous with less variation in grain size and porosity by region of the sample. Similar, but weaker trends were observed with increasing milling time. At longer milling times grains were slightly larger and microstructure somewhat more homogeneous. This trend of increased homogeneity can be clearly seen between Figures 42 and 43. Figure 42 shows that the sample milled for 25 hours and sintered at 1200°C is noticeably more heterogeneous than Figure 43, which shows the sample milled for 50 hours and sintered at 1200°C.

The heterogeneity observed most prominently at lower sintering temperatures appears to correlate with particle size. Regions of high density and small grain size are of similar size and shape to the larger pre-sintering powder particles observed under SEM. Therefore, it seems most probable that these large particles are the regions of high density and small grain size surrounded by smaller particles that are in more porous regions and more free to experience grain growth. However, this explanation is not consistent with sintering theory (discussed in Chapter 2), where grain growth rate increases as sintering progresses and porosity is eliminated. By sintering theory, grain growth should proceed faster in these almost fully dense areas where there is less porosity and slower in areas with more porosity.

This apparent contradiction could be explained by the Ni-activated sintering of W. Past research has shown Ni to activate W grain boundary diffusion by reducing the activation energy [37, 42-45]. It is possible that in large particles it is more difficult for Ni to be present at and activate the grain boundaries for diffusion and grain growth than in the smaller particles simply due to the surface area of the particles. Some evidence for this theory was found by object-based EDS, which showed substantial differences in composition between small-grained regions and adjacent large-grained regions. Results shown in Table 6 show more Ni/Fe relative to W in the large-grained regions compared to the small-grained regions.

The larger grains outside the larger particles could also be due to greater impingement of grain growth processes in the large particles compared to the small particle regions, which have a larger driving force for surface area reduction leading to greater diffusion and grain growth. One useful way to distinguish the importance of each effect (Ni activation vs. grain growth impingement) would be to mill, compact, and sinter pure W without any Ni or Fe for activation to observe the microstructure and grain size as a function of milling time. This could also provide insights into the development of the bimodal particle size distribution and any potential role Ni may play.

The trend of increasing grain size and homogeneity with increasing milling time could be explained by the reduction in particle size with increasing milling time. With smaller particles, there is greater driving force for surface area reduction leading to greater diffusion and grain growth, which explains the larger grain size at longer milling times. Likewise smaller particles sinter faster (higher driving force) and reduce the porosity difference inside and outside the large particles more quickly, causing a more homogeneous structure in terms of porosity and eventually grain size. Once the porosity difference in the two regions is reduced and eliminated, the driving force for increased diffusion and grain growth also disappears and small grains then grow faster for surface area reduction and "catch up" in grain size, creating a completely homogeneous structure in terms of porosity and grain size with sufficient sintering time and temperature.

5.5 Phase Identification

X-ray diffraction and scanning electron microscopy with energy dispersive X-ray spectroscopy were used to identify the phases present in the bulk material after sintering. Relevant XRD data can be seen in Figures 37 and 38, while SEM/EDS data can be found in Figures 48 – 51 and Tables 7 and 8. First, XRD curves were analyzed to look for secondary phase peaks in order to help identify precipitates that might be forming during sintering. This analysis showed the formation of two precipitate phases, one of which was fairly easily and confidently identified as matching the powder diffraction file for Fe_6W_6C. This phase showed more peaks with greater intensity than the other precipitate phase, indicating it likely represents a larger volume fraction of the sample and also making it easier to positively identify. The second phase was only observed in two small XRD peaks (at diffraction angles of 43.7° and 50.8° as seen in Figure 28). Based on their trends of increasing and decreasing intensity compared to the Fe_6W_6C peaks across the different milling times and sintering parameters, it became clear that these two peaks were generated by a distinct phase different from Fe_6W_6C.

However, positively identifying the phase off of only two peaks was more difficult than with Fe_6W_6C. When restricting the powder diffraction file search to only W, Ni, Fe, or C (possibly introduced through WC grinding media) containing phases, there are only two phases that have significant peaks near the two observed peaks: Ni_3Fe intermetallic phase or FCC Ni. Based on the Ni-Fe phase diagram [54] seen in Figure 55 and the 3:1 nickel to iron ratio, it is likely for the ordered Ni_3Fe phase to form. However, the significant shifting of the peaks from the powder diffraction file angles for Ni_3Fe as seen in Figure 38 cannot easily explained by compositional variation of the Ni_3Fe ordered phase. The FCC Ni phase, on the other hand, could be expected to exhibit the observed shift if significant amounts of W were to be dissolved in solid solution causing an increase in the lattice parameter. The pure nickel FCC lattice parameter is about 3.52 Å, but the observed shifted peaks indicate a lattice parameter of around 3.58 Å. According to the lattice spacing handbook [60], this lattice parameter increase correlates to about 15 at%

W dissolved in Ni. Figure 56 shows the W-Ni phase diagram [54], indicating significant solubility of W in Ni, which would be expected in this situation given the high W content and could explain the shifted XRD peaks by increasing the lattice parameter.

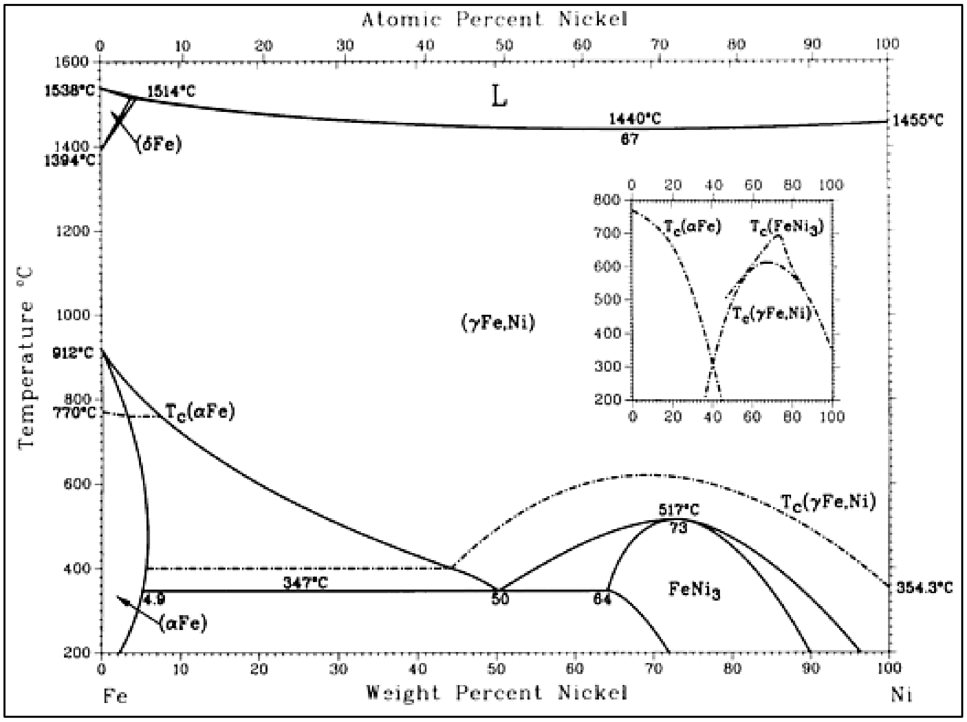

Figure 55 Fe-Ni phase diagram [54] Reprinted with permission of ASM International. All rights reserved. www.asminternational.org

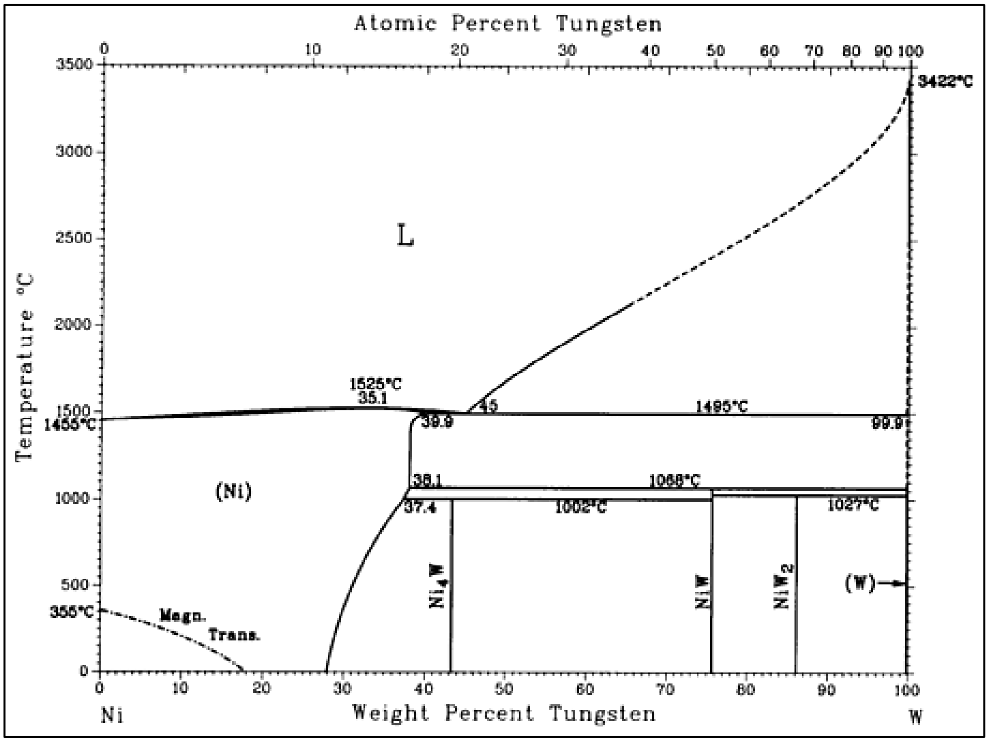

Figure 56 Ni-W phase diagram [54] Reprinted with permission of ASM International. All rights reserved. www.asminternational.org

With XRD seeming to provide initial indications to identify the two precipitate phases, SEM with EDS was used to improve this understanding by observing compositional variation within the microstructure. As described in Section 4.2.3.3, the very fine microstructure of the samples sintered below 1300°C made it difficult to confidently gather EDS data. Even with these challenges, Figure 48 shows clear evidence for the formation of two different Ni/Fe enriched phases in addition to the W matrix in a 1200°C sintered sample. Samples sintered to 1300°C with coarser microstructure (and similar-looking XRD peaks) were analyzed more extensively with EDS for secondary phases. These results showed three distinct phases: the W matrix phase with a W:Ni ratio of over 100 in general; the Ni/Fe elevated phase with a W:Ni ratio of about 5 and a Fe:Ni ratio of about 0.35; and the Ni/Fe rich phase with a W:Ni ratio of about 0.5 and a Fe:Ni ratio of about 0.33. It is interesting to note the consistent 3:1 nickel to iron ratio in both precipitate phases. Due to the similar size and weight of Ni and Fe compared to W, it was found useful to look at the Ni/Fe composition relative to the W composition and treat the system almost as a binary alloy. With this thought process, Table 9 was generated showing approximate weight percent ratios compared to estimated atomic percent ratios of W and Ni/Fe for the two precipitate phases using simple binary alloy system conversions and averaging the Ni and Fe atomic weights.

Table 9: Estimated Atomic and Weight Percent of Precipitate Phases Relative to Ni/Fe

Phase	Ni/Fe Elevated	Ni/Fe Rich
W:Ni/Fe in wt%	3.65	0.38
Ni/Fe	1	1
W:Ni/Fe in at%	1.13	0.12
Ni/Fe	1	1

Table 9 provides a better understanding of the EDS data by showing the atomic percent of Ni/Fe compared to W. It shows the Ni/Fe elevated phase to have almost a 1:1 W:Ni/Fe ratio, presenting more clearly the true chemical composition without the skewed wt% of the heavier W. This is consistent with the Fe_6W_6C-like structure matched in the XRD peaks. However, rather than being exactly Fe_6W_6C, the phase may be more like $(Fe, Ni)_6W_6C$, based on the 3:1 nickel to iron ratio present in this phase. Useful insights are also provided into the Ni/Fe rich phase, which has a W:Ni/Fe ratio of only 0.12. This Ni/Fe rich EDS data appears consistent with a solid solution of Ni, Fe, and W and also represents similar W content to the 15 at% W estimated from the lattice spacing handbook [60] for the observed XRD peak shift. As the W-Ni phase diagram shows, W can be expected to dissolve to about the amounts observed, and Fe is highly soluble in Ni as well. Another possibility is that this phase is actually only Ni and Fe and the small W EDS signal is simply due to the surrounding W-rich areas. However, the consistency of some of the W composition via EDS would seem to refute this explanation, which would expect at least a couple readings of much lower W content if the true phase is only Fe and Ni.

With the characterization techniques available to us, there is no good, clear-cut way to distinguish whether this Ni/Fe rich phase is an FCC solid solution of Ni, Fe, and W or the ordered Ni_3Fe with some signal leakage from the surrounding W matrix. An argument could be made either way, but based on the greater likelihood of XRD peak shift caused by dissolution of W into the FCC Ni lattice than shifting of the Ni_3Fe peaks as well as the consistent presence of significant W content with coarsening microstructure (even with less W signal leakage from surrounding areas), an FCC solid solution of Ni, Fe, and W is the more logical conclusion. The W composition matches quite well with the solubility of W in Ni from the W-Ni phase diagram and the 3:1 nickel to iron ratio is expected from the starting composition. Likewise, the observed XRD peak position is consistent with a Ni lattice with 15 at% W dissolved [60], which is quite similar to the W:Ni/Fe ratio of 0.12 measured by EDS. This error could be explained by experimentation and also by the effect of a significant amount of Fe dissolved in the W causing a confounding effect on the lattice parameter change.

Therefore, based on EDS and XRD analysis the observations are consistent with the precipitation of two secondary phases during sintering: $(Fe, Ni)_6W_6C$ and at a lower volume fraction an FCC solid solution of W, Ni, and Fe. $(Fe, Ni)_6W_6C$ will likely increase strength, but reduce ductility of the resulting bulk material, while the FCC solid solution will likely have the opposite effect. The increased strength is desirable, but the reduced ductility is very much not as this application requires high plasticity and shear banding to maximize penetration.

5.6 Hardness Testing and Mechanical Properties

Vickers micro and macrohardness testing were performed on all samples to assess mechanical properties as show in Figure 53. The hardness data generally followed the pattern in density, showing a strong increase with increasing sintering temperature as expected as well as a slight positive correlation with increasing milling time. One interesting observation was that hardness values seemed to max out at about 400 – 450 HV for most of the 1200 and 1300°C sintered samples. This can be explained by a combination of density and grain size. The 1200°C samples had slightly lower density, which would reduce hardness measurements, but also smaller grain size leading to higher hardness. Therefore, the two effects of density and grain size compensate for each other, leading to an effective maximum hardness around 400 – 450 HV.

Chapter 6

---

6. Conclusions

Powder processing of W – 3 wt% Ni – 1 wt% Fe was used to observe the effects of milling time and sintering temperature on densification, microstructure, grain size, and mechanical properties of the bulk material for potential replacement of depleted uranium in kinetic energy penetrators. The goal of this work is to be able to process a bulk nanocrystalline tungsten heavy alloy. SEM, XRD, and particle size analysis were used to assess the effects of milling. Milling produced a bimodal particle size distribution with one peak between 1 and 10 microns and the other between 50 and 150 microns. Particle size reduced slightly with increasing milling time, but maintained a bimodal distribution. XRD peak broadening analysis by the Williamson-Hall method showed lattice strain increasing to 1.5% during milling with crystallite size reduced to below 50 nm, while peak shifting indicated a reduction in W lattice parameter due to dissolution of Ni and Fe atoms into the W BCC lattice. Therefore, milling was shown to produce the desirable nanocrystalline structure as well as the metastable dissolution of Ni and Fe into the W lattice beyond equilibrium solubility limits.

Post-sintering bulk characterization showed density increasing strongly with increasing sintering temperature to above 90% of theoretical density at 1200°C. Density increased slightly and apparent activation energy for sintering decreased strongly with increasing milling time, probably due to greater Ni activation of W diffusion during sintering. SEM micrographs to examine microstructure showed the development of a bimodal grain size distribution with smaller, generally submicron grains in areas of lesser porosity and larger grains on the order of 1 – 4 μm in areas of greater porosity. This is believed to be connected to the bimodal particle size distribution from milling. XRD and SEM also showed the precipitation of two secondary phases during sintering: $(Fe, Ni)_6W_6C$ intermetallic incorporating carbon from the grinding media and an FCC solid solution of Ni, Fe, and W as Ni and Fe diffuse back out of the W lattice and incorporate some W. The intermetallic phase will increase strength but reduce ductility of the bulk material, which is not desirable, but the FCC phase will have the opposite effect of increasing ductility. Micro and macrohardness testing show similar trends generally following density with a strong correlation with sintering temperature and a weaker trend with increasing milling time. Vickers hardness appears to maximize at 400 – 450 HV after sintering at 1200 and 1300°C independent of milling or sintering time.

These results showed a powder processing approach to be a promising method of producing a bulk nanocrystalline tungsten heavy alloy. Milling produces a nanocrystalline structure and supersaturates the W lattice with Ni and Fe to improve sintering kinetics and impede grain growth. However, CIP and pressureless sintering are insufficient methods for achieving the high density and small grain size required for this application. Likewise, the precipitation of brittle phases is not beneficial for the high plasticity needed from penetrator material. However, these challenges can be overcome with appropriate modifications. Continued work with pure W and no alloying as well as other grinding media (to prevent the introduction of WC) could help to prevent brittle phase formation and better understand the cause of bimodal grain sizes. Quenching from high temperature rather than ambient cooling could also prevent brittle phase formation. Further work should include more advanced compaction and sintering techniques combining temperature and pressure simultaneously such as hot isostatic pressing or spark plasma sintering to maximize densification while minimizing grain growth. High strain-rate testing of the bulk samples is also needed to determine the critical grain size at which the desirable shear bands form. Future work might also consider reducing the amount of Ni and Fe to maintain activated sintering, but reduce or prevent the presence of brittle intermetallic phases that reduce ductility and therefore effectiveness as a penetrator material.

References

1. Miller, A.C., *Depleted Uranium: Properties, Uses, and Health Conesquenses.* 2007, Boca Raton, FL: CRC Press.

2. Dorsey, C.D., et al., *Biological monitoring for depleted uranium exposure in U.S. Veterans.* Environmental health perspectives, June, 2009. **117**(6): p. 953-956.

3. van der Voet, G.B., et al., *Metals and health: a clinical toxicological perspective on tungsten and review of the literature.* Military medicine, September, 2007. **172**(9): p. 1002-1005.

4. Combat, C.o.T.a.R.E.f.E.t.D.U.D.a.A., *Review of the Toxicological and Radiologic Risks to Military Personel from Exposures to Depleted Uranium During and After Combat*. 2008, Washington, DC: National Academies Press.

5. Esquivel, E.V., et al., *Comparison of flow and shear band structures in oriented, columnar tungsten, single crystal tungsten-tantalum ands intered tungsten heavy alloy ballistic penetrators.* Powder Metallurgy, 2003. **46**(2): p. 137.

6. Fan, J., et al., *Thermal stability, grain growth and structure changes of mechanically alloyed W-Ni-Fe composite during annealing.* International Journal of Refractory Metals and Hard Materials, 2001. **19**(2): p. 73-77.

7. Hong, S.H., *Processing, microstructure and mechanical properties of mechanically alloyed tungsten heavy alloy.* Journal of metastable and nanocrystalline materials, 2003. **15**: p. 665-672.

8. Hwang, K.S., et al., *Sintering of nanosized tungsten prepared by ultrahigh energy milling.* Adv. Powder Metall. Part. Mater., 2009(Copyright (C) 2011 American Chemical Society (ACS). All Rights Reserved.): p. 8/65-8/71.

9. Jang, J.S.C., *Nano-scaled microstructure evolution of W-Ni-Fe-Co heavy alloy by mechanical alloying.* Journal of metastable and nanocrystalline materials, 2005. **24**: p. 133-136.

10. Krüger, L., et al., *Stress state influence ondynamic strength and failure behaviour of tungstenheavy alloys.* Powder Metallurgy, 2003. **46**(2): p. 132.

11. Magness, L., *The performance of a nanocrystalline tungsten composite in ballistic impacts.* Proceedings of SPIE, the international society for optical engineering, 2002. **4608**: p. 216-224.

12. Mathaudhu, S.N., et al., *Microstructures and recrystallization behavior of severely hot-deformed tungsten.* Materials Science and Engineering: A, 2009. **503**(1-2): p. 28-31.

13. Ryu, H.J., *Microstructure and mechanical properties of mechanically alloyed and solid-state sintered tungsten heavy alloys.* Materials science & engineering. A, Structural materials : properties, microstructure and processing, 2000. **291**(1): p. 91-96.

14. Wei, Q., et al., *Nanoengineering opens a new era for tungsten as well.* JOM Journal of the Minerals, Metals and Materials Society, 2006. **58**(9): p. 40-44.

15. Magness, L. *Demonstration of Tungsten Nanocomposite Alternatives to Depleted Uranium in Anti-Armor Penetrators*. 2010 July 19, 2010 February 17, 2011]; Available from:

http://prod.serdp-estcp.org/Program-Areas/Weapons-Systems-and-Platforms/Energetic-Materials-and-Munitions/Ammunition-and-Projectiles/WP-200805/WP-200805/(modified)/19Jul2010.

16. Cho, K., et al., *Nanocrystalline and Ultra-Fine Grained Tungsten for Kinetic Energy Penetrator and Warhead Liner Applications*. 2006, Army Research Laboratory: Aberdeen Proving Ground, MD.

17. Wei, Q., et al., *Nanoengineering Applied to Tungsten*. 2006, Army Research Laboratory: Aberdeen Proving Ground, MD.

18. Klotz, B.R., et al., *Characterization, Processing, and Consolidation of Nanoscale Tungsten Powder*. 2009, Army Research Laboratory: Aberdeen Proving Ground, MD.

19. Wei, Q., et al., *Effect of nanocrystalline and ultrafine grain sizes on the strain rate sensitivity and activation volume: fcc versus bcc metals.* Materials Science and Engineering A, 2004. **381**(1-2): p. 71-79.

20. Wei, Q., et al., *Microstructure and mechanical properties of super-strong nanocrystalline tungsten processed by high-pressure torsion.* Acta Materialia, 2006. **54**(15): p. 4079-4089.

21. Eksi, A. and M.K. Kulekci, *Hardness and Densification Behaviour of Copper and Bronze Powders Compacted with Uniaxial Die and Cold Isostatic Pressing Processes.* Metalurgija, 2004. **43**(2): p. 129-134.

22. Lee, H.F., et al., *The production of aluminium alloy composites using a cold isostatic press and extrusion approach.* Journal of Materials Processing Technology, 1992. **29**: p. 245-253.

23. Majumdar, S., et al., *A study on preparation of Mo–0.6Ti–0.2Zr–0.02C alloy by mechanical alloying and hot isostatic pressing, and its characterization.* Materials Chemistry and Physics, 2009. **113**: p. 562-566.

24. Ye, J., L. Ajdelsztajn, and J.M. Schoenung, *Bulk Nanocrystalline Aluminum 5083 Alloy Fabricated by a Novel Technique: Cryomilling and Spark Plasma Sintering.* Metallurgical and Materials Transactions A, 2006. **37A**: p. 2569-2579.

25. *File: Sabot separating.gif*. Available from: http://commons.wikimedia.org/wiki/File:Sabot_separating.gif.

26. Parkhurst, M.A., et al., *Depleted Uranium Aerosol Doses and Risks*. 2005, Columbus, OH: Battelle Press.

27. Marshall, A.C., *An Analysis of Uranium Dispersal and Health Effects Using a Gulf War Case Study*. 2005, Sandia National Laboratories: Albuquerque, NM.

28. Environment, D.o.t.P.o.t.H., *Depleted uranium: Sources, Exposure, and Health Effects*. 2001, World Health Organization: Geneva.

29. Rogers, H., *Adiabatic Plastic Deformation.* Annual Review of Materials Science, 1979. **9**: p. 283-311.

30. Wright, T.W., *The Physics and Mathematics of Adiabatic Shear Bands*. 2002, Cambridge: Cambridge University Press.

31. Stevens, J.B. and R.C. Batra. *Adiabatic Shear Banding and Axisymmetric Impact and Penetration Problems*. [cited 2011 March 28]; Available from: http://www.sv.vt.edu/research/batra-stevens/pent.html.

32. Wei, Q., et al., *Mechanical behavior and dynamic failure of high-strength ultrafine grained tungsten under uniaxial compression.* Acta Materialia, 2006. **54**(1): p. 77-87.

33. Benjamin, J.S., *Mechanical Alloying.* Scientific American, 1976. **234**(5): p. 108-116.

34. Benjamin, J.S. and T.E. Volin, *Mechanism of Mechanical Alloying.* Metallurgical Transactions, 1974. **5**(8): p. 1929-1934.

35. Suryanarayana, C., *Mechanical alloying and milling.* Progress in Materials Science, 2001. **46**(1-2): p. 1-184.

36. Suryanarayana, C., *Recent Developments in Mechanical Alloying.* Reviews on Advanced Materials Science, 2008. **18**(3): p. 203-211.

37. German, R.M., *Powder Metallurgy*. 2005, Princeton, NJ: Metal Powders Industries Federation.

38. Zhan, Y., et al., *Cu–Cr–Zr alloy matrix composite prepared by powder metallurgy method.* Powder Metallurgy, 2006. **49**(3): p. 253-257.

39. Aning, A.O., Z. Wang, and T.H. Courtney, *Tungsten solution kinetics and amorphization of nickel in mechanically alloyed Ni-W alloys.* Acta metallurgica et materialia, 1993. **41**(1): p. 165-174.

40. Zeagler, A., *Structure and Processing Relations in Ni-W Amorphous Particle Strengthened Ni Matrix Composites*, in *Materials Science and Engineering*. 2008, Virginia Polytechnic Institute and State University: Blacksburg.

41. German, R.M. and Z.A. Munir, *Enhanced Low-Temperature Sintering of Tungsten.* Metallurgical Transactions A, 1976. **7A**: p. 1873-1877.

42. Gessinger, G.H. and H.F. Fischmesiter, *A Modified Model for the Sintering of Tungsten with Nickel Additions.* Journal of the Less-Common Metals, 1972. **27**: p. 129-141.

43. Boonyongmaneerat, Y., *Effects of low-content activators on low-temperature sintering of tungsten.* Journal of Materials Processing Technology, 2009. **209**: p. 4084-4087.

44. Moon, I.-H., S.-T. Oh, and Y.-L. Kim, *Effect of Nickel Additive on the Grain Growth of Tungsten Wire.* Journal of the Less-Common Metals, 1989. **153**: p. 275-283.

45. Hwang, N.M., et al., *Activated Sintering of Nickel-Doped Tungsten: Approach by Grain Boundary Structural Transition.* Scripta Materialia, 2000. **42**: p. 421-425.

46. Jing-lian, F., et al., *Preparation of fine grain tungsten heavy alloy with high properties by mechanical alloying and yttrium oxide addition.* Journal of Materials Processing Technology, 2008. **208**: p. 463-469.

47. Lee, K.H., et al., *Effect of mechanical alloying process on microstructure and mechanical properties of ODS tungsten heavy alloys.* Journal of Alloys and Compounds, 2007. **434-435**: p. 433-436.

48. Fan, J.L., et al., *Dynamic failure and adiabatic shearbands in fine-grain 93W–4.9Ni–2.1Fe alloy with Y2O3 addition under lower high-strain-rate (HSR) compression.* Mechanics of Materials, 2009.

49. Sarkar, R., et al., *Characterisation and sintering studies of mechanically milled nano tungsten powder.* Powder Metallurgy, 2008. **51**(2).

50. Wang, H., et al., *Sinter-ability of nanocrystalline tungsten powder.* International Journal of Refractory Metals and Hard Materials, 2010. **28**: p. 312-316.

51. Xiao-qiang, L., et al., *Microstructure and properties of ultra-fine tungsten heavy alloys prepared by mechanical alloying and electric current activated sintering.* Transactions of Nonferrous Metals Sociey of China, 2010. **20**: p. 443-449.

52. Callister Jr., W.D., *Materials Science and Engineering An Introduction*. 7th ed. 2007, New York: John Wiley & Sons, Inc.

53. Nagender Naidu, S.V., A.M. Sriramamurthy, and P. Rama Rao, *Fe-W (Iron-Tungsten).* Binary Alloy Phase Diagrams, 1990. **2**: p. 1791-1793.

54. Baker, H., ed. *ASM Handbook, Volume 3 - Alloy Phase Diagrams*. 1992, ASM International.

55. Williamson, G.K. and W.H. Hall, *X-ray line broadening from filed aluminium and wolfram.* Acta Metallurgica, 1953. **1**(1): p. 22-31.

56. Meier, M., *Measuring Crystallite Size Using X-ray Diffraction, The Williamson-Hall Technique*. 2005, University of California, Davis: Davis, CA.

57. Lab, S.C. *t-Based Confidence Interval for the Mean*. 2003 [cited 2011; Available from: http://www.stat.wmich.edu/s216/book/node79.html.

58. Williams, K.L., *An Association of Awaruite with Heazelwoodite.* The American Mineralogist, 1960. **45**: p. 450-453.

59. Swanson, T., National Bureau of Standards (U.S.) Circular 539, 1953. **13**.

60. Pearson, W.B., ed. *A Handbook of Lattice Spacings and Structures of Metals and Alloys*. Vol. 1. 1958, Pergamon Press: New York.

Appendix A: Powder Characterization

A.1 Particle Size Analysis

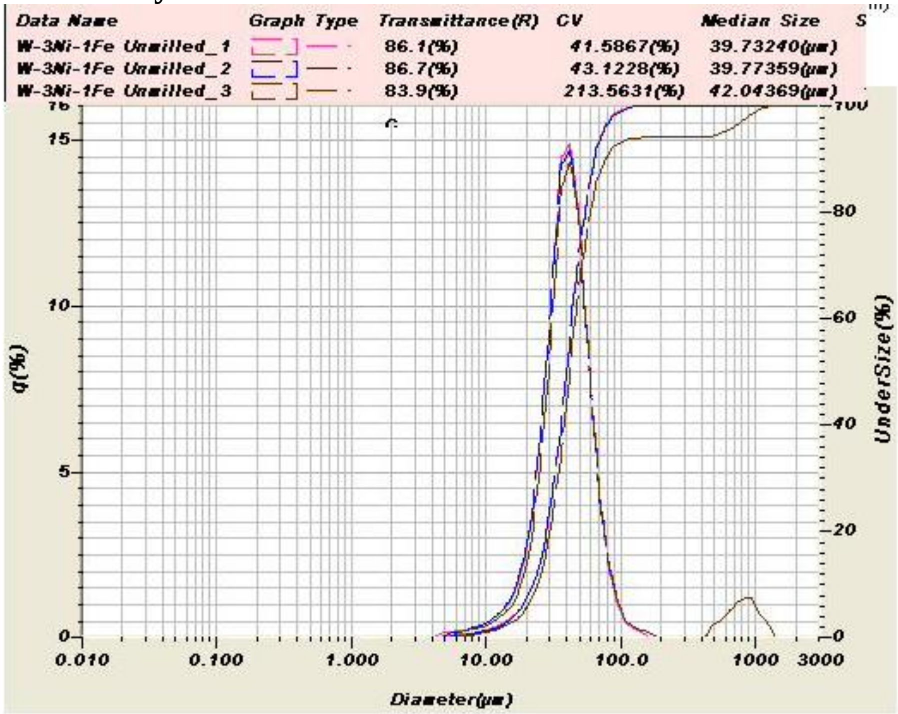

Data Name	Graph Type	Transmittance(R)	CV	Median Size
W-3Ni-1Fe Unmilled_1	▭ — ·	86.1(%)	41.5867(%)	39.73240(µm)
W-3Ni-1Fe Unmilled_2	▭ — ·	86.7(%)	43.1228(%)	39.77359(µm)
W-3Ni-1Fe Unmilled_3	▭ — ·	83.9(%)	213.5631(%)	42.04369(µm)

Fig. A1.1 Unmilled W-3Ni-1Fe particle size distributions

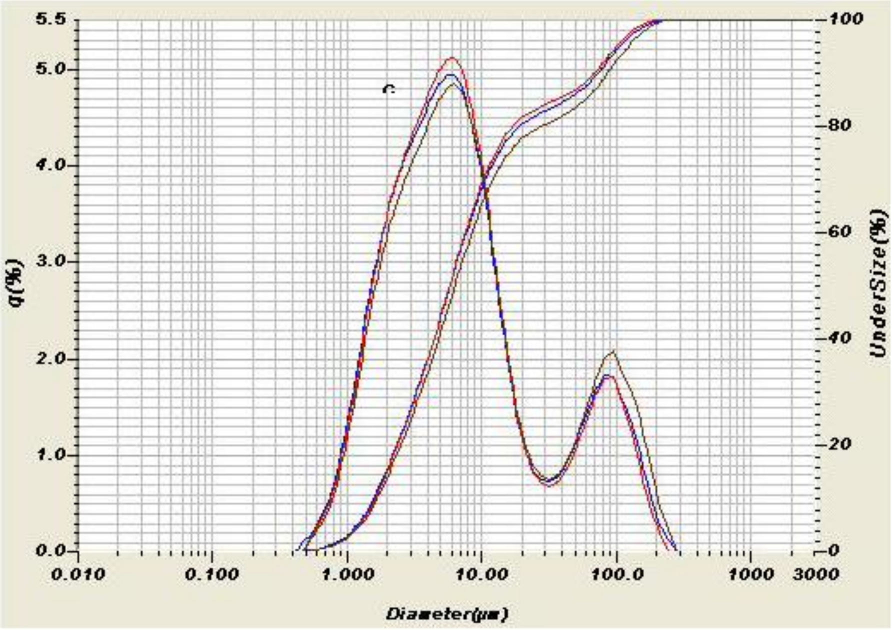

Fig. A1.2 15 hour milled W-3Ni-1Fe particle size distributions

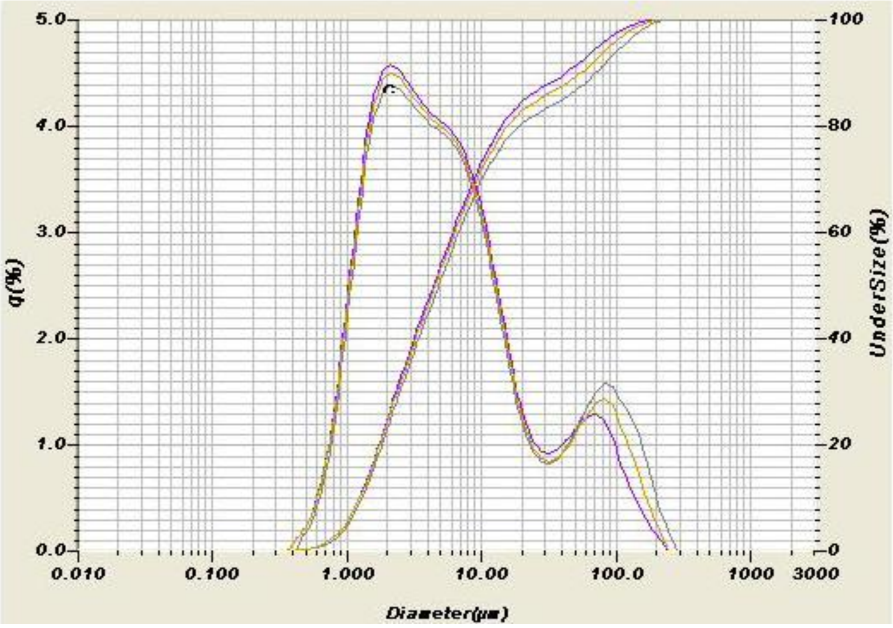

Fig. A1.3 25 hour milled W-3Ni-1Fe particle size distributions

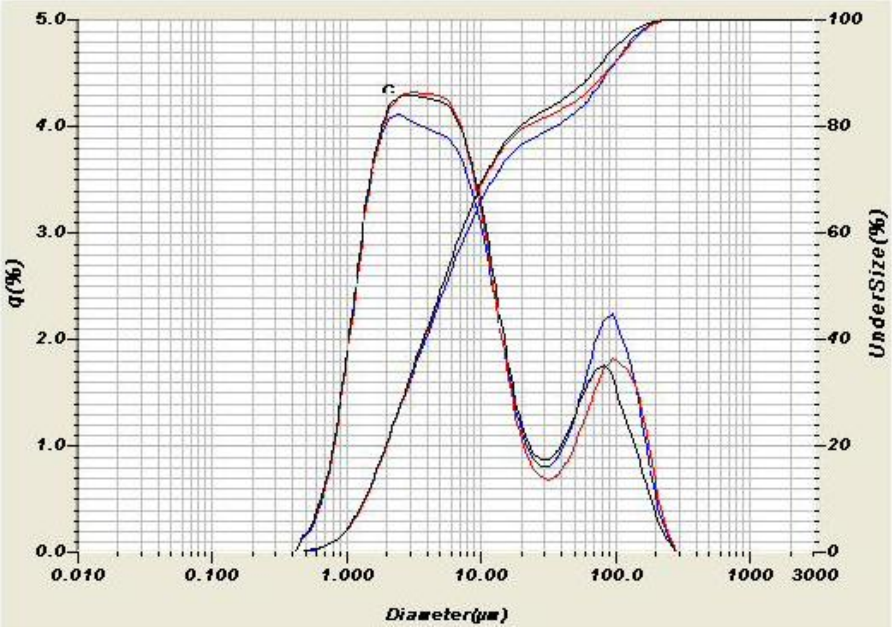

Fig. A1.4 50 hour milled W-3Ni-1Fe particle size distributions

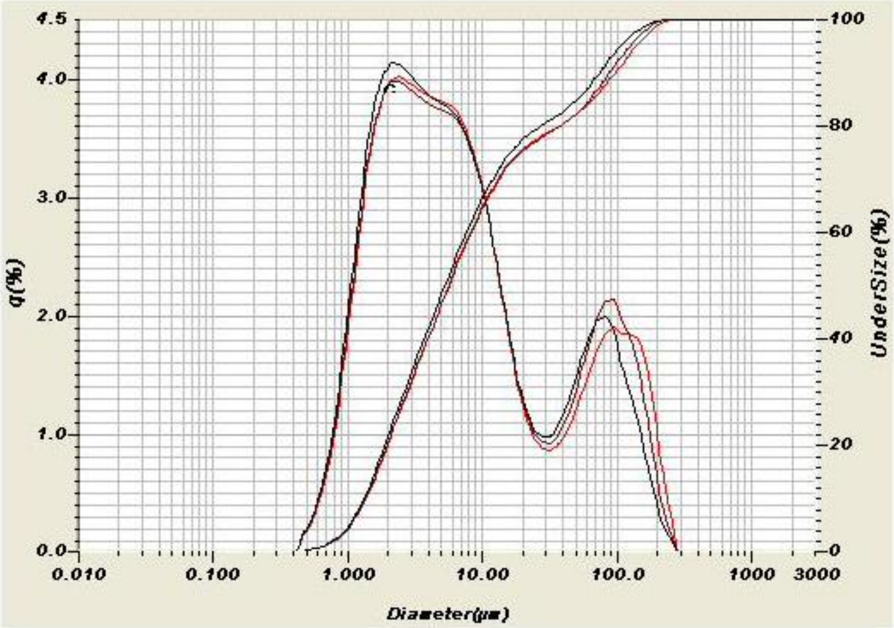

Fig. A1.5 100 hour milled W-3Ni-1Fe particle size distributions

A.2 Scanning Electron Microscopy

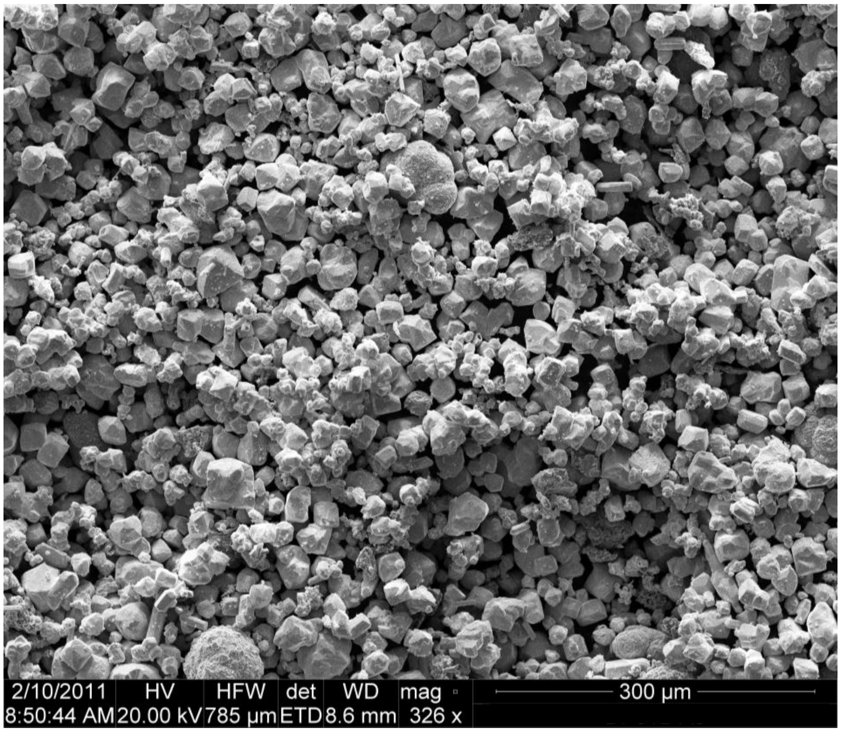

Fig. A2.1 Low-magnification SEM micrograph of unmilled W-3Ni-1Fe particles

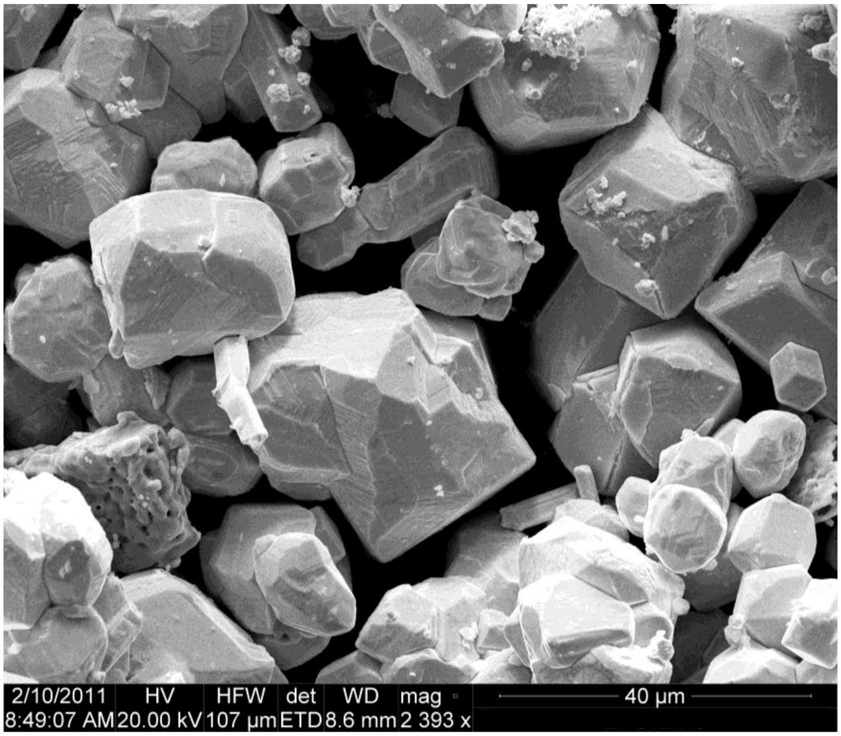

Fig. A2.2 High-magnification SEM micrograph of unmilled W-3Ni-1Fe particles

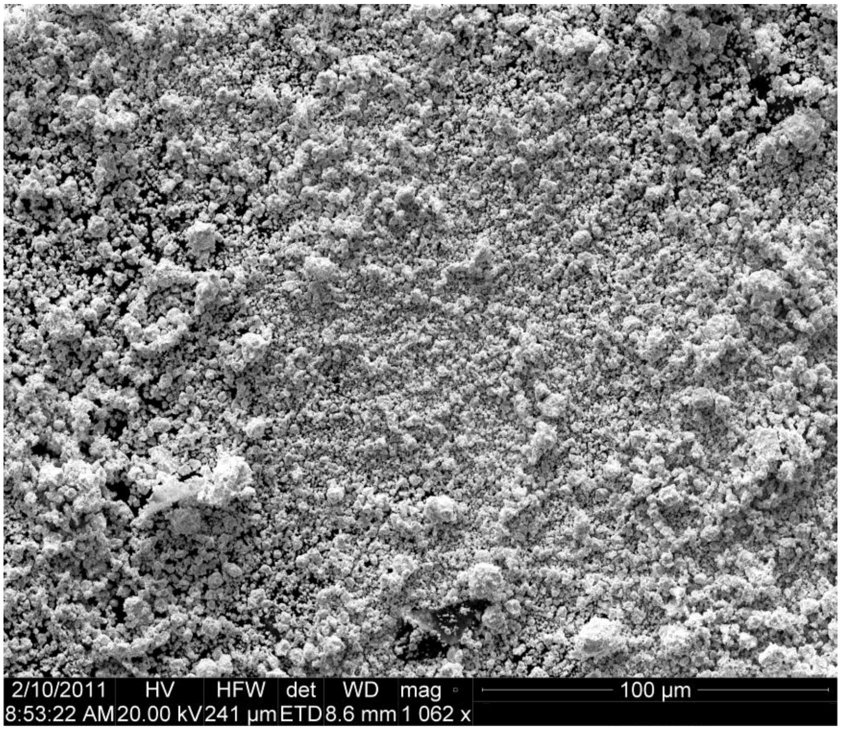

Fig. A2.3 SEM micrograph of 15 hour milled W-3Ni-1Fe particles

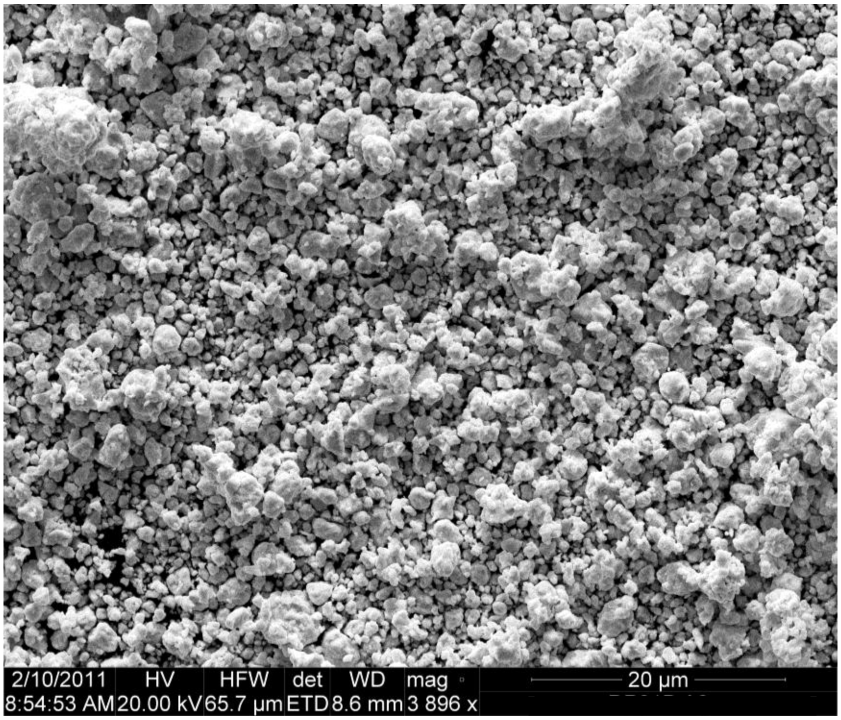

Fig. A2.4 SEM micrograph of 15 hour milled W-3Ni-1Fe particles

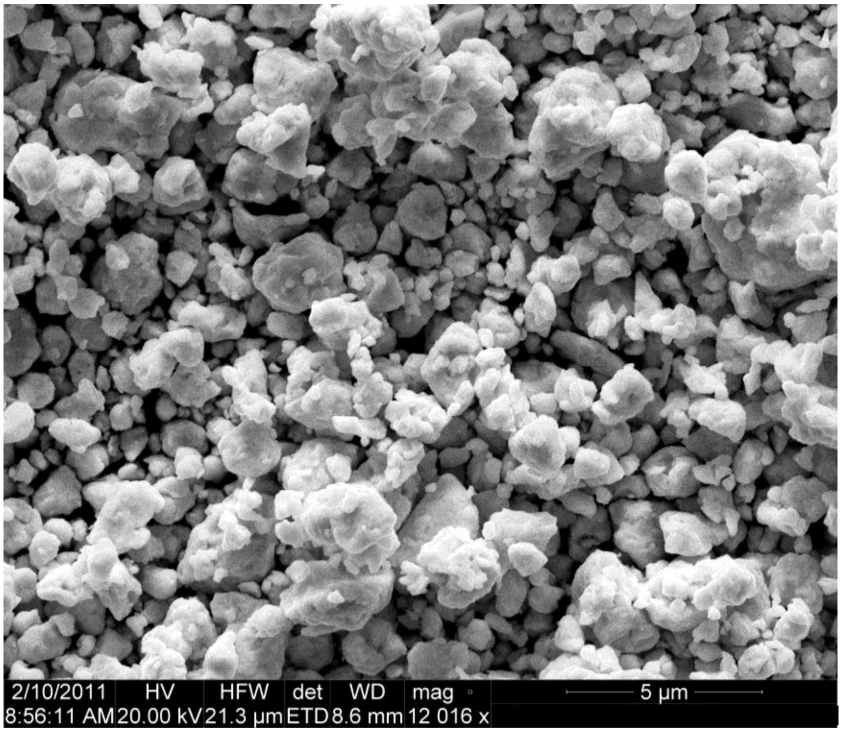

Fig. A2.5 SEM micrograph of 15 hour milled W-3Ni-1Fe particles

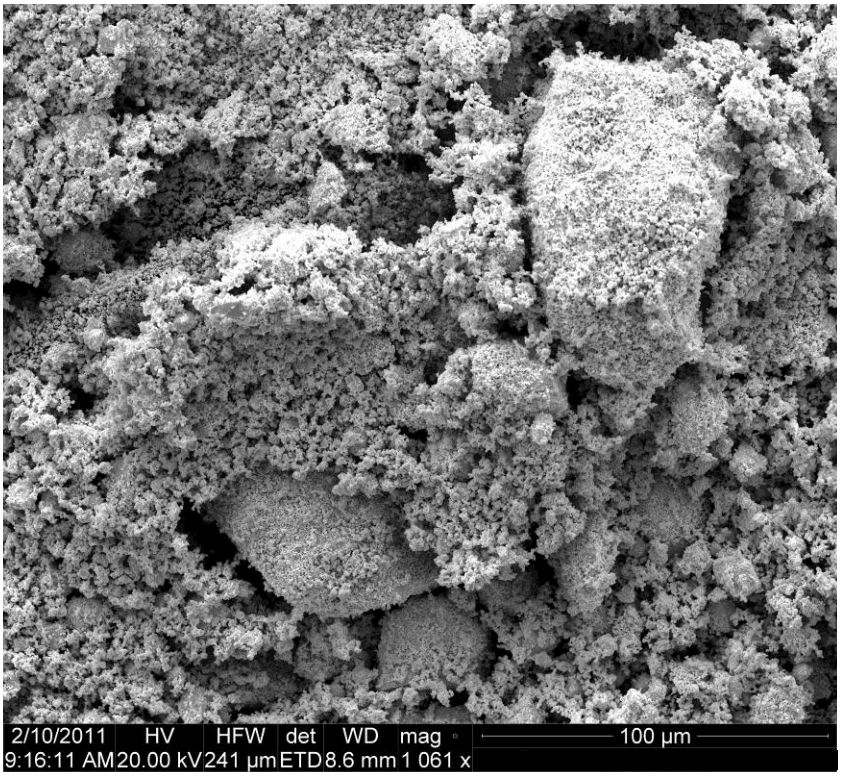

Fig. A2.6 SEM micrograph of 25 hour milled W-3Ni-1Fe particles

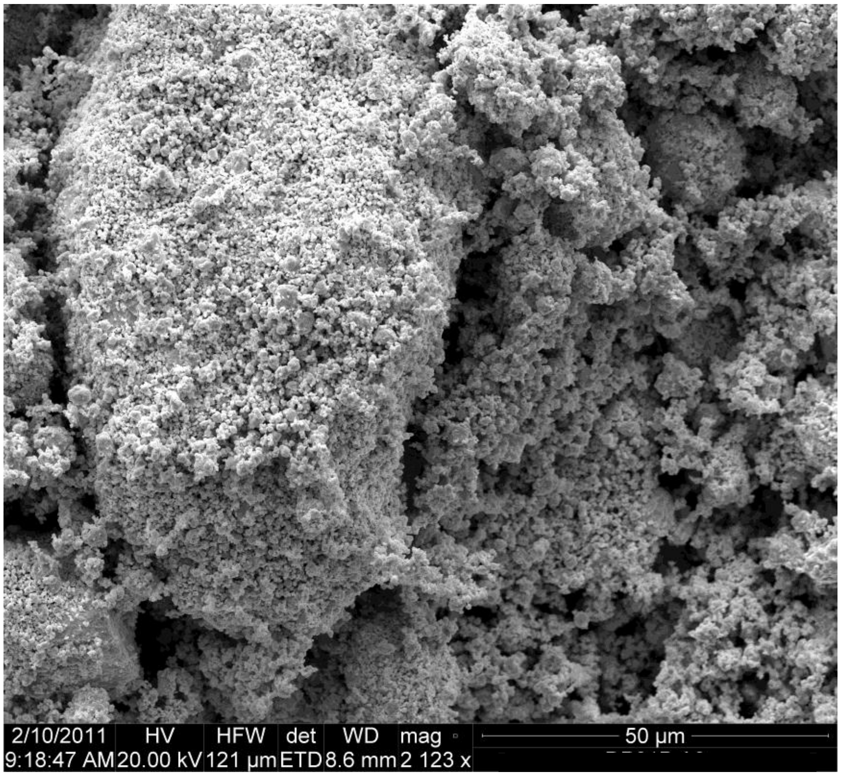

Fig. A2.7 SEM micrograph of 25 hour milled W-3Ni-1Fe particles

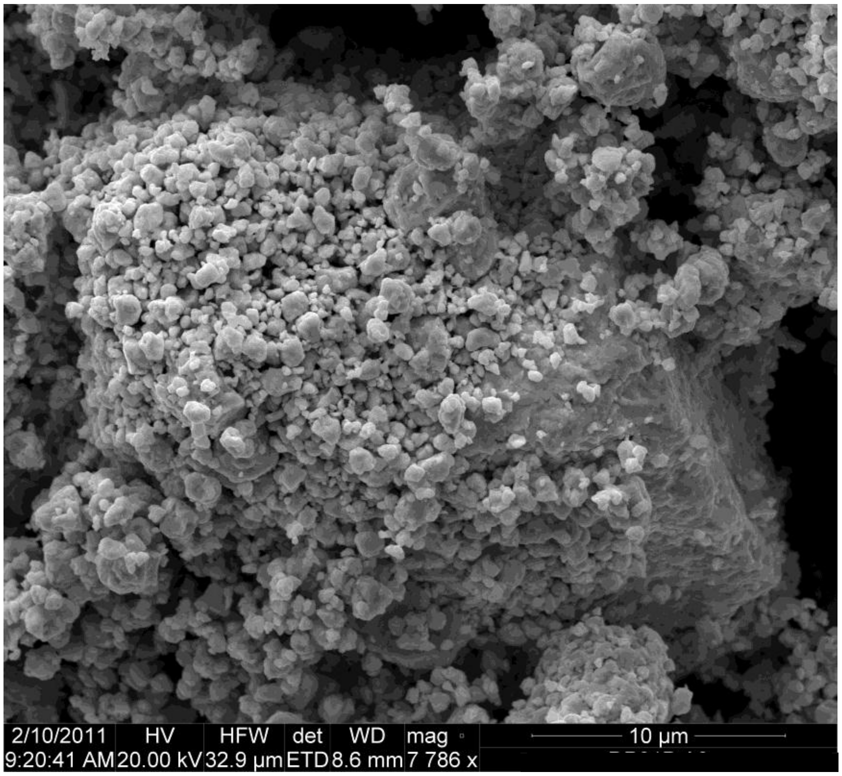

Fig. A2.8 SEM micrograph of 25 hour milled W-3Ni-1Fe particles

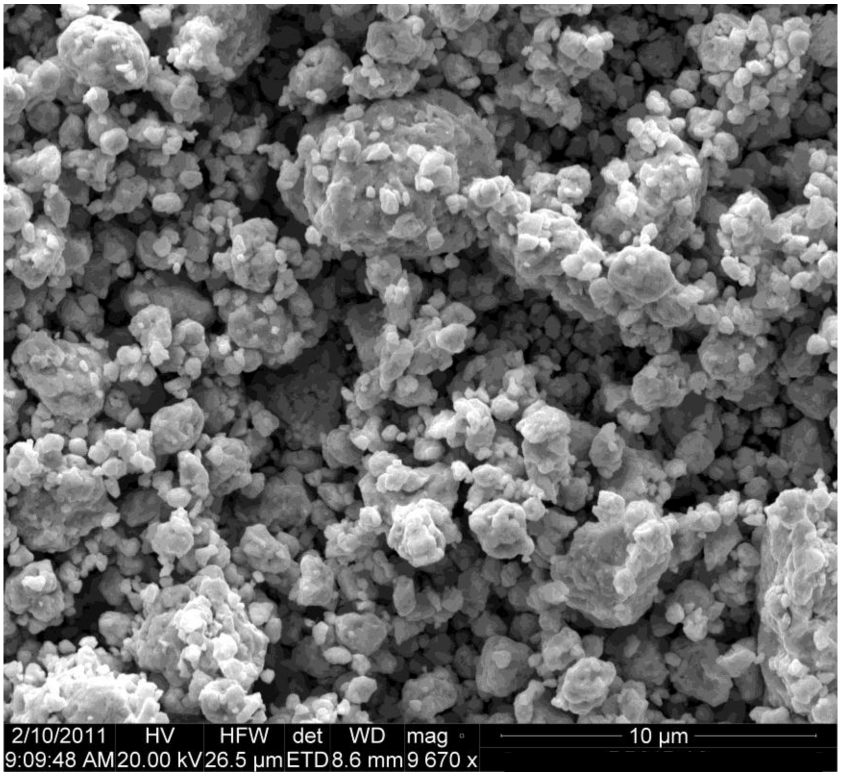

Fig. A2.9 SEM micrograph of 25 hour milled W-3Ni-1Fe particles

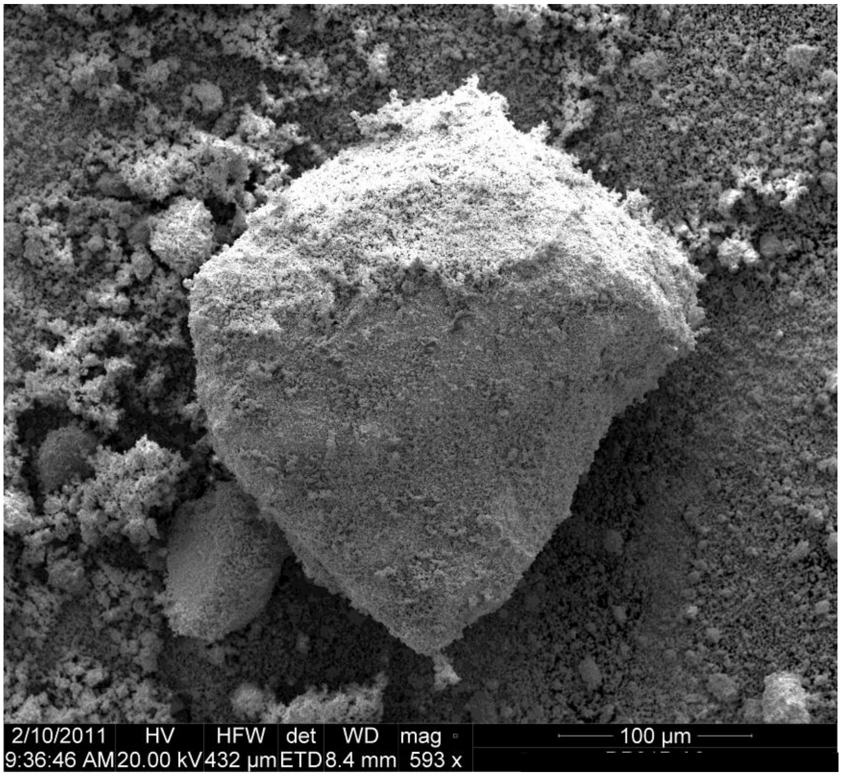

Fig. A2.10 SEM micrograph of 100 hour milled W-3Ni-1Fe particles

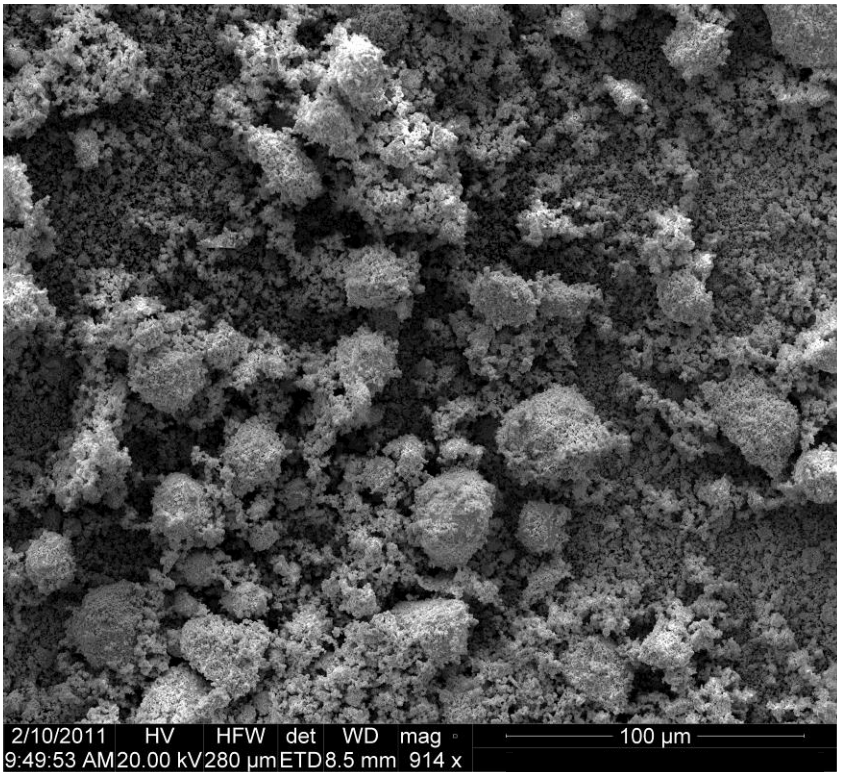

Fig. A2.11 SEM micrograph of 100 hour milled W-3Ni-1Fe particles

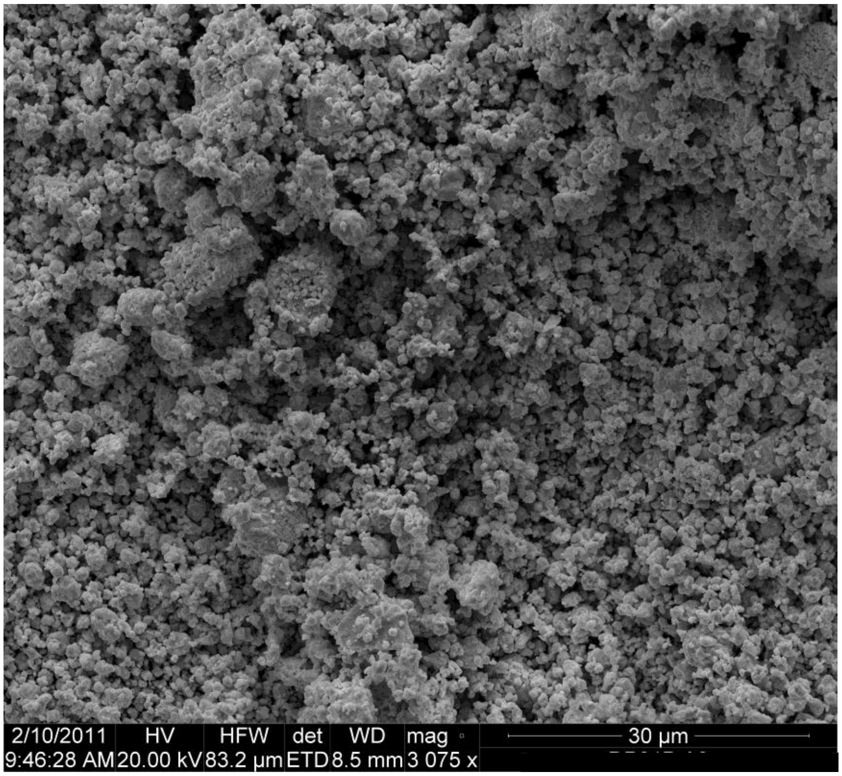

Fig. A2.12 SEM micrograph of 100 hour milled W-3Ni-1Fe particles

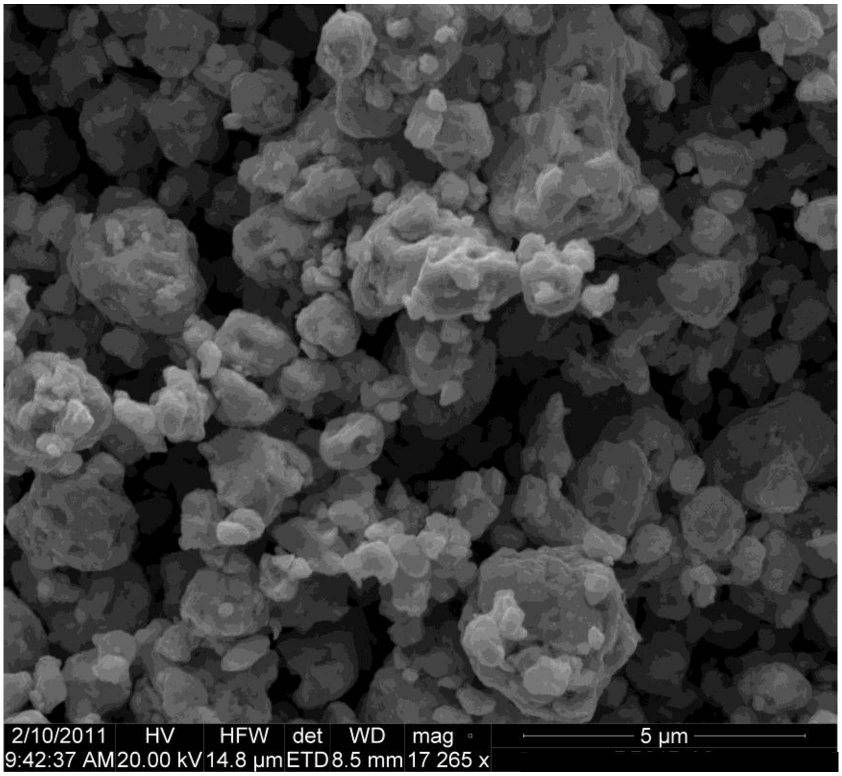

Fig. A2.13 SEM micrograph of 100 hour milled W-3Ni-1Fe particles

A.3 X-ray Diffraction (XRD)

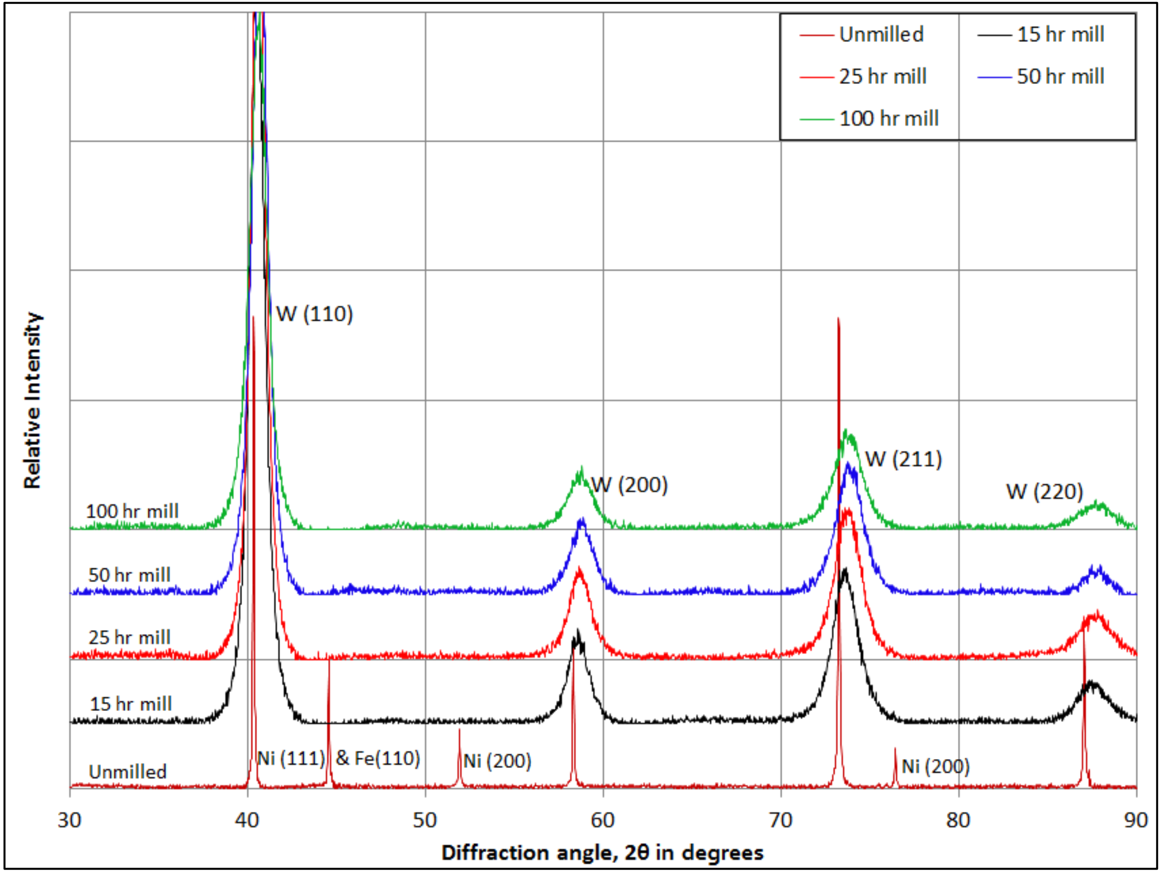

Figure A3.1 Full XRD curves of unmilled, 15, 25, 50, and 100 hour milled powder samples

Appendix B: Bulk Characterization

B.1 X-Ray Diffraction (XRD)

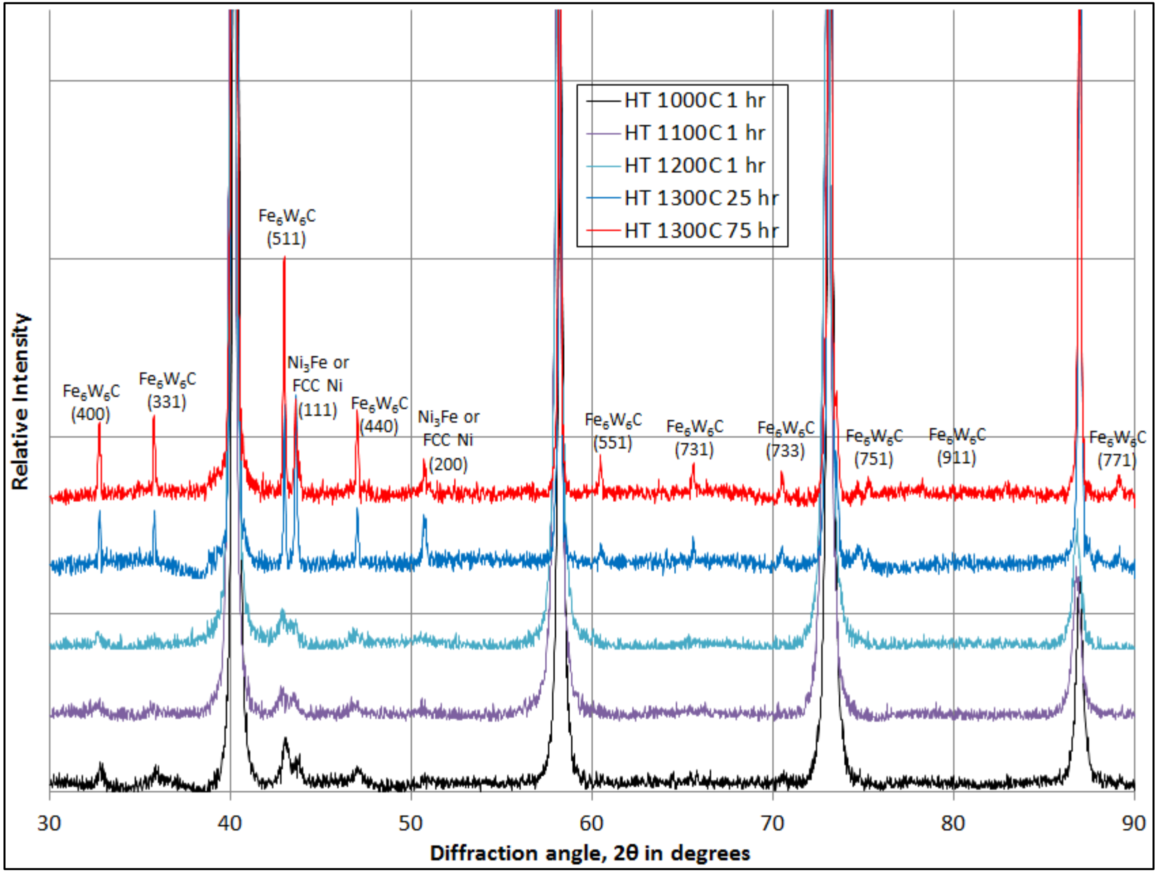

Figure B1.1 XRD curves for 15 hour milled samples – sintering temp increases vertically as indicated in legend

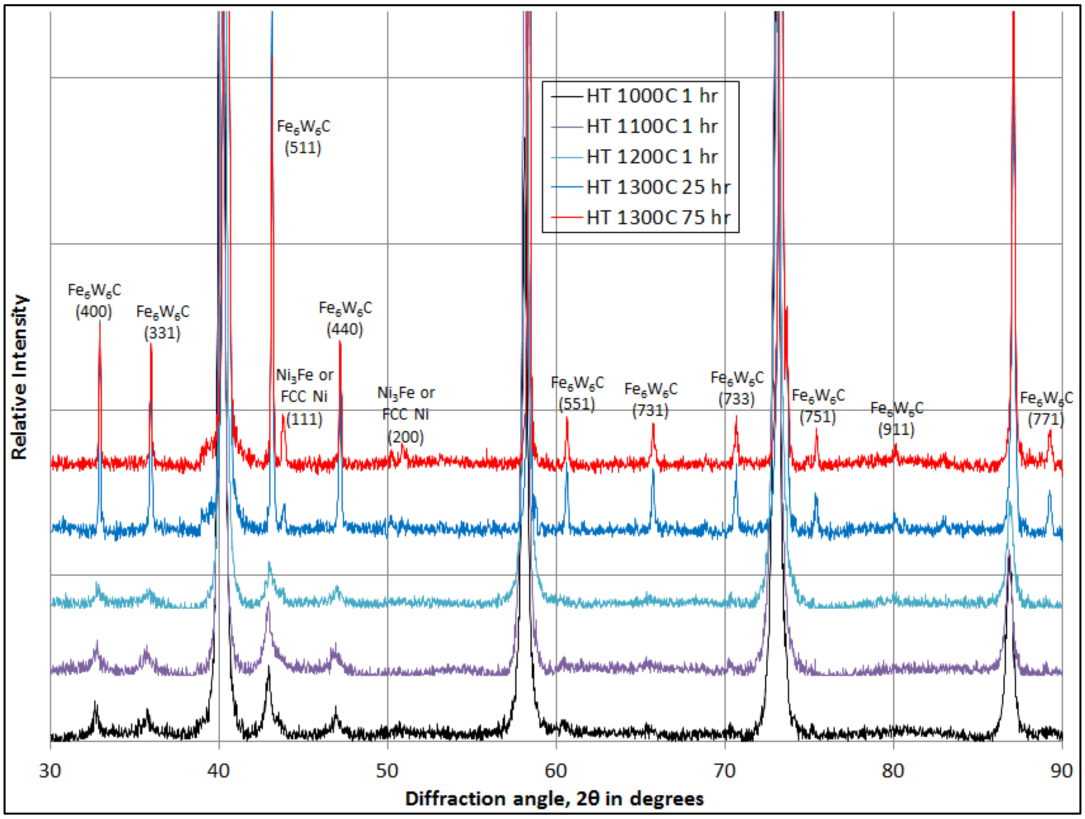

Figure B1.2 XRD curves for 25 hour milled samples – sintering temp increases vertically as indicated in legend

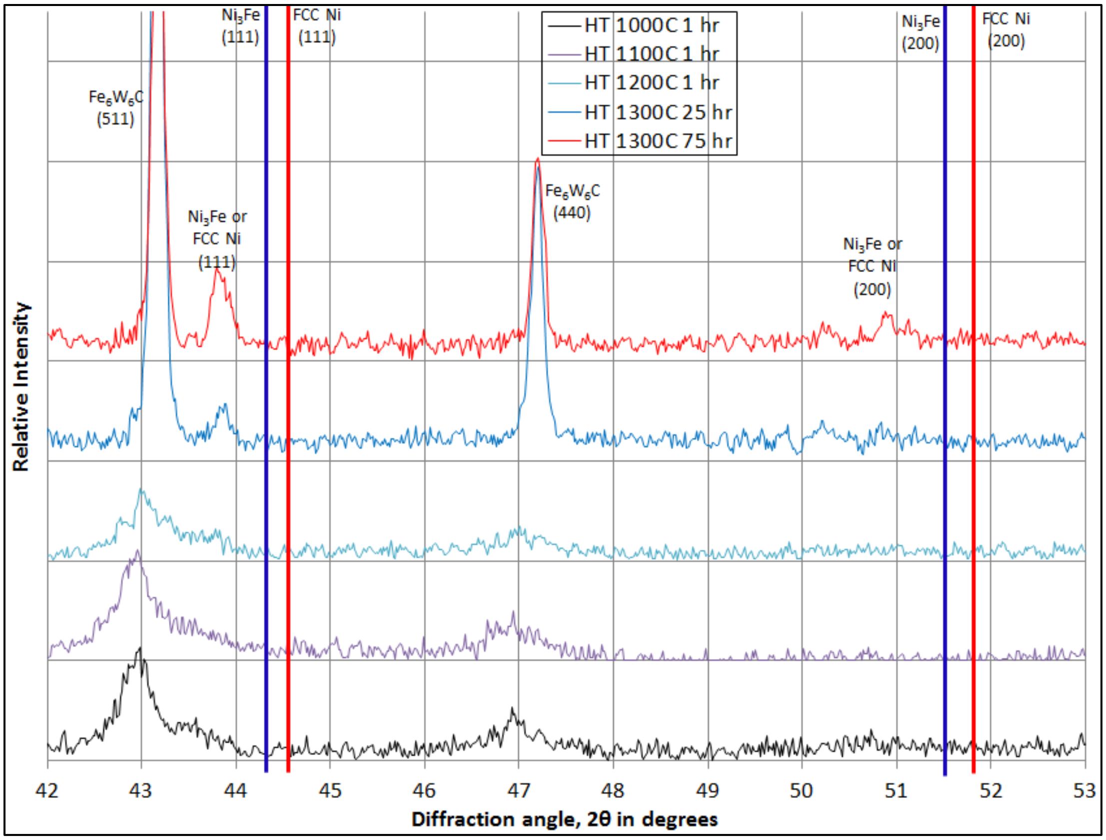

Figure B1.3 XRD curves for 25 hour milled samples with vertical lines drawn indicating expected peak positions for Ni$_3$Fe and FCC Ni – sintering temp increases vertically as indicated in legend

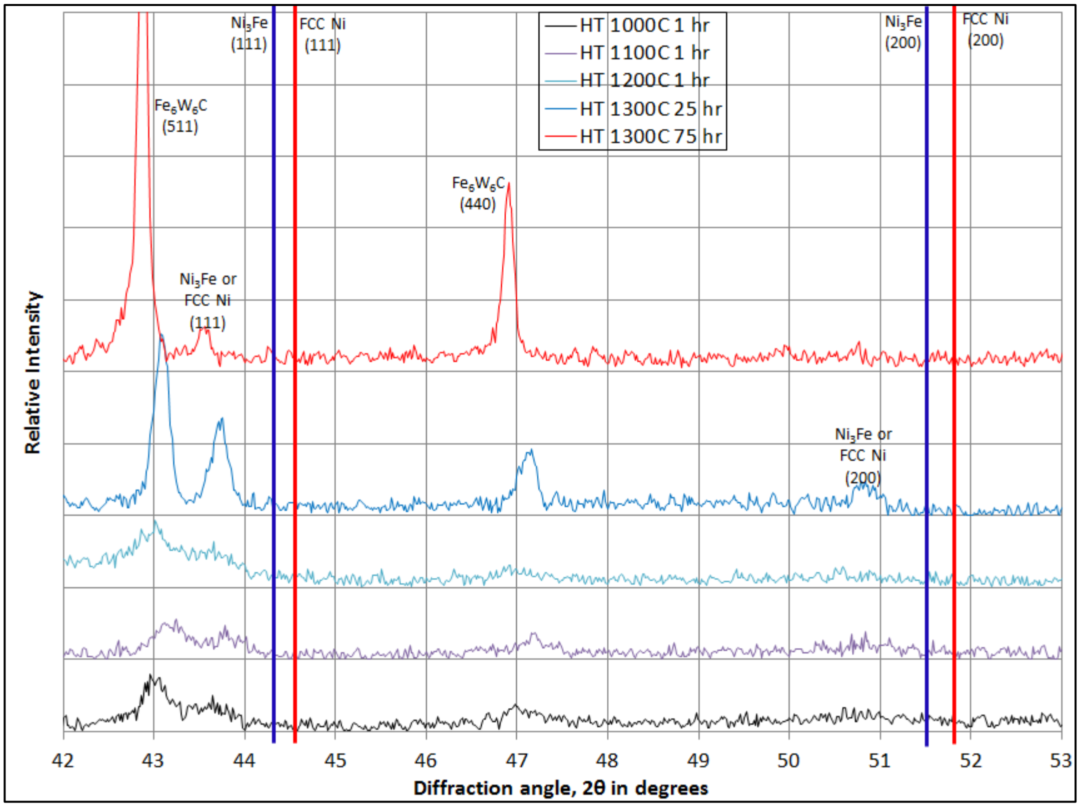

Figure B1.4 XRD curves for 50 hour milled samples with vertical lines drawn indicating expected peak positions for Ni$_3$Fe and FCC Ni – sintering temp increases vertically as indicated in legend

B.2 Scanning Electron Microscopy (SEM)

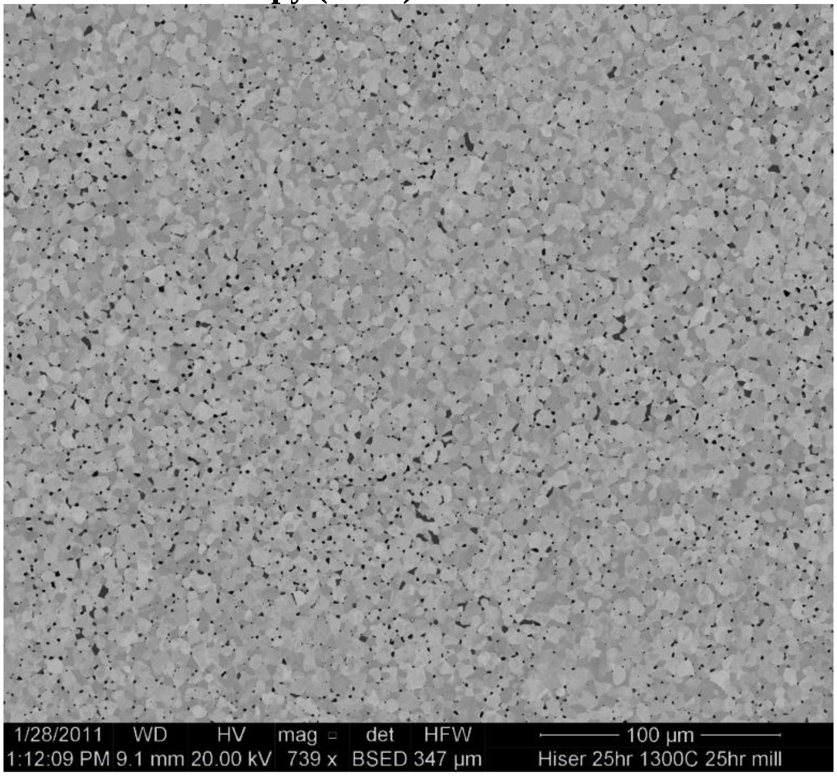

Figure B2.1 SEM micrograph of 25 hour milled 1300°C 25 hour sintered W-3Ni-1Fe

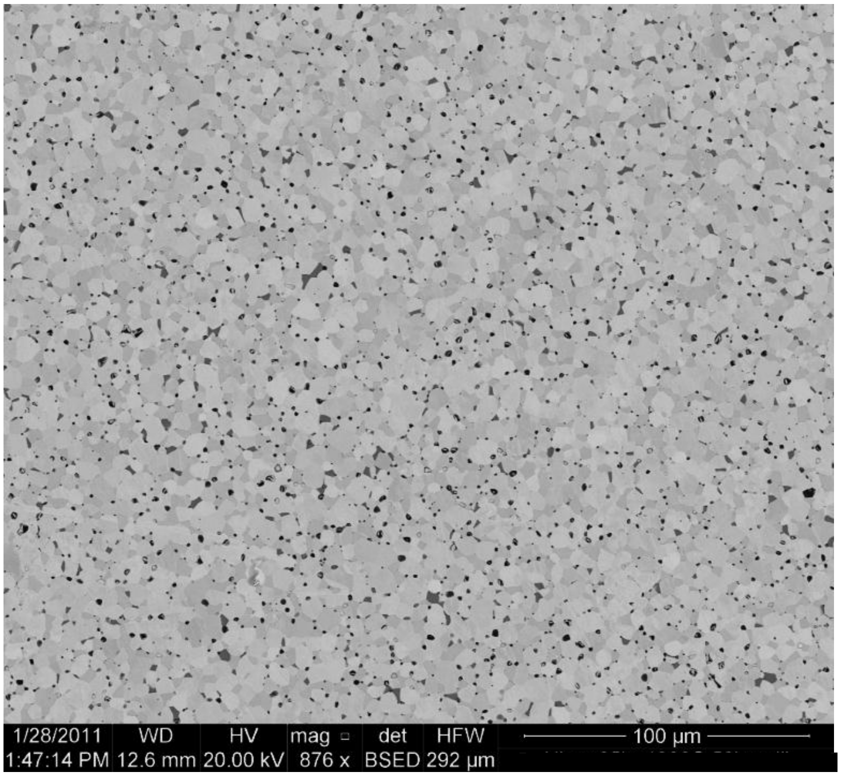

Figure B2.2 SEM micrograph of 50 hour milled 1300°C 75 hour sintered W-3Ni-1Fe

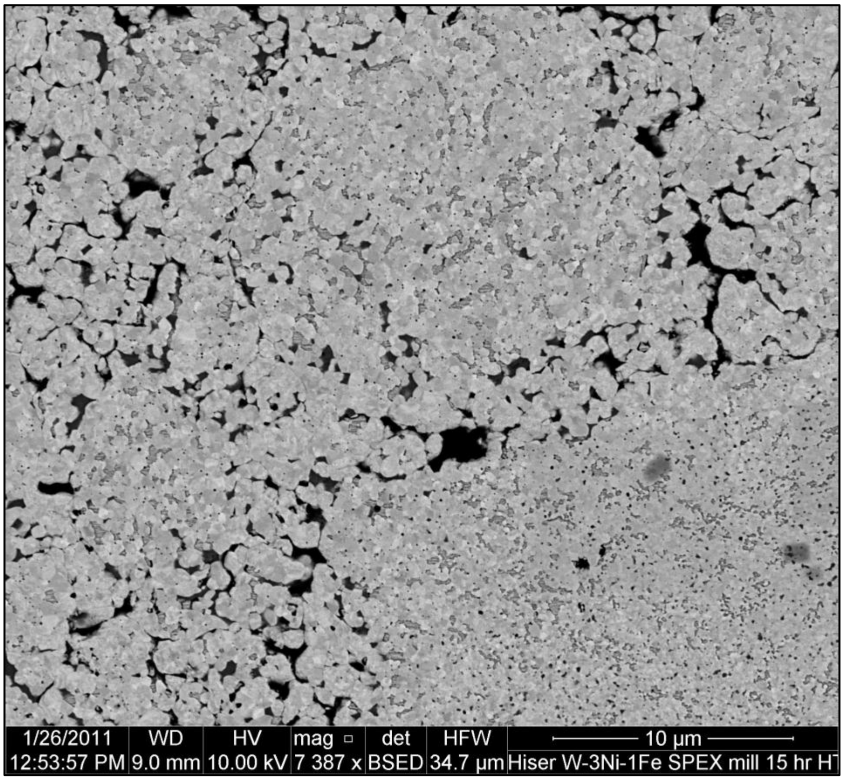

Figure B2.3 SEM micrograph of 15 hour milled 1000°C sintered W-3Ni-1Fe

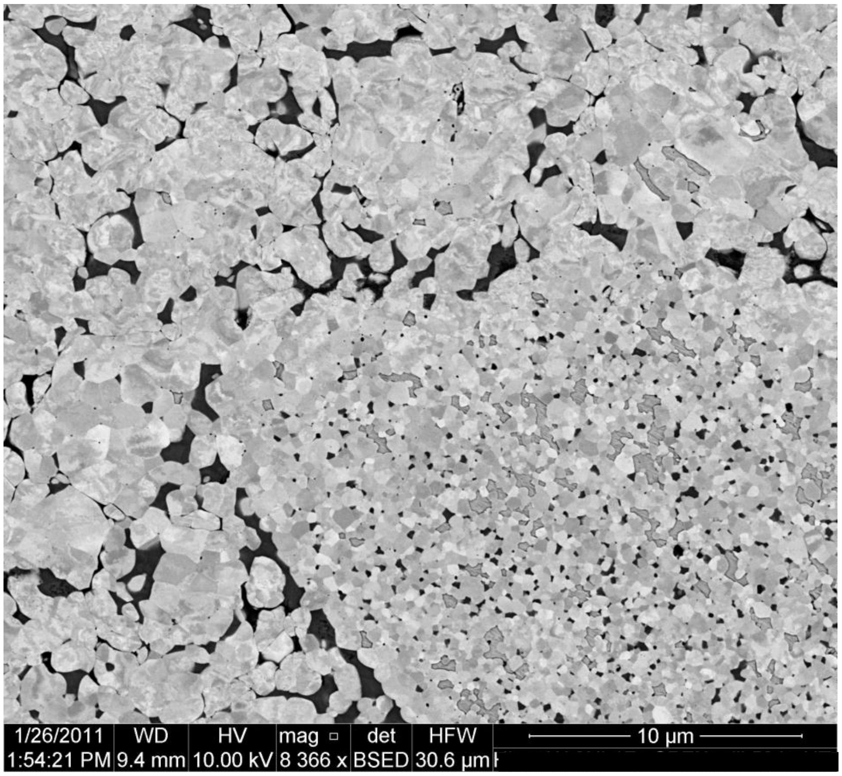

Figure B2.4 SEM micrograph of 15 hour milled 1100°C sintered W-3Ni-1Fe

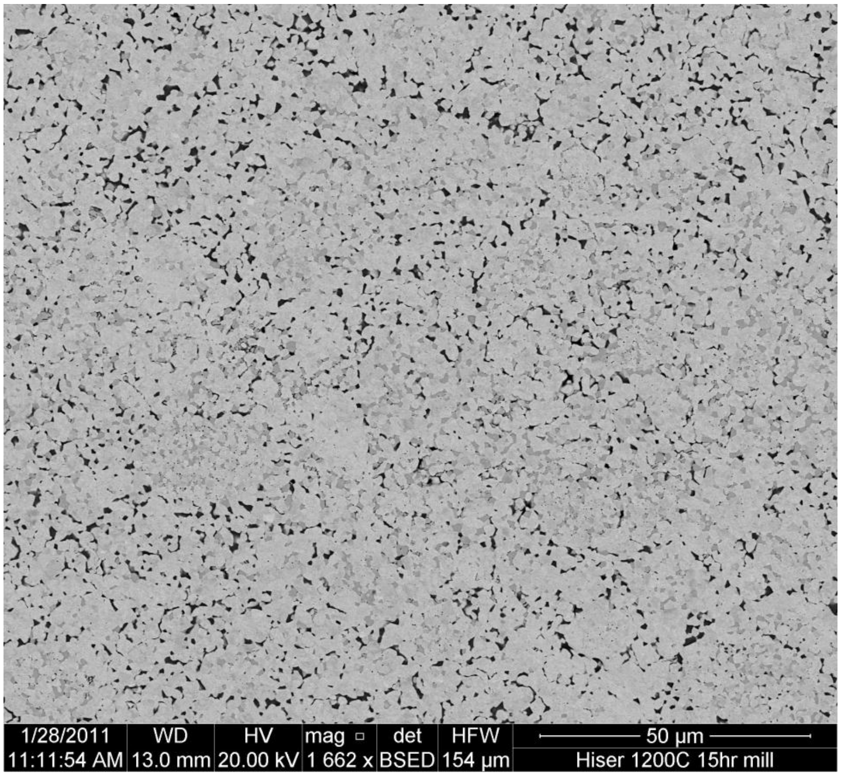

Figure B2.5 SEM micrograph of 15 hour milled 1200°C sintered W-3Ni-1Fe

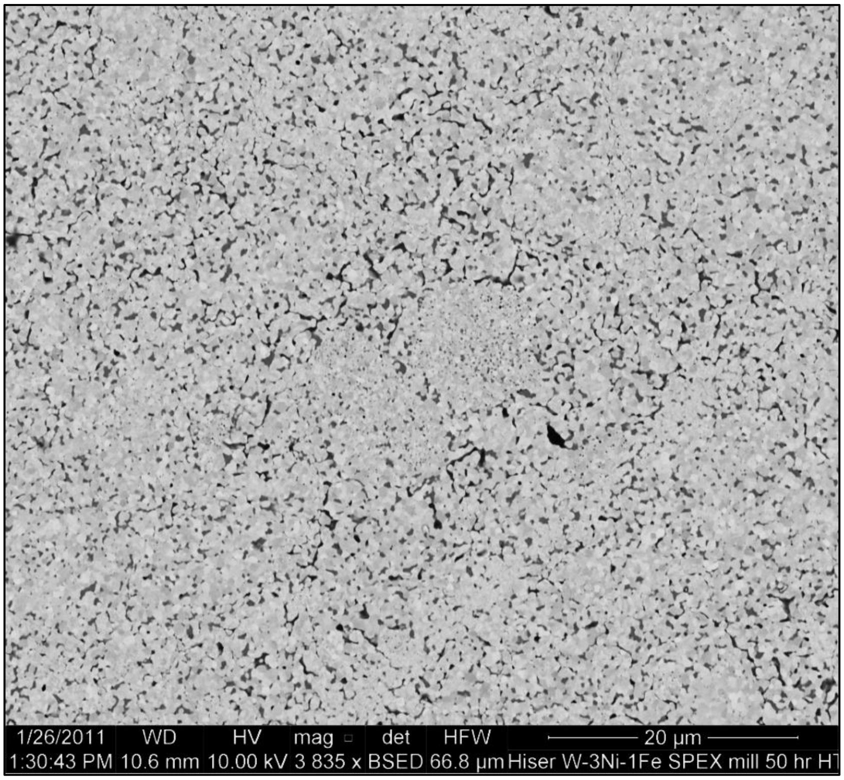

Figure B2.6 SEM micrograph of 50 hour milled 1000°C sintered W-3Ni-1Fe

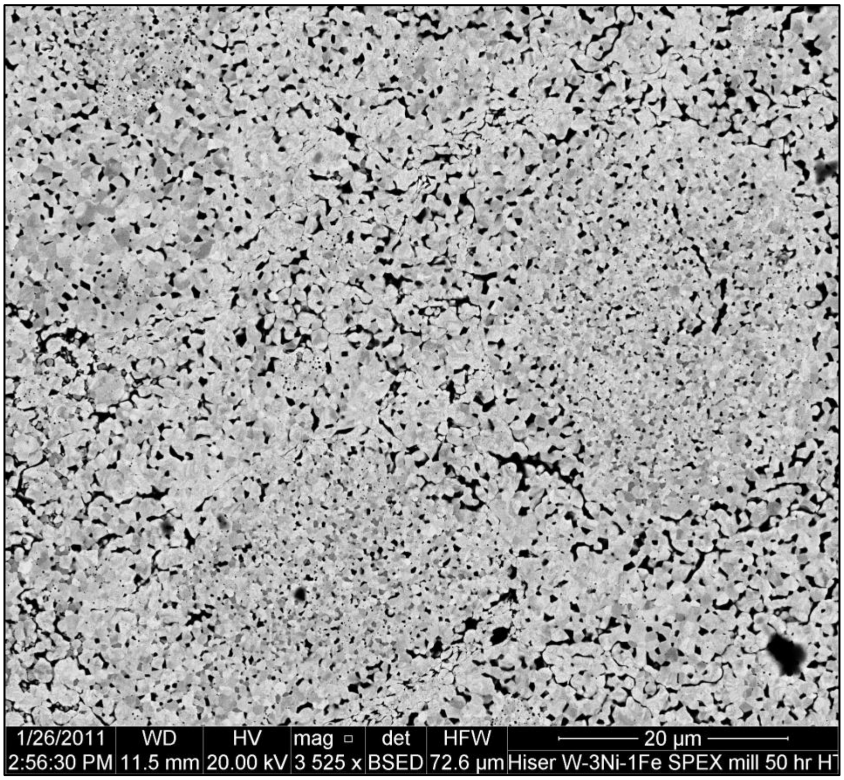

Figure B2.7 SEM micrograph of 50 hour milled 1100°C sintered W-3Ni-1Fe

Table B2.1: W Matrix Phase Point-Based EDS Composition Readings

Sample (Relative to Ni in wt%)	W:Ni	Ni	Fe:Ni
15 hr mill 1100°C for 1 hr HT	42.26	1	0.60
25 hr mill 1100°C for 1 hr HT	85.08	1	0.88
15 hr mill 1200°C for 1 hr HT	94.44	1	0.71
25 hr mill 1200°C for 1 hr HT	136.89	1	1
50 hr mill 1200°C for 1 hr HT	156.75	1	0.98
15 hr mill 1300°C for 25 hr HT	123.15	1	0.85
25 hr mill 1300°C for 25 hr HT	133.20	1	0.93
50 hr mill 1300°C for 25 hr HT	137.10	1	0.79
50 hr mill 1300°C for 25 hr HT	136.95	1	0.95
50 hr mill 1300°C for 25 hr HT	107.12	1	0.58
50 hr mill 1300°C for 25 hr HT	141	1	0.86
50 hr mill 1300°C for 25 hr HT	141.09	1	0.79
15 hr mill 1300°C for 75 hr HT	159.40	1	0.87
25 hr mill 1300°C for 75 hr HT	143.12	1	0.81
25 hr mill 1300°C for 75 hr HT	113.11	1	0.83
50 hr mill 1300°C for 75 hr HT	136.96	1	0.93
50 hr mill 1300°C for 75 hr HT	118.72	1	0.77
50 hr mill 1300°C for 75 hr HT	137	1	0.90
50 hr mill 1300°C for 75 hr HT	118.73	1	0.75
Average	114.48	1	0.80

Table B2.2: Ni/Fe Elevated Point-Based EDS Composition Readings

Sample (Relative to Ni in wt%)	W:Ni	Ni	Fe:Ni
15 hr mill 1100°C for 1 hr HT	3.66	1	0.36
25 hr mill 1100°C for 1 hr HT	5.40	1	0.35
15 hr mill 1200°C for 1 hr HT	4.95	1	0.34
25 hr mill 1200°C for 1 hr HT	7.14	1	0.35
25 hr mill 1200°C for 1 hr HT	6.63	1	0.40
50 hr mill 1200°C for 1 hr HT	4.89	1	0.35
50 hr mill 1200°C for 1 hr HT	5.33	1	0.34
50 hr mill 1300°C for 25 hr HT	4.69	1	0.35
50 hr mill 1300°C for 25 hr HT	4.72	1	0.32
50 hr mill 1300°C for 25 hr HT	4.72	1	0.33
15 hr mill 1300°C for 75 hr HT	4.65	1	0.33
25 hr mill 1300°C for 75 hr HT	4.66	1	0.35
50 hr mill 1300°C for 75 hr HT	4.58	1	0.35
50 hr mill 1300°C for 75 hr HT	4.93	1	0.36
50 hr mill 1300°C for 75 hr HT	4.86	1	0.38
Average	4.96	1	0.35

B.3 Hardness Testing

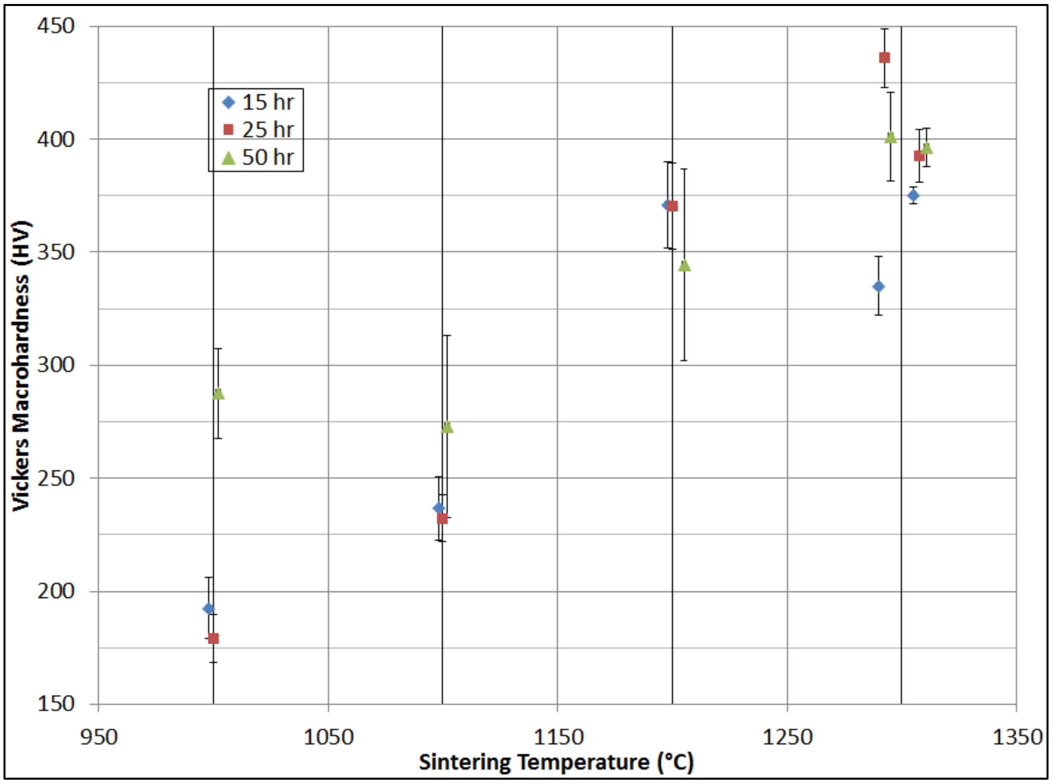

Figure B3.1 Macrohardness as a function of sintering temperature for all three milling times

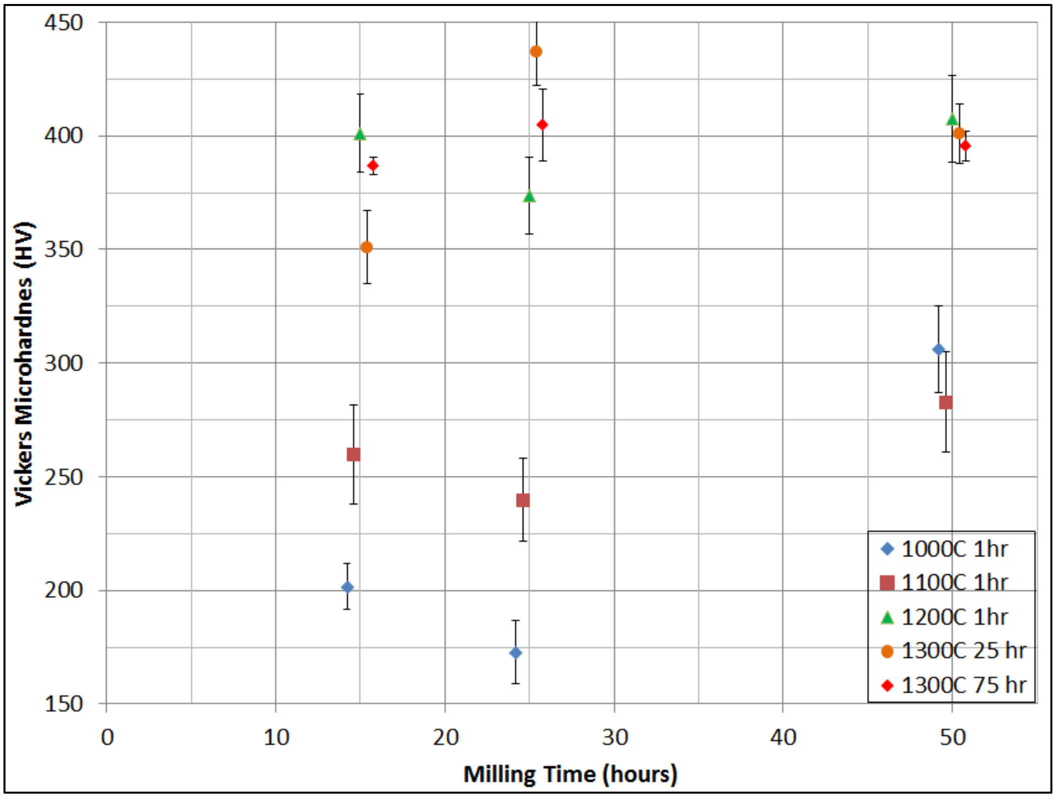

Figure B3.2 Microhardness as a function of milling time for all sintering temperatures and times

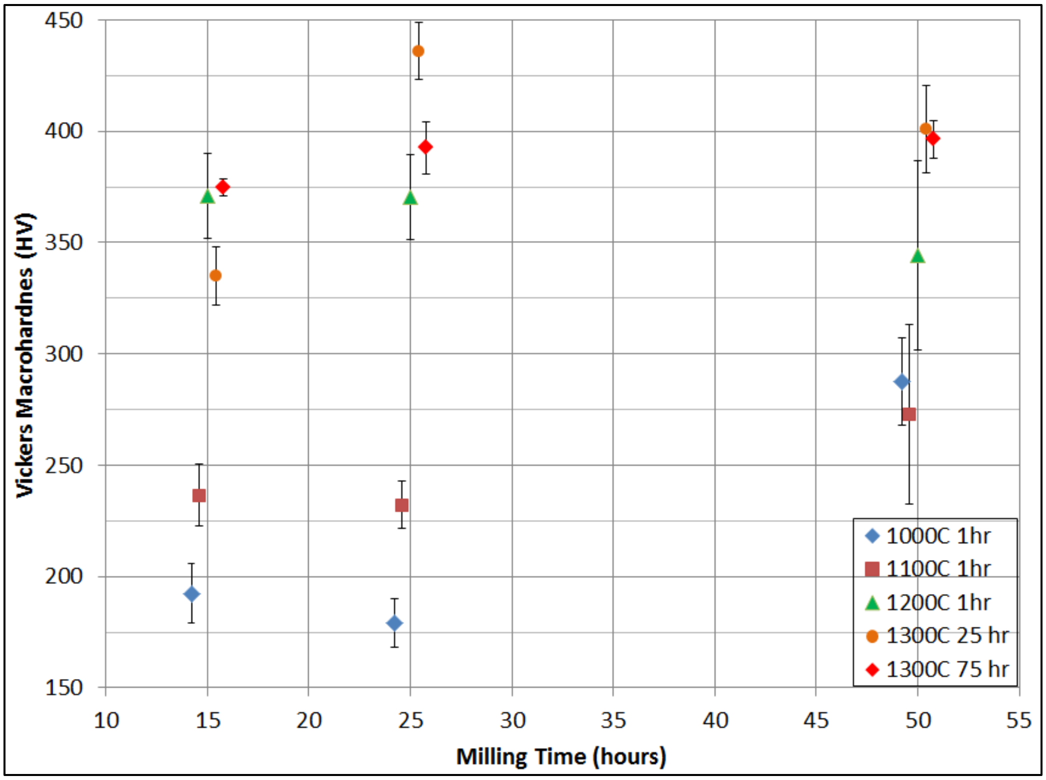

Figure B3.3 Macrohardness as a function of milling time for all sintering temperatures and times

B.4 Density Measurement

Table B4.1 Pre-Sintering, Pre-re-CIP Caliper Density			
Sintering Parameters	Milling Time		
	15 hr	25 hr	50 hr
1000°C 1 hr HT	12.23	11.86	9.97
1100°C 1 hr HT	12.41	11.87	10.34
1200°C 1 hr HT	12.14	11.71	10.02
1300°C 25 hr HT	---	11.11	---
1300°C 75 hr HT	11.58	11.43	11.52

Table B4.2 Pre-Sintering, Post-re-CIP Caliper Density			
Sintering Parameters	Milling Time		
	15 hr	25 hr	50 hr
1000°C 1 hr HT	---	12.13	9.98
1100°C 1 hr HT	12.41	12.04	10.68
1200°C 1 hr HT	12.27	12.43	10.32
1300°C 25 hr HT	---	---	---
1300°C 75 hr HT	---	---	---

Table B4.3 Pre-Sintering, Pre-re-CIP Archimedes’ Density (in g/cc)			
Milling Time	15 hr	25 hr	50 hr
Density (g/cc)	12.47	12.90	14.50

Table B4.4 Post-Sintering Caliper Density			
Sintering Parameters	Milling Time		
	15 hr	25 hr	50 hr
1000°C 1 hr HT	---	13.55	14.60
1100°C 1 hr HT	15.07	15.01	15.21
1200°C 1 hr HT	16.60	16.67	16.66
1300°C 25 hr HT	---	---	---
1300°C 75 hr HT	17.19	17.43	16.32

Table B4.5 Post-Sintering Archimedes’ Density (in g/cc)			
Sintering Parameters	Milling Time		
	15 hr	25 hr	50 hr
1000°C 1 hr HT	15.42	15.33	15.63
1100°C 1 hr HT	16.33	16.25	16.25
1200°C 1 hr HT	16.90	16.85	17.16
1300°C 25 hr HT	18.08	17.65	18.17
1300°C 75 hr HT	17.81	17.88	17.16

Appendix C: Permissions

C.1 ASM International

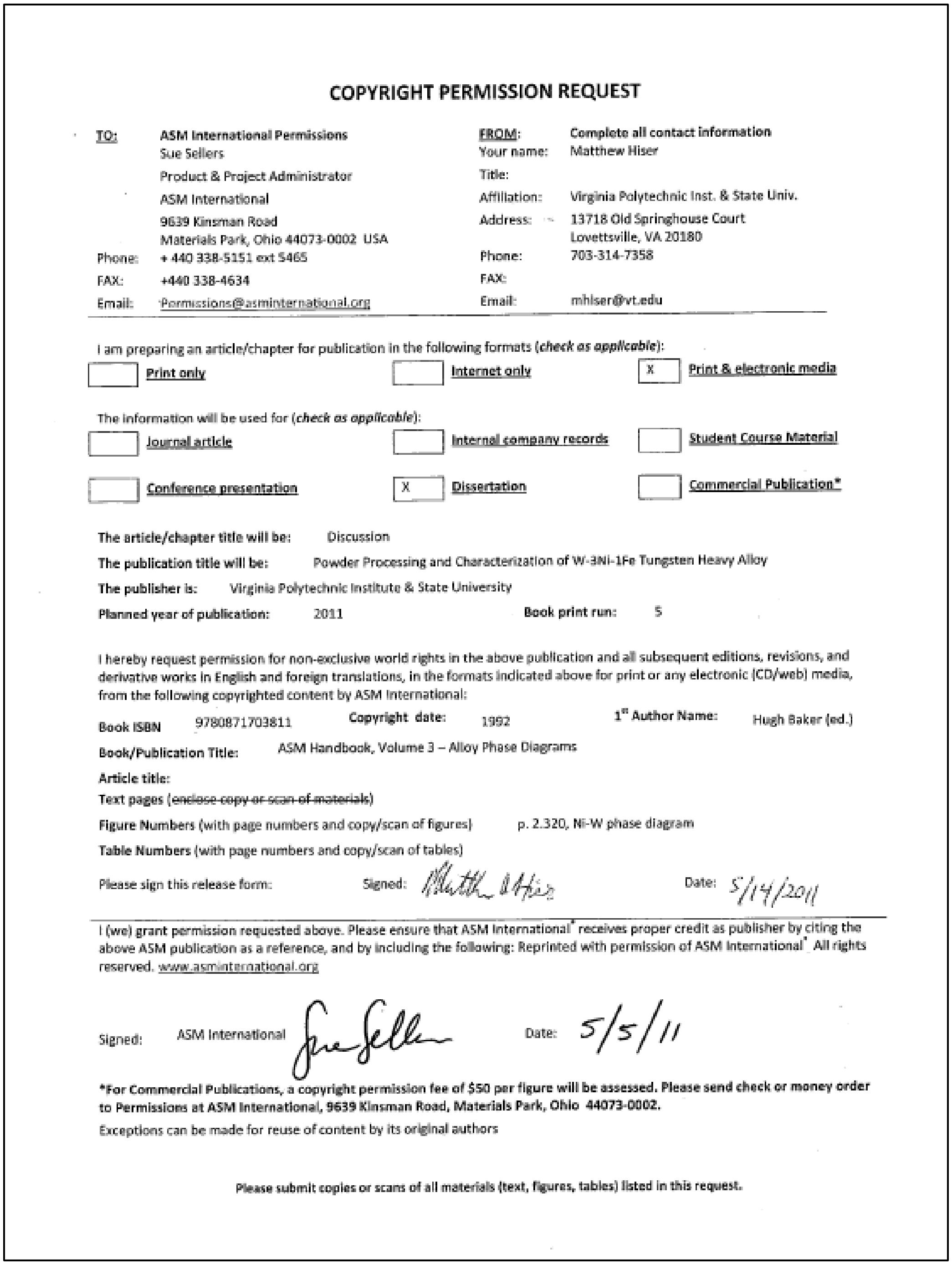

COPYRIGHT PERMISSION REQUEST

TO:	**ASM International Permissions** Sue Sellers Product & Project Administrator ASM International 9639 Kinsman Road Materials Park, Ohio 44073-0002 USA	**FROM:**	**Complete all contact information**
		Your name:	Matthew Hiser
		Title:	
		Affiliation:	Virginia Polytechnic Inst. & State Univ.
		Address:	13718 Old Springhouse Court Lovettsville, VA 20180
Phone:	+ 440 338-5151 ext 5465	Phone:	703-314-7358
FAX:	+440 338-4634	FAX:	
Email:	Permissions@asminternational.org	Email:	mhiser@vt.edu

I am preparing an article/chapter for publication in the following formats (***check as applicable***):

☐ **Print only** ☐ **Internet only** ☒ **Print & electronic media**

The information will be used for (***check as applicable***):

☐ **Journal article** ☐ **Internal company records** ☐ **Student Course Material**

☐ **Conference presentation** ☒ **Dissertation** ☐ **Commercial Publication***

The article/chapter title will be: Discussion

The publication title will be: Powder Processing and Characterization of W-3Ni-1Fe Tungsten Heavy Alloy

The publisher is: Virginia Polytechnic Institute & State University

Planned year of publication: 2011 **Book print run:** 5

I hereby request permission for non-exclusive world rights in the above publication and all subsequent editions, revisions, and derivative works in English and foreign translations, in the formats indicated above for print or any electronic (CD/web) media, from the following copyrighted content by ASM International:

Book ISBN 9780871703811 **Copyright date:** 1992 **1st Author Name:** Hugh Baker (ed.)

Book/Publication Title: ASM Handbook, Volume 3 – Alloy Phase Diagrams

Article title:

Text pages (~~enclose copy or scan of materials~~)

Figure Numbers (with page numbers and copy/scan of figures) p. 2.320, Ni-W phase diagram

Table Numbers (with page numbers and copy/scan of tables)

Please sign this release form: Signed: Date: 5/14/2011

I (we) grant permission requested above. Please ensure that ASM International® receives proper credit as publisher by citing the above ASM publication as a reference, and by including the following: Reprinted with permission of ASM International® All rights reserved. www.asminternational.org

Signed: ASM International Date: 5/5/11

***For Commercial Publications, a copyright permission fee of $50 per figure will be assessed. Please send check or money order to Permissions at ASM International, 9639 Kinsman Road, Materials Park, Ohio 44073-0002.**

Exceptions can be made for reuse of content by its original authors

Please submit copies or scans of all materials (text, figures, tables) listed in this request.

COPYRIGHT PERMISSION REQUEST

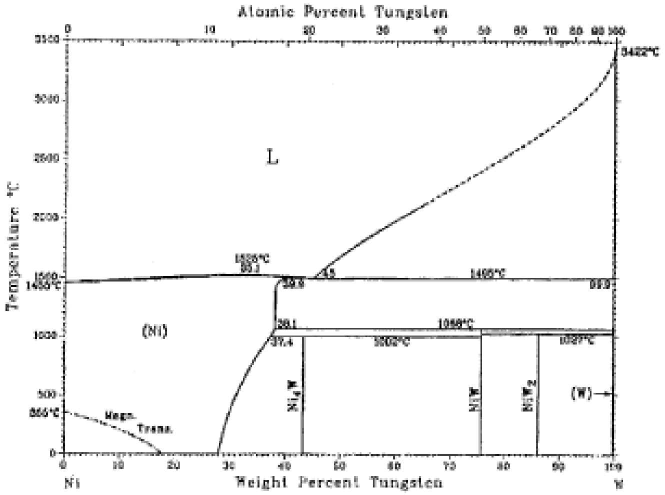

Please submit copies or scans of all materials (text, figures, tables) listed in this request.

C.2 Metal Powder Industries Federation (MPIF)

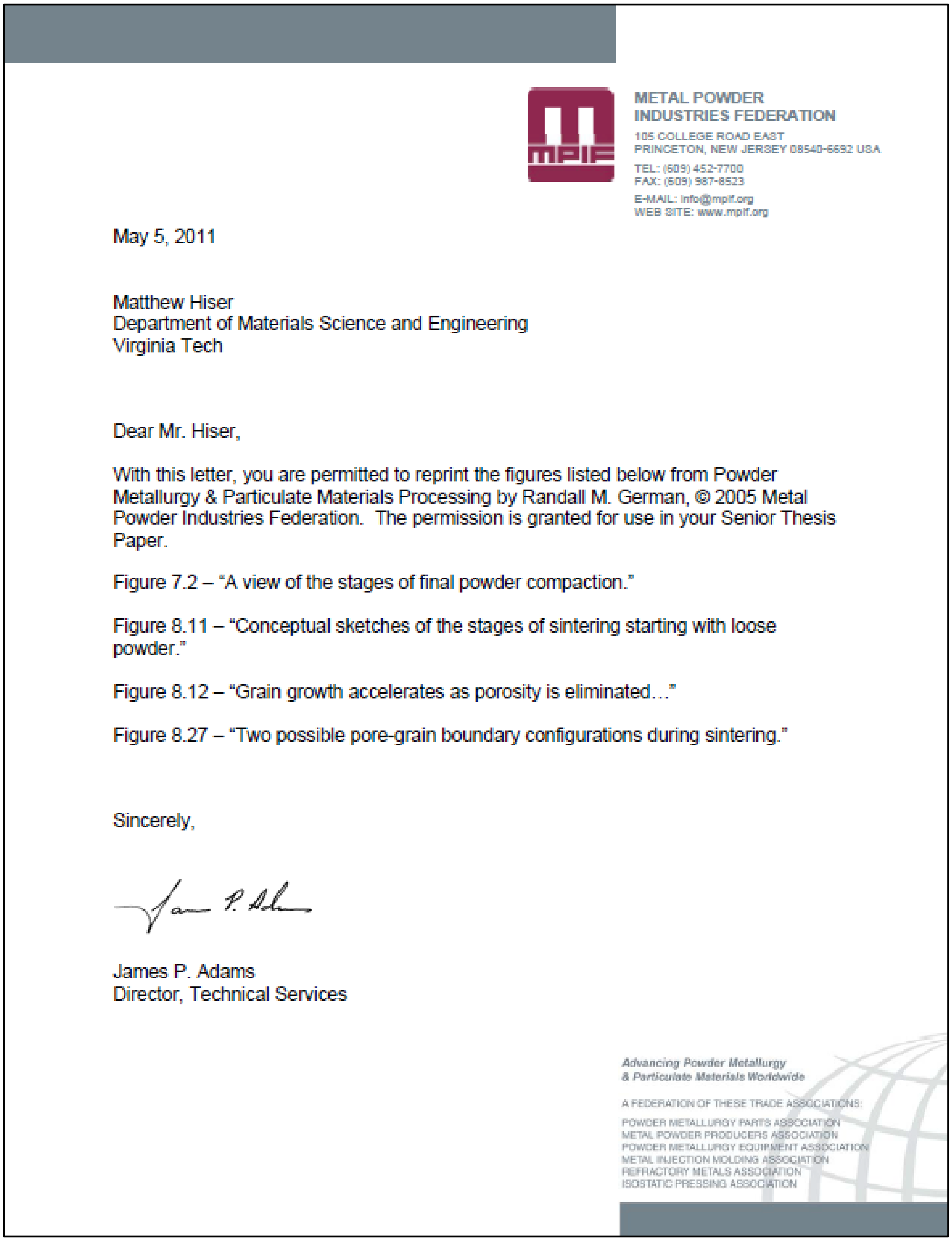

METAL POWDER
INDUSTRIES FEDERATION
105 COLLEGE ROAD EAST
PRINCETON, NEW JERSEY 08540-6692 USA
TEL: (609) 452-7700
FAX: (609) 987-8523
E-MAIL: info@mpif.org
WEB SITE: www.mpif.org

May 5, 2011

Matthew Hiser
Department of Materials Science and Engineering
Virginia Tech

Dear Mr. Hiser,

With this letter, you are permitted to reprint the figures listed below from Powder Metallurgy & Particulate Materials Processing by Randall M. German, © 2005 Metal Powder Industries Federation. The permission is granted for use in your Senior Thesis Paper.

Figure 7.2 – "A view of the stages of final powder compaction."

Figure 8.11 – "Conceptual sketches of the stages of sintering starting with loose powder."

Figure 8.12 – "Grain growth accelerates as porosity is eliminated…"

Figure 8.27 – "Two possible pore-grain boundary configurations during sintering."

Sincerely,

James P. Adams
Director, Technical Services

Advancing Powder Metallurgy
& Particulate Materials Worldwide

A FEDERATION OF THESE TRADE ASSOCIATIONS:

POWDER METALLURGY PARTS ASSOCIATION
METAL POWDER PRODUCERS ASSOCIATION
POWDER METALLURGY EQUIPMENT ASSOCIATION
METAL INJECTION MOLDING ASSOCIATION
REFRACTORY METALS ASSOCIATION
ISOSTATIC PRESSING ASSOCIATION

C.3 Cambridge University Press

http://www.cambridge.org/rights/permissions/permission.htm

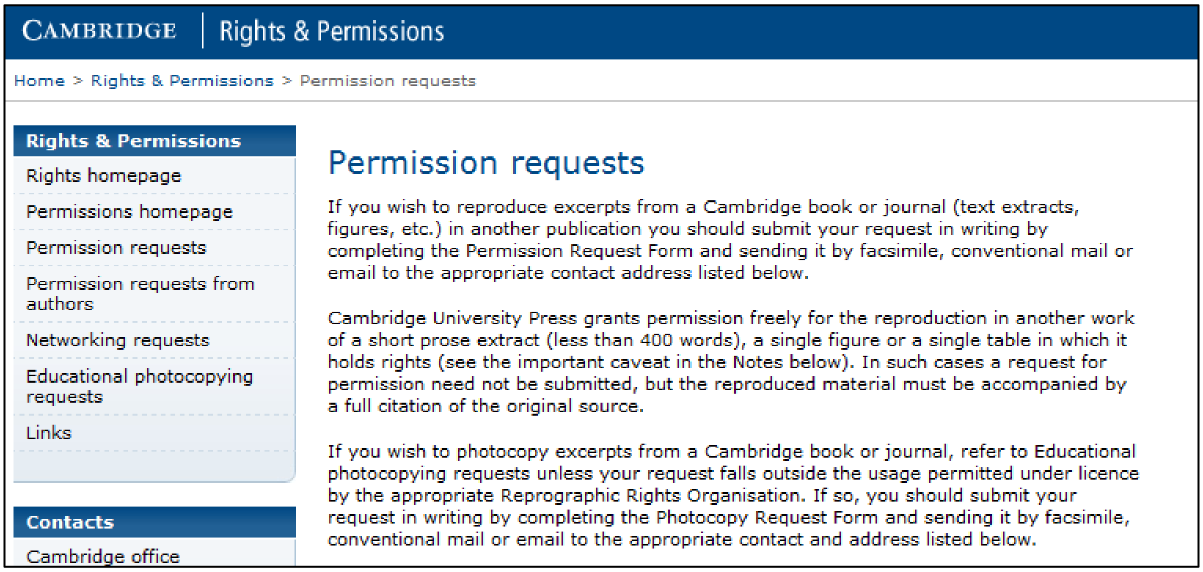

Permission requests

If you wish to reproduce excerpts from a Cambridge book or journal (text extracts, figures, etc.) in another publication you should submit your request in writing by completing the Permission Request Form and sending it by facsimile, conventional mail or email to the appropriate contact address listed below.

Cambridge University Press grants permission freely for the reproduction in another work of a short prose extract (less than 400 words), a single figure or a single table in which it holds rights (see the important caveat in the Notes below). In such cases a request for permission need not be submitted, but the reproduced material must be accompanied by a full citation of the original source.

If you wish to photocopy excerpts from a Cambridge book or journal, refer to Educational photocopying requests unless your request falls outside the usage permitted under licence by the appropriate Reprographic Rights Organisation. If so, you should submit your request in writing by completing the Photocopy Request Form and sending it by facsimile, conventional mail or email to the appropriate contact and address listed below.

C.4 Elsevier

https://s100.copyright.com/CustomerAdmin/PLF.jsp?lID=2011050_1304534269387

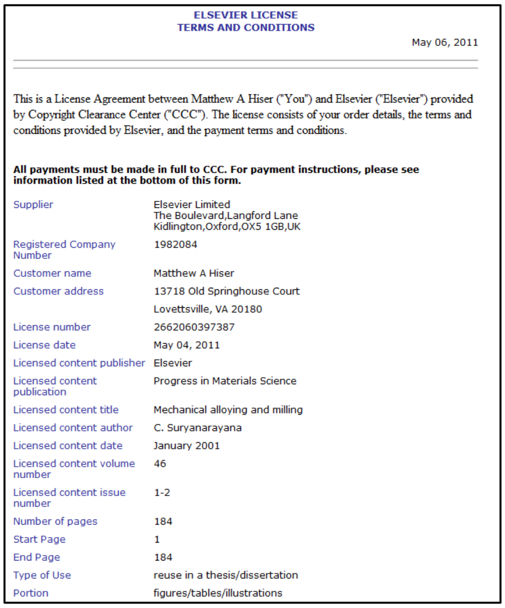

ELSEVIER LICENSE
TERMS AND CONDITIONS

May 06, 2011

This is a License Agreement between Matthew A Hiser ("You") and Elsevier ("Elsevier") provided by Copyright Clearance Center ("CCC"). The license consists of your order details, the terms and conditions provided by Elsevier, and the payment terms and conditions.

All payments must be made in full to CCC. For payment instructions, please see information listed at the bottom of this form.

Supplier	Elsevier Limited The Boulevard,Langford Lane Kidlington,Oxford,OX5 1GB,UK
Registered Company Number	1982084
Customer name	Matthew A Hiser
Customer address	13718 Old Springhouse Court Lovettsville, VA 20180
License number	2662060397387
License date	May 04, 2011
Licensed content publisher	Elsevier
Licensed content publication	Progress in Materials Science
Licensed content title	Mechanical alloying and milling
Licensed content author	C. Suryanarayana
Licensed content date	January 2001
Licensed content volume number	46
Licensed content issue number	1-2
Number of pages	184
Start Page	1
End Page	184
Type of Use	reuse in a thesis/dissertation
Portion	figures/tables/illustrations

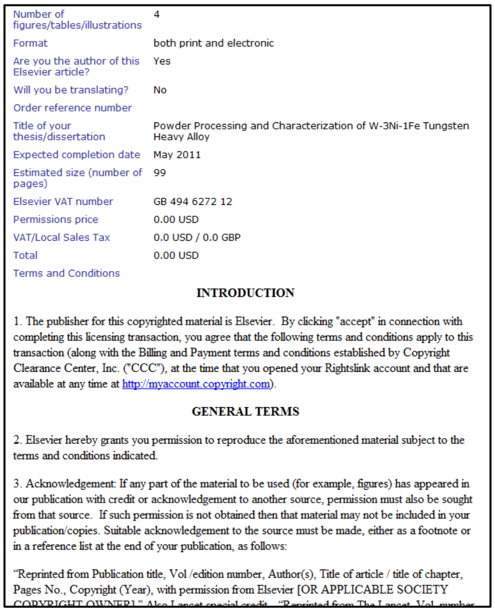

Number of figures/tables/illustrations	4
Format	both print and electronic
Are you the author of this Elsevier article?	Yes
Will you be translating?	No
Order reference number	
Title of your thesis/dissertation	Powder Processing and Characterization of W-3Ni-1Fe Tungsten Heavy Alloy
Expected completion date	May 2011
Estimated size (number of pages)	99
Elsevier VAT number	GB 494 6272 12
Permissions price	0.00 USD
VAT/Local Sales Tax	0.0 USD / 0.0 GBP
Total	0.00 USD
Terms and Conditions	

INTRODUCTION

1. The publisher for this copyrighted material is Elsevier. By clicking "accept" in connection with completing this licensing transaction, you agree that the following terms and conditions apply to this transaction (along with the Billing and Payment terms and conditions established by Copyright Clearance Center, Inc. ("CCC"), at the time that you opened your Rightslink account and that are available at any time at http://myaccount.copyright.com).

GENERAL TERMS

2. Elsevier hereby grants you permission to reproduce the aforementioned material subject to the terms and conditions indicated.

3. Acknowledgement: If any part of the material to be used (for example, figures) has appeared in our publication with credit or acknowledgement to another source, permission must also be sought from that source. If such permission is not obtained then that material may not be included in your publication/copies. Suitable acknowledgement to the source must be made, either as a footnote or in a reference list at the end of your publication, as follows:

“Reprinted from Publication title, Vol /edition number, Author(s), Title of article / title of chapter, Pages No., Copyright (Year), with permission from Elsevier [OR APPLICABLE SOCIETY COPYRIGHT OWNER].” Also Lancet special credit - “Reprinted from The Lancet, Vol. number

C.5 Virginia Tech ESM Professor Romesh C. Batra

http://www.sv.vt.edu/research/batra-stevens/pent.html

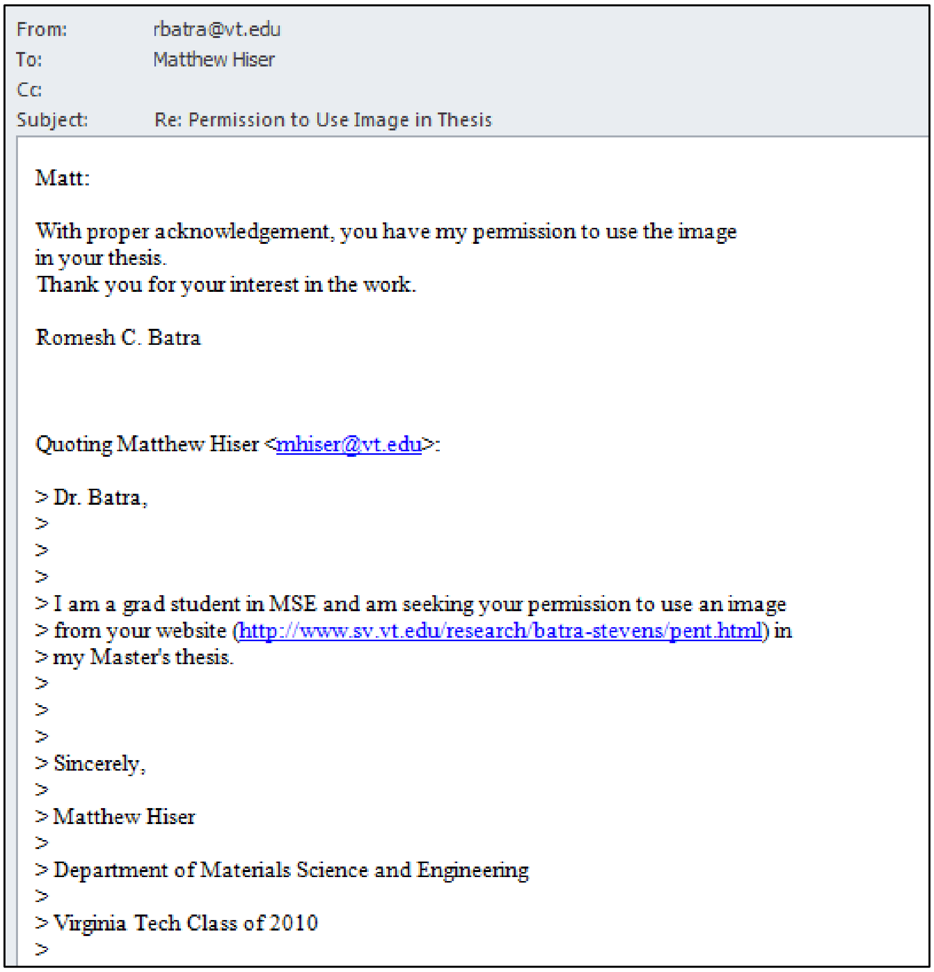

From: rbatra@vt.edu
To: Matthew Hiser
Cc:
Subject: Re: Permission to Use Image in Thesis

Matt:

With proper acknowledgement, you have my permission to use the image
in your thesis.
Thank you for your interest in the work.

Romesh C. Batra

Quoting Matthew Hiser <mhiser@vt.edu>:

> Dr. Batra,
>
>
>
> I am a grad student in MSE and am seeking your permission to use an image
> from your website (http://www.sv.vt.edu/research/batra-stevens/pent.html) in
> my Master's thesis.
>
>
>
> Sincerely,
>
> Matthew Hiser
>
> Department of Materials Science and Engineering
>
> Virginia Tech Class of 2010
>

C.6 Wikimedia Commons

http://commons.wikimedia.org/wiki/File:Sabot_separating.gif

No higher resolution available.

Sabot_separating.gif (400 × 303 pixels, file size: 102 KB, MIME type: image/gif)

Summary

[edit]

Taken from http://www.dtc.army.mil/tts/1997/proceed/walton/walton.html

Caption: "shows a modern Kinetic Energy (KE) projectile shortly after muzzle exit, as the sabot petals are separating from the penetrator."

Licensing

[edit]

This work is in the ***public domain*** *in the United States because it is a work of the United States Federal Government under the terms of* Title 17, Chapter 1, Section 105 of the US Code. *See Copyright.*

Note: This only applies to works of the Federal Government and not to the work of any individual U.S. state, territory, commonwealth, county, municipality, or any other subdivision. This template also does not apply to postage stamp designs published by the United States Postal Service since 1978. (See 206.02(b) of Compendium II: Copyright Office Practices). It also does not apply to certain US coins, see The US Mint Terms of Use.

العربية | Беларуская (тарашкевіца) | Български | বাংলা | Català | Česky | Deutsch | English | Esperanto | Español | Eesti | Euskara | فارسی | Suomi | Français | Magyar | Italiano | 日本語 | 한국어 | Македонски | Plattdüütsch | Nederlands | Polski | Português | Português do Brasil | Русский | ไทย | Türkçe | Vèneto | 中文 | 中文(简体) | 中文(繁體) | +/−

This file has been identified as being free of known restrictions under copyright law, including all related and neighboring rights.